Investigations of Ion Channel Structure-Function Relationships Using Molecular Modeling and Experimental Biochemistry

Thesis by

Donald Eugene Elmore, Jr.

In Partial Fulfillment of the

Requirements for the Degree of

Doctor of Philosophy

California Institute of Technology

Pasadena, California

2004

(Defended April 22, 2004)

Acknowledgments

"But this dedication is for others to read:
These are private words addressed to you in public."

- T. S. Eliot

It is certainly too rare that I take an opportunity to sit back and thank the people who have contributed greatly to my life in so many ways. Thus, I think that this is not just the only part of this thesis any of you will read (yes, you can admit it without offending me—even *I* have trouble getting past page 7 at this point), but it's also really the most important part. So, for lack of a better place, I'll start at the beginning . . . .

I treasure countless memories of growing up in Murphysboro, IL, with my wonderful parents, Donald (the elder) and Patricia Elmore. They provided an ideal environment to be a child—to learn about the world, to have fun, and to just be loved—and have been a constant source of support in the past twenty-eight years. I have great respect for both of them personally and professionally, and they are great role models in innumerable ways. I also was very fortunate to have three grandparents living in Murphysboro while I was growing up. My Grandmother "B" (who thankfully let me shorten her name from Borgsmiller when I was young!) and Grandmother and Grandfather Elmore were each a source of inspiration in their own way—and always were fun to have around to hang out with. I feel very lucky to know that my parents and grandmothers back in Southern Illinois are always ready to warmly welcome me home for a visit.

I was also able to discover a love of learning about the world through scientific exploration while a student in Murphysboro. From the first open-ended projects in Carol O'Donnell and Nancy Borgsmiller's classes in elementary school to working on science fair projects in Mary Williams and Molly McDaniels' junior high sciences courses, I was fortunate to see that science was far more than just the memorization of facts. My appreciation of science was further enhanced through the remarkable opportunities I encountered at the Illinois Mathematics and Science Academy. In particular, Richard Dods set me on the trajectory towards chemistry (and particularly biochemistry), and Donald Dosch and Ed Goebel helped solidify my interests in biology. Throughout my junior and senior years, I was able to perform research in the laboratory of Roger Melvold at Northwestern University Medical School, which gave me invaluable research experience before starting college (and also showed me that I did not want to personally do research on animal models!). As well, the innovative teaching methods employed frequently at IMSA, especially their emphasis on experiential learning helped foster my interest in teaching and research in education. Of course, I shouldn't forget the constant pull towards literature that I began to feel during high school, largely due to classes taught by Grant Walker, Larry Chott, and Jackie White.

When I left high school for Central Iowa, I had no inkling of the incredible personal and intellectual growth I would experience in the challenging and supportive environment at Grinnell College. Institutions are no greater than the people who make them up, and this was no exception at Grinnell where I had wonderful classmates (many of whom are still my closest friends) and professors. Among the generally outstanding faculty I encountered were many dedicated members of the Chemistry Department,

particularly Mary Mader, a supportive and always candid academic advisor; Martin Minelli, with his constant enthusiasm; and Charlie Liberko, who made organic chemistry a surprisingly enjoyable experience for me as a first-year student. I was also lucky to have another academic "home" at Grinnell in the English Department, who encouraged me despite my split loyalties. In particular, Elizabeth Dobbs' classes were the most challenging (and rewarding) I encountered during college (or graduate school), and represent the ideal I hope to approach when teaching my own seminar classes. The Grinnell Biology Department was also very supportive of my crossover interests, especially Leslie Gregg-Jolly, Bruce Voyles, and Deborah Eastman. Carol Trosset in the Office of Institutional Research was gracious enough to work with Julia Prentice and I on an educational research project I was grossly underqualified to perform but nonetheless gave me a valuable crash course in social science research methods. However, Jim Swartz stands alone in my esteem among the Grinnell faculty. In addition to being a great undergraduate research advisor, he has been a superlative mentor and friend. I am always amazed by the amount of support he has given not only me but so many others at Grinnell and throughout the wider academic community, and I would be happy if I am a fraction as influential as him on my own students.

Also during college, Steve Scheiner at Southern Illinois University was kind enough to open up his research lab to me after my first year, where I was infected with an excitement for computational chemistry. Both Steve and his research associate Tapas Kar provided me with the perfect balance of guidance and freedom to critically develop my research skills.

For some reason, four years of college chemistry wasn't enough for me, so I decided to head out to Caltech where I was savvy (or more honestly lucky) enough to join the Dougherty Group. Simply stated, Dennis Dougherty has been the model advisor (although I have ignored his advice on terse writing in these acknowledgments). Unlike so many other people, I truly *enjoyed* graduate school, and I know this was in no small part due to working for Dennis. I sometimes doubt I would have even completed graduate school with any other advisor, and I am certain that I would not have grown so much from the experience. I truly appreciate the intellectual freedom he was willing to give me on projects from the very beginning, which made my research much more meaningful in my scientific development. And, in addition to being a wonderful scientific mentor, he is also an exemplary person who can teach many valuable lessons about life outside of the lab. Over the past years, the rest of the Dougherty Clan (Ellen, Meg, and Kayla) have frequently welcomed other group members and me into their home, and I always looked forward to those gatherings.

The members of the Dougherty Group provided a wonderful working (and often *non*-working) environment in which to spend my time at Caltech. It goes without saying that they provided an intellectually stimulating environment for science, and numerous insightful conversations with group members have taken my projects in directions I would never have envisioned alone. However, what I will remember most about the group is the endearing personalities of its members. I have enough stories about all of them to fill pages, but I'll just give a glimpse into those here. Gabriel Brandt gave me my first positive impression of the group when I was a prospective student, and he exemplified the best qualities of the group—I greatly miss having him two desks away

for long and varied conversations (and I am so glad he will be in Boston next year!). Justin Gallivan was there to give me a warm welcome and some useful advice when I first showed up. Seth Miller pointed out the necessity of taking a break from thesis writing with his pursuit of Ms. Pac Man high scores. Jen Ma showed me the value of a leisurely lunch after her graduation. Pam England had an unstoppable energy towards any pursuit. Jesse Lin has an amazing opera voice (that gave me quite a fright one late night in lab!). Marcus Sarofim is one of the most sincere people I've ever met—in addition to being skilled at Pint-Sized Punchlines. Niki Zacharias is a model of kindness, both to those in direct contact with her and to the world as a whole, and was responsible for organizing far more than her share of group events. Lintong Li was an impressive example of effectively balancing professional and family lives that I could learn more from. I have always admired David Dahan's consistency throughout many aspects of his life, showing a balance I know I lack. James Petersson is the modern day embodiment of the *sprezzatura* of Casiglione's courtier (in all of its good connotations)—he makes it seem so easy to do a wide variety of things impressively well, including making it "cool" to listen to the Thom Bell Sessions. I was thankful to have another English major in the group with Darren Beene (albeit one whose knowledge of literature and culture far exceeds my own), and seeing him as a doting father has been particularly heartwarming. I've enjoyed Sarah Monahan's perspective in a wide range of conversations, from women in science to the Canadian medical system. Steve Spronk helped me remember my "glory days" of scholar bowl, and his encyclopedic knowledge of all things athletic is remarkable. Lori Lee has been too gracious in taking care of Hector during vacations, and I always look forward to perpetually engaging talks with her over Orean or falafel. I

love sharing notes on new music with Amanda Cashin, and despite my sarcastic remarks there is no one I would rather have move into my old desk. Tingwei Mu exudes an infectious enthusiasm in lab that helped boost my morale. Despite his foolhardy attempt to avoid driving in Los Angeles *and* being an MIT graduate, Michael Torrice is an amazingly well-balanced person with a keen sense of humor and a wisdom beyond his years in graduate school. Being too often out of shape myself, Amy Eastwood's dedication to marathon training leaves me speechless. Erik Rodriguez has shown incredible patience in being able to deal with the rest of us both as an undergraduate and a graduate student. Joanne Xiu was too kind as my desk "neighbor," dealing daily with my encroaching papers without complaint. Julian Revie's search for a patron highlighted his impressive moxie and unique perspective on the world. Katie McMenimen seems poised to carry the torch well for the group, and has been overly nice to this random old grad student who kept showing up this year. And, Catherine Baker was a welcome "honorary group member," providing advice on hamster care and incisive perspectives on the Gilmore Girls. I have also been lucky enough to interact with several talented undergraduate researchers, including Paola Giusti, Lisa Turner, Anita Choi, and Caroline Gibbs, who brought enthusiasm and unique insights to the group.

One group member, Josh Maurer, deserves a special mention. Josh was brave enough to help this computationalist learn biochemical lab techniques, and was a first-rate collaborator on many projects (some more successful than others!) over the years. (Much of the material in Chapters 2 and 3 were done in collaboration with him.) I look back fondly on our time in lab together, but most of all I am glad for the friendship that

grew out of it. I always looked forward to Baja lunches, constructing lofts, or "Josh's Day Out," all of which made my time at Caltech much happier.

I have also been able to work with some other wonderful people at Caltech. Henry Lester, Doug Rees, and Gerd Kochendoerfer have been wonderful collaborators on the mechanosensitive ion channel projects, and I have always appreciated their input on my research. My other committee members, Bill Goddard and Harry Gray, made valuable contributions to my candidacy and research proposal meetings. Ken Philipson provided invaluable biological experience to the early MscL calculations. Many people in the Lester Group have helped supply resources during my time at Caltech, in particular Purnima Deshpande (who organizes more than the rest of us have ever appreciated), Kira Kostenko, and Vanna Santoro. As well, the Chemistry Division at Caltech runs so smoothly due to the hard work of many staff members, including Linda Syme, Dian Buchness, Tom Dunn, Chris Smith, Steve Gould, Paul Carroad, and Debbie Miles.

During the past year, I have also been able to work with some wonderful people in the Joint Sciences Department at the Claremont Colleges, and I have really appreciated the opportunity to develop my teaching skills in a very supportive environment. Katie Purvis-Roberts stepped up from the start as my informal (and eventually formal) faculty mentor, and I will miss our frequent "mentoring" lunches and other get togethers. Mary Hatcher-Skeers has been a great cheerleader from the moment I met her at my interview. I'm very glad that I've been able to compare notes with Loyd Bastin throughout the job search process, and it will be nice to have him also moving east this fall. Harriet Moeur's hard work has made it easy for even me to teach organic labs effectively. I will also fondly remember many great conversations and "power lunches" with Nina Karnovsky,

Todd Coleman, and Alex Reich during meetings for the "real" faculty. And, I've been very fortunate to work with some phenomenal students—including a few invaluable teaching assistants, Irene Frank and Rachel Levitan—who I am certain will go on to many great things in their lives after Claremont.

I have also been blessed with many friends outside of my professional life while I have been in Los Angeles, and I think those are the people who have truly kept me balanced enough to actually complete my doctorate! Jamie Pflasterer and Ian Spielman have helped make Pasadena feel more like home from our first month in Southern California, and I will always have fond memories of spending time with them from the early Ally McBeal days to hanging out with their son Camden in the last few months. It was also wonderful to have a few Grinnellians to make the LA transition with—Rachel Taylor and Cory Turner have always been a beacon to us from the fabled West Side, providing a constant source of friendship and insights into the interesting worlds of non-profits and the movie industry. Jeremy "Lil' Dude" Hill has often been a necessary ballast for me throughout the last six years just as he was during our four years in college. No matter whether we were taking in great (and sometimes not so great) concerts, watching Dodgers baseball, or just hangin' in the Valley, I am so glad that he decided to grace Los Angeles with his presence for a few years—and I am even happier that we will at least be on the same coast again in a few months. I was also fortunate to have some high school friends, Russ Schaaf and Ryan Fox, living around Southern California while I was here, and I appreciate your friendships that have extended far over a decade now.

Of course, I couldn't be lucky enough to have all of my friends living in Los Angeles. However, although they have been in London, Ft. Wayne, and Kansas City

during my years at Caltech, Ted Smith and Laura Schwartz have been such great friends that it has seemed like they were always close at hand. I am really glad we have been able to visit so frequently over the years, and I look forward to countless more vacations and phone calls. Many other friends from Grinnell and back home in Illinois have been wonderful to visit with many times over the past years, including Bill Bell, Joanna Church, Kate Fuller, Sarah Halpin, Kristen Jensen, Elizabeth Murphy, Barbara Sloss and Owen Stanwood. It is so wonderful to look at a map and realize that there is a great friend just a day's drive away pretty much anywhere I go—my own modern day Missions, so to speak. I am also very fortunate to have gained some very supportive in-laws—Rod and Myrna Prentice, who are always interested in hearing descriptions of my research; Patricia Prentice, the ideal sister-in-law in more ways that I could mention; and Grandma June Dailey and the late Grandma Avis Prentice, who lived such inspiring lives.

And, I will close with the most important acknowledgement of all. When I set out with my best friend to live in California six years ago, we never could have known the spectrum of experiences we would have. But, Julie, because you were with me throughout, I look back on it all fondly. We have (somehow!) made it here, and I look forward to conquering the other coast with you next! I love you immensely, and I never cease to be amazed by everything about you. Thanks for all of the support, all of the laughter, all of the caring, and most of all for making my world a better place. To finish this section as we began, in Eliot's words, you are: "To whom I owe the leaping delight / That quickens my senses in our wakingtime / And the rhythm that governs the repose of our sleepingtime / The breathing in unison."

Abstract

Ion channels are integral membrane proteins found in all cells that mediate the selective passage of specific ions or molecules across a cell membrane. These channels are important in a diverse range of physiological processes, including signal transmission in the nervous system, sensory perception, and regulation of vital systems, such as circulation. This thesis discusses the use of computational chemistry methods, such as molecular dynamics (MD) and *ab initio* calculations, and experimental biochemical techniques, such as site-directed mutagenesis, *in vivo* bacterial assays, chemical cross-linking, and circular dichroism spectroscopy, in tandem to elucidate ion channel structure-function relationships. This research was catalyzed by the solving of atomic resolution crystal structures of the mechanosensitive channels of large and small conductance (MscL and MscS) by the Rees group. Although interesting themselves, these bacterial channels also provide good model systems for considering more complex eukaryotic channels.

MscL is an ion channel gated only by membrane tension. Initial studies of MscL verified the relevance of the crystal structure conformation under physiological conditions and compared different MscL homologues. Other work began to elucidate potentially unique structural and functional roles of the *M. tuberculosis* MscL C-terminal helical bundle. As well, interactions between the MscL channel protein and surrounding lipid and the potential relevance of helical kinking in MscL gating pathways were investigated. MscS is also gated by membrane tension, but its gating can be modulated by changes in transmembrane potential. Thus, studies on MscS began to identify the

specific amino acid residues that are responsible for giving the channel its voltage sensitivity. Finally, computations predicting the conformation of nicotine in different solvent environments are discussed. Nicotine is a small molecule ligand that binds to and gates nicotinic acetylcholine receptors, and a thorough understanding of nicotine structure could aid efforts to elucidate receptor structure-function relationships and design new pharmaceuticals.

Table of Contents

List of figures

Chapter 1: Introduction

Ion Channels

Ion channels are integral membrane proteins found in all cells that mediate the selective passage of specific ions or molecules across a cell membrane (Alberts et al., 1994). These channels are important in a diverse range of physiological processes, including signal transmission in the nervous system, sensory perception, and regulation of vital systems, such as circulation.

These ion channels can be considered selective in two ways. First, since channels can exist in open and closed conformations they are *temporally* selective. In an open conformation, a channel mediates the formation of a column of water across the membrane through which ions can pass, while in a closed conformation this column is blocked, preventing the flow of ions. Different channels are converted from their closed to open states—or "gated"—by different types of stimuli. Thus, channels are often divided into three general categories based on the type of stimulus to which they respond (Fig. 1.1).

Perhaps the simplest of these categories includes channels that respond to mechanical stress in the membrane (Fig. 1.1A). These mechanosensitive channels are gated by tension that they sense either through direct contact with membrane lipids or indirectly through forces applied through attached cytoskeletal elements. Although their gating stimulus appears relatively primitive, these types of channels are nonetheless very important physiologically, playing a role in touch and hearing in higher organisms and osmotic regulation in prokaryotes (Hamill and Martinac, 2001). Channels that are gated by changes in transmembrane voltage form the second class of channels (Fig. 1.1B). These voltage-gated channels that respond to membrane depolarization or

hyperpolarization are central to the transmission of electrical signals along nerve axons. The final category of channels are ligand-gated channels, or channels that are gated upon the binding of some small molecule ligand, such as acetylcholine, serotonin, or glycine (Fig. 1.1C). Some notable examples of ligand-gated channels occur at the synapses between nerves, where the electrical signal is transmitted from the end of an axon to an adjacent neuron through the passing of a neurotransmitter molecule—a ligand—through the synaptic gap.

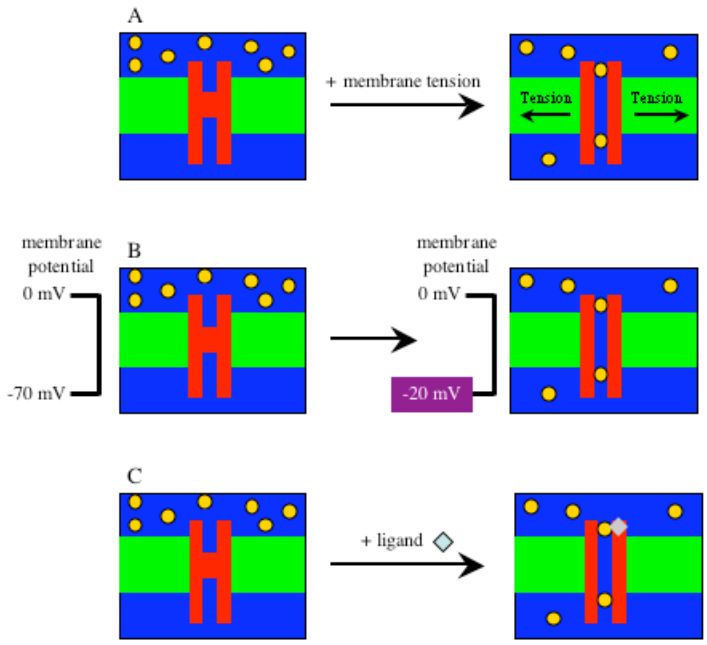

Figure 1.1: The three general categories of gating stimuli for ion channels. Ion channel proteins are shown in red with membrane, water, and ions in green, blue, and yellow, respectively. A) Mechanosensitive channels are gated by membrane tension sensed through the membrane or cytoskeletal elements. B) Voltage-sensitive channels are gated by changes in transmembrane voltage, such as the membrane depolarization depicted here. C) Ligand-gated channels are gated by the binding of some small molecule ligand, shown here as a light blue diamond.

Although channels are typically divided into these three groups, it is important to remember that some channels can respond to more than one type of stimulus. For example, the MscS channel discussed below appears to be modulated by transmembrane

voltage in addition to being gated by mechanical stress (Martinac et al., 1987). In fact, it has been hypothesized that all types of channels show at least some mechanosensitive modulation as they respond to stresses in the surrounding lipid environment (Gu et al., 2001).

In addition to temporal selectivity, channels are also selective for certain ions. For example, certain channels are highly selective for K^+ ions, while others selectively pass Na^+, Ca^{2+}, or Cl^-. This ion selectivity is particularly noteworthy since channels that allow a relatively rapid flow of ions also show an impressive selectivity between two very similar cations, such as K^+ and Na^+. Thus, ion selectivity has been, and continues to be, the focus of numerous studies of ion channels (Chung and Kuyucak, 2002).

Although ion channels are clearly an important class of molecules, they can also be quite difficult to study. Since the passage of ions through channels produces a current, the gating behavior, selectivity, and other characteristics of channels can be investigated by measuring the currents of open channels through electrophysiological techniques. The activity of a single ion channel can even be measured through patch-clamp electrophysiology. Although electrophysiological studies have provided detailed information about many channels, they provide limited structural information. However, it is quite difficult to produce sufficient quantities of most eukaryotic ion channels for biochemical and spectroscopic studies or for efforts towards direct structure determination. As well, the lack of detailed structural information on ion channels has severely limited the application of molecular modeling techniques. Thus, it would be useful to have ion channel systems that could be studied with a wider range of techniques.

Bacterial Ion Channels

Until relatively recently, many researchers believed that bacteria did not necessarily have ion channels like more complicated organisms (Koprowski and Kubalski, 2001). However, over the past few decades people have come to realize not only that bacteria contain these channels, but that their channels also provide particularly useful models of ion channel systems in higher organisms. In particular, bacterial ion channels can be easily overexpressed in bacterial expression systems (Rees et al., 2000). Thus, a large amount—relative to that obtainable for mammalian channels—of channel protein can be produced and purified for subsequent studies. Purified channel can be used for biochemical studies, such as cross-linking (Maurer et al., 2000; Sukharev et al., 1999), and spectroscopic measurements, such as circular dichroism (Arkin et al., 1998). Other studies have successfully used electron paramagnetic resonance (EPR) spectroscopy measurements of spin-labeled bacterial channels to develop gating models (Perozo et al., 1999; Perozo et al., 2002). Bacterial channels can also be functionally characterized using electrophysiological techniques analogous to those applied to eukaryotic channels. Many channels, such as MscL, KcsA, and ClC, can be purified and reconstituted into lipid vesicles or bilayers of controlled lipid composition (Heginbotham et al., 1998; Maduke et al., 1999; Sukharev et al., 1993), allowing the effects of lipid composition on channel function to be considered. Also, bacterial cells expressing channels can be prepared as spheroplasts, or "giant round-up cells," by preventing them from separating properly after cell division (Saimi et al., 1992). This leads to unusually large "cells" that can be patch-clamped directly for electrophysiological measurements. In addition to using detailed electrophysiological measurements, some bacterial channels

and their mutants can be characterized using high-throughput *in vivo* assays of channel function (Maurer and Dougherty, 2001).

The ability to produce large amounts of channel proteins also makes direct structural determination, such as through crystal structures, feasible. In fact, a few groups have been particularly successful in obtaining crystal structures of bacterial ions channels. In 1998, the first ion channel structures were solved: KcsA, a potassium channel, by the MacKinnon group (Doyle et al., 1998) and MscL, the mechanosensitive channel of large conductance, by the Rees group (Chang et al., 1998) (Fig. 1.2). The KcsA structure allowed the first direct structural interpretation of ion selectivity in potassium channels, the understanding of which has been increased by using the structure as a basis for subsequent theoretical and experimental studies (Sansom et al., 2002). For both channels, the structures offered a starting point for studies predicting the gating transition between closed and open forms (Perozo et al., 1999; Perozo et al., 2002; Sukharev et al., 2001).

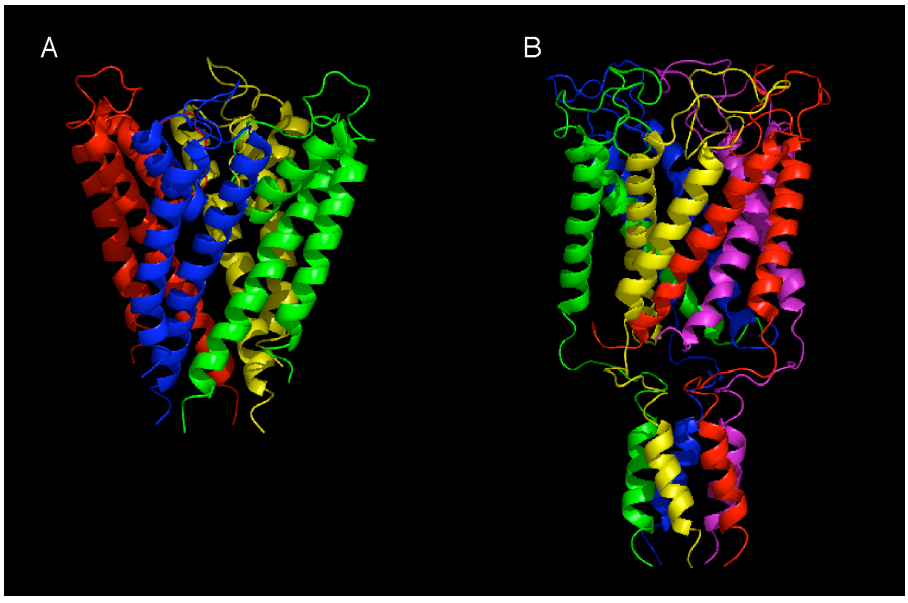

Figure 1.2: Crystal structures of the KcsA (A) and MscL (B) channels.

After the initial mechanosensitive and potassium channel structures, high-resolution structures have been determined for other bacterial ion channels. These have included a chloride selective channel, ClC (Dutzler et al., 2002); a mechanosensitive and voltage modulated channel, MscS (Bass et al., 2002); and a voltage-gated potassium channel, KvAP (Jiang et al., 2003). Thus, it appears that bacterial channels can provide useful structural information for many types of ion channels. This is particularly notable as decades of concerted effort towards determining the high-resolution structure of ion channels from higher organisms has led to limited success. For example, the dedicated work of Unwin and co-workers towards obtaining cryo-EM structures of nAChR from *Torpedo* electroplaques has only led to structures at about 4 Å resolution, too low to resolve atomic-level details (Miyazawa et al., 2003).

Applying Computational Modeling and Experimental Biochemistry to Ion Channel Structures

While the determination of several high-resolution structures of bacterial ion channels has provided the first atomic-level interpretations of many phenomena, the structures also raise even more questions, including figuring out the most effective way to utilize structural data to learn about channel function. One such approach that seems particularly promising is using the structures as a starting point for computational modeling and experimental biochemical studies performed directly in tandem with one another. The solving of the first crystal structures of KcsA and MscL in 1998 coincided with the increasing feasibility of performing multi-nanosecond molecular dynamics (MD) simulations on membrane proteins embedded in explicitly represented hydrated lipid

membranes. For example, one landmark study was the simulation of a porin, OmpF, in a phosphatidylethanolamine membrane (Tieleman and Berendsen, 1998), and this was followed in rapid succession by similar ion channel simulations in several other groups (Forrest and Sansom, 2000; Roux, 2002). These types of simulations, which developed from initial MD studies on explicit hydrated lipid membranes in the early 1990s (Egberts et al., 1994; Heller et al., 1993), allow people to consider channel dynamics and atomic-level interactions that might not be apparent from the static picture provided by a crystal structure. As well, many other types of computations, such as Brownian Dynamics simulations that use structures to predict channel conductances (Chung et al., 2002; Im et al., 2000) and electrostatic calculations (Roux and MacKinnon, 1999), have been used along with crystal structure information. Alone, information from these computations is intriguing, but it is most compelling if it can be tied to experimental results. This can be done relatively readily for bacterial channels, since they are amenable to a wide range of biochemical, spectroscopic, and electrophysiological studies. Thus, a useful synergy can be developed where computation drives experiments, and in turn, experiments drive additional computation.

The following chapters describe my attempts to utilize this in tandem computational-experimental approach to study mechanosensitive, voltage-sensitive, and ligand gated ion channel systems. Chapters 2 through 5 describe different studies of MscL, which is a bacterial channel thought to be gated only by tension in the cell membrane. Chapter 2 describes some initial studies on MscL, including cross-linking studies designed to verify its crystal structure conformation, circular dichroism studies comparing the secondary structure of a number of MscL homologues, and additional

homologue comparisons using a bioinformatics approach. Chapter 3 discusses the use of MD simulations and circular dichroism studies of multiple channel mutants to probe the curious helical bundle conformation of the MscL C-terminal region seen in the crystal structure. Many different molecular dynamics simulations of the full MscL channel crystal structure embedded in a lipid membrane are presented in Chapters 4 and 5. The initial setup of these MD simulations and the ability of the simulations to consider channel mutations are discussed in Chapter 4. These first simulations are extended in Chapter 5 to consider how the membrane lipid composition may affect MscL structure and function. Simulations of MscL in gradually thinner membranes predicted that kinking of transmembrane helices might be an important element of channel gating. This prediction was then tested by experiments and additional computations described in Chapter 5 that characterized MscL mutants with a designed transmembrane kink.

In other studies described in Chapter 6, I have probed the voltage-sensitivity of the mechanosensitive channel of small conductance, MscS. These studies utilized MD simulations of MscS similar to those performed on MscL to structurally verify the supposed voltage sensitivity of the channel and to identify specific amino acid residues likely to be important for voltage sensitivity. These residues were then experimentally mutated and characterized electrophysiologically to verify the computational predictions.

The final chapter, Chapter 7, discusses the use of small molecule *ab initio* calculations and modern solvation models to predict the conformation of the nicotine molecule in aqueous solution. Nicotine is an important agonist of the nicotinic acetylcholine receptor (nAChR), a ligand-gated ion channel. Experimental studies have found that nicotine appears to bind to the channel differently than other agonists, such as

acetylcholine (Beene et al., 2002). Thus, these computations aimed to better characterize the conformational subtleties of nicotine with the goal of gaining insight into its apparently unusual binding behavior.

References

Alberts, B., D. Bray, J. Lewis, M. Raff, K. Roberts, and J. D. Watson. 1994. *Molecular Biology of the Cell*. New York, NY: Garland Publishing, Inc.

Arkin, I. T., S. I. Sukharev, P. Blount, C. Kung, and A. T. Brunger. 1998. Helicity, membrane incorporation, orientation and thermal stability of the large conductance mechanosensitive ion channel from E. coli. *Biochim. Biophys. Acta* 1369:131-40.

Bass, R. B., P. Strop, M. Barclay, and D. C. Rees. 2002. Crystal structure of *Escherichia coli* MscS, a voltage-modulated and mechanosensitive channel. *Science* 298:1582-7.

Beene, D. L., G. S. Brandt, W. Zhong, N. M. Zacharias, H. A. Lester, and D. A. Dougherty. 2002. Cation-pi interactions in ligand recognition by serotonergic (5-HT3A) and nicotinic acetylcholine receptors: the anomalous binding properties of nicotine. *Biochemistry* 41:10262-9.

Chang, G., R. H. Spencer, A. T. Lee, M. T. Barclay, and D. C. Rees. 1998. Structure of the MscL homolog from *Mycobacterium tuberculosis*: a gated mechanosensitive ion channel. *Science* 282:2220-6.

Chung, S. H., T. W. Allen, and S. Kuyucak. 2002. Modeling diverse range of potassium channels with Brownian dynamics. *Biophys. J.* 83:263-77.

Chung, S. H., and S. Kuyucak. 2002. Recent advances in ion channel research. *Biochim. Biophys. Acta* 1565:267-86.

Doyle, D. A., J. Morais Cabral, R. A. Pfuetzner, A. Kuo, J. M. Gulbis, S. L. Cohen, B. T. Chait, and R. MacKinnon. 1998. The structure of the potassium channel: molecular basis of K^+ conduction and selectivity. *Science* 280:69-77.

Dutzler, R., E. B. Campbell, M. Cadene, B. T. Chait, and R. MacKinnon. 2002. X-ray structure of a ClC chloride channel at 3.0 A reveals the molecular basis of anion selectivity. *Nature* 415:287-94.

Egberts, E., S. J. Marrink, and H. J. Berendsen. 1994. Molecular dynamics simulation of a phospholipid membrane. *Eur. Biophys. J.* 22:423-36.

Forrest, L. R., and M. S. P. Sansom. 2000. Membrane simulations: Bigger and better? *Curr. Opin. Struct. Biol.* 10:174-181.

Gu, C. X., P. F. Juranka, and C. E. Morris. 2001. Stretch-activation and stretch-inactivation of Shaker-IR, a voltage-gated K+ channel. *Biophys. J.* 80:2678-93.

Hamill, O. P., and B. Martinac. 2001. Molecular basis of mechanotransduction in living cells. *Physiol. Rev.* 81:685-740.

Heginbotham, L., L. Kolmakova-Partensky, and C. Miller. 1998. Functional reconstitution of a prokaryotic K^+ channel. *J. Gen. Physiol.* 111:741-9.

Heller, H., M. Schaefer, and K. Schulten. 1993. Molecular dynamics simulation of a bilayer of 200 lipids in the gel and in the liquid crystal phases. *J. Phys. Chem.* 97:8343-8360.

Im, W., S. Seefeld, and B. Roux. 2000. A Grand Canonical Monte Carlo-Brownian dynamics algorithm for simulating ion channels. *Biophys. J.* 79:788-801.

Jiang, Y., A. Lee, J. Chen, V. Ruta, M. Cadene, B. T. Chait, and R. MacKinnon. 2003. X-ray structure of a voltage-dependent K^+ channel. *Nature* 423:33-41.

Koprowski, P., and A. Kubalski. 2001. Bacterial ion channels and their eukaryotic homologues. *Bioessays* 23:1148-58.

Maduke, M., D. J. Pheasant, and C. Miller. 1999. High-level expression, functional reconstitution, and quaternary structure of a prokaryotic ClC-type chloride channel. *J. Gen. Physiol.* 114:713-22.

Martinac, B., M. Buechner, A. H. Delcour, J. Adler, and C. Kung. 1987. Pressure-sensitive ion channel in *Escherichia coli*. *Proc. Natl. Acad. Sci.* 84:2297-301.

Maurer, J. A., and D. A. Dougherty. 2001. A high-throughput screen for MscL channel activity and mutational phenotyping. *Biochim. Biophys. Acta* 1514:165-9.

Maurer, J. A., D. E. Elmore, H. A. Lester, and D. A. Dougherty. 2000. Comparing and contrasting *Escherichia coli* and *Mycobacterium tuberculosis* mechanosensitive channels (MscL). New gain of function mutations in the loop region. *J. Biol. Chem.* 275:22238-44.

Miyazawa, A., Y. Fujiyoshi, and N. Unwin. 2003. Structure and gating mechanism of the acetylcholine receptor pore. *Nature* 424:949-55.

Perozo, E., D. M. Cortes, and L. G. Cuello. 1999. Structural rearrangements underlying K^+-channel activation gating. *Science* 285:73-8.

Perozo, E., D. M. Cortes, P. Sompornpisut, A. Kloda, and B. Martinac. 2002. Open channel structure of MscL and the gating mechanism of mechanosensitive channels. *Nature* 418:942-8.

Rees, D. C., G. Chang, and R. H. Spencer. 2000. Crystallographic analyses of ion channels: lessons and challenges. *J. Biol. Chem.* 275:713-6.

Roux, B. 2002. Theoretical and computational models of ion channels. *Curr. Opin. Struct. Biol.* 12:182-189.

Roux, B., and R. MacKinnon. 1999. The cavity and pore helices in the KcsA K+ channel: electrostatic stabilization of monovalent cations. *Science* 285:100-2.

Saimi, Y., B. Martinac, A. H. Delcour, P. V. Minorsky, M. C. Gustin, M. R. Culbertson, J. Adler, and C. Kung. 1992. Patch clamp studies of microbial ion channels. *Methods Enzymol.* 207:681-691.

Sansom, M. S., I. H. Shrivastava, J. N. Bright, J. Tate, C. E. Capener, and P. C. Biggin. 2002. Potassium channels: structures, models, simulations. *Biochim. Biophys. Acta* 1565:294-307.

Sukharev, S., S. R. Durell, and H. R. Guy. 2001. Structural models of the MscL gating mechanism. *Biophys. J.* 81:917-36.

Sukharev, S. I., B. Martinac, V. Y. Arshavsky, and C. Kung. 1993. Two types of mechanosensitive channels in the *Escherichia coli* cell envelope: solubilization and functional reconstitution. *Biophys. J.* 65:177-83.

Sukharev, S. I., M. J. Schroeder, and D. R. McCaslin. 1999. Stoichiometry of the large conductance bacterial mechanosensitive channel of *E. coli*. A biochemical study. *J. Membr. Biol.* 171:183-93.

Tieleman, D. P., and H. J. Berendsen. 1998. A molecular dynamics study of the pores formed by Escherichia coli OmpF porin in a fully hydrated palmitoyloleoylphosphatidylcholine bilayer. *Biophys. J.* 74:2786-801.

Chapter 2: Confirmation of the *M. tuberculosis* MscL Crystal Structure and Comparisons of MscL Homologues

The *M. tuberculosis* MscL Crystal Structure: Unique Opportunities and Ambiguity

Mechanosensation is a central part of numerous biological processes ranging from circulation and hearing in higher animals to maintaining proper osmotic conditions in bacteria (Wood, 1999). One family of bacterial channels gated by membrane tension was first identified and characterized electrophysiologically as the mechanosensitive channels of large, small, and mini conductance (MscL, MscS, and MscM, respectively) (Berrier et al., 1996; Martinac et al., 1987; Sukharev et al., 1993). The first of these to be cloned, *E. coli* MscL (Ec-MscL) (Sukharev et al., 1994), has been the subject of extensive studies including site-directed and random mutagenesis (Blount et al., 1997; Blount et al., 1996b; Ou et al., 1998; Yoshimura et al., 1999), covalent cross-linking (Blount et al., 1996a; Sukharev et al., 1999b), structural probing with IR and CD (Arkin et al., 1998), and extended electrophysiology (Sukharev et al., 1999c). Additionally, homologues from seven varied bacterial species were cloned and found to have mechanosensitive activity analogous to Ec-MscL (Moe et al., 1998). The ability of MscL to rescue an osmotically sensitive bacterium, *V. alginolyticus*, from osmotic downshock supports proposals that MscL acts as a "release valve" to reduce membrane tension during osmotic stress (Nakamaru et al., 1999).

The crystal structure of the *M. tuberculosis* MscL (Tb-MscL) homologue (Fig. 2.1) solved by the Rees group (Chang et al., 1998) gives further insight into previous studies while provoking new questions about MscL. The crystal structure gives unique opportunities for structure-function studies employing a variety of computational and experimental techniques. The relatively small size of MscL and the ability to produce

reasonably large quantities of it from bacterial cultures also makes it a promising model system for studying general principles of mechanosensitive ion channels.

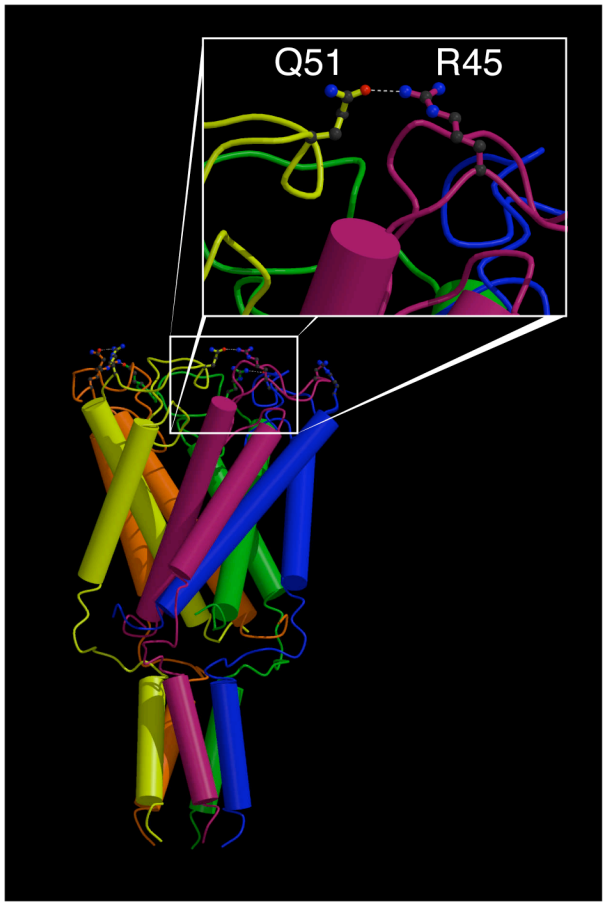

Figure 2.1: The Tb-MscL crystal structure with the five identical subunits shown in different colors. The interaction between Gln 51 and Arg 45 residues on adjacent subunits is highlighted.

However, there is some ambiguity in the crystal structure of Tb-MscL. The crystallization was performed under non-physiological conditions, at low pH and in the presence of heavy metal ions (Chang et al., 1998), which has caused some concern about the relevance of the structure to physiological conditions (Oakley et al., 1999). Additionally, the pentameric structure was at odds with several studies claiming MscL was a homohexamer, including biochemical cross-linking (Blount et al., 1996a; Sukharev

et al., 1999b), estimates of pore size (Cruickshank et al., 1997), and a two-dimensional crystal structure (Saint et al., 1998).

Concerns over Tb-MscL multimerization could be addressed by designing an intersubunit crosslink using the crystal structure. These designed reactions would give a more definitive answer to the multimerization than the use of non-specific crosslinkers. As well, the success of a designed reaction would support the validity of the structure in the region of the design. This would be particularly desirable since the electron density for some regions, such as the loop region, was more ambiguous than for other regions of Tb-MscL, such as the transmembrane helices. Also, as discussed below, the extracellular loop region exhibits interesting sequence diversity among MscL homologues.

An apparent intersubunit hydrogen-bond in the crystal structure between R45 and Q51 can be ideally exploited for designed cross-linking reactions (Fig. 2.1). To this end, an R45K/Q51E mutant was made to allow intersubunit amide bond formation mediated by the peptide bond forming reagents EDC or DCC. However, EDC is known to cause some background cross-linking in wild-type EcMscL (Sukharev et al., 1999b). This led to the production of an R45C/Q51C mutant which can be crosslinked through disulfide bond formation with $Cu(phen)_3$ or with bifunctional bismaleimide crosslinkers of differing lengths: BMOE, BNDB, and BMH. Structures of these crosslinkers are shown in Fig. 2.2. The absence of native cysteines in TbMscL will preclude background reactions for these cases.

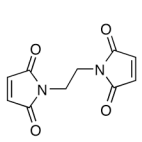

BMOE
Spacer Arm 8.0 Å

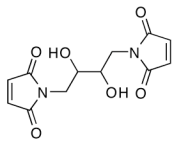

BMDB
Spacer Arm 10.2 Å

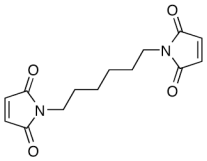

BMH
Spacer Arm 16.1 Å

Figure 2.2: Bis-malimide cross-linking reagents with spacer arms of varying lengths.

Production of MscL Proteins and Cross-linking Protocols

All mutations were generated using the QuikChange Method (Stratagene) on a pET 19b (Novagen) construct containing the *M. tuberculosis* MscL open reading frame (Chang et al., 1998). Mutations were confirmed by enzymatic digest and sequencing. Expression was carried out in a MscL-null strain of BL21(DE3) *E. coli* (Chang et al., 1998). All bacterial growth was done in the presence of 100 □g/mL ampicillin.

Protein expression was performed by growing cells at 37 °C to the midpoint of log phase ($OD_{600} \approx 0.6$-0.8) and inducing with 0.1% IPTG and 1% lactose. Following induction, cells were grown for an additional 2 hours, harvested, and solubilized in 1% DDM, 10 mM TRIS, and 10 mM NaCl. Protein was purified on a nickel-chelation column (Qiagen) in the presence of 0.05% DDM. The resulting proteins were identified by MALDI-TOF mass spectral analysis.

Wild-type or R45K/Q51E protein solubilized in DDM micelles was diluted to a concentration of approximately 25 μg/mL and cross-linked at 4 °C for 2 hours using 10 mM EDC, 10 mM DCC, 10 mM EDC/10 mM Sulfo-NHS, or 10 mM DCC/10 mM NHS. All cross-linking reactions were quenched with SDS-PAGE loading buffer containing □-mercaptoethanol. Reaction products were run on 4-15% gradient polyacrylamide gels

and visualized by Western blotting with either a 6-His Antibody (Amersham) or INDIA HisProbe-HRP (Pierce). Cysteine cross-linking reactions were performed and assayed in a similar manner on wild-type and R45C/Q51C Tb-MscL. In these reactions, thioethers were formed with bis-maleimide reagents (Pierce) or disulfide bond formation was mediated by 3 mM copper phenanthroline. For the disulfide formation reactions with copper phenanthroline, □-mercaptoethanol was omitted from the loading buffer.

Results of Cross-linking Studies

A typical SDS-PAGE Western blot of cross-linking products is shown in Fig. 2.3. All reagents showed at least a weak pentameric band in the mutant with slight background cross-linking in wild-type. The background cross-linking is most likely due to cross-linking in the carboxy terminus of the protein, which contains a number of glutamates, aspartates and lysines.

The most interesting cross-linking results were seen with EDC and Sulfo-NHS. This combination gives mainly pentamer and tetramer for cross-linked products (Fig. 2.3). The strong pentameric band in this designed system provides the best evidence to date that Tb-MscL is pentameric under physiological conditions. Other cross-linking studies typically show progressively weaker band intensities on going from monomer to dimer to trimer, etc., analogous to our results with just EDC and other non-optimal conditions (Fig. 2.3) (Blount et al., 1996a; Hase et al., 1997; Sukharev et al., 1999a). Such observations always leave open the possibility that a hexamer band is present, but is too weak to be seen as the intensity progressively falls off with higher oligomerization. In fact, under some conditions, a weak band assigned to hexamer is occasionally seen in

our reactions. However, with the designed double mutant under appropriate conditions (EDC/Sulfo-NHS), very strong tetramer and pentamer bands are seen, but no hexamer band is visible. This provides compelling evidence that no significant fraction of Tb-MscL is present in hexameric (or higher oligomerization) states when reconstituted in DDM micelles. Most likely, crosslinked complexes with more than five subunits in previous work resulted from cross-linking between subunits in nearby but distinct channels or cross-linking of malformed channels.

Figure 2.3: Cross-linking of the R45K/Q51E mutant of *M. tuberculosis* MscL. Purified wild-type and R45K/Q51E *M. tuberculosis* MscL proteins were cross-linked for 2 hours at 4 ºC using EDC, DCC, EDC with sulfo-NHS, and DCC with NHS. The reactions were quenched with β-mercaptoethanol, run on a 4-15% SDS-polyacrylamide gel and visualized by Western blotting with 6-His antibody.

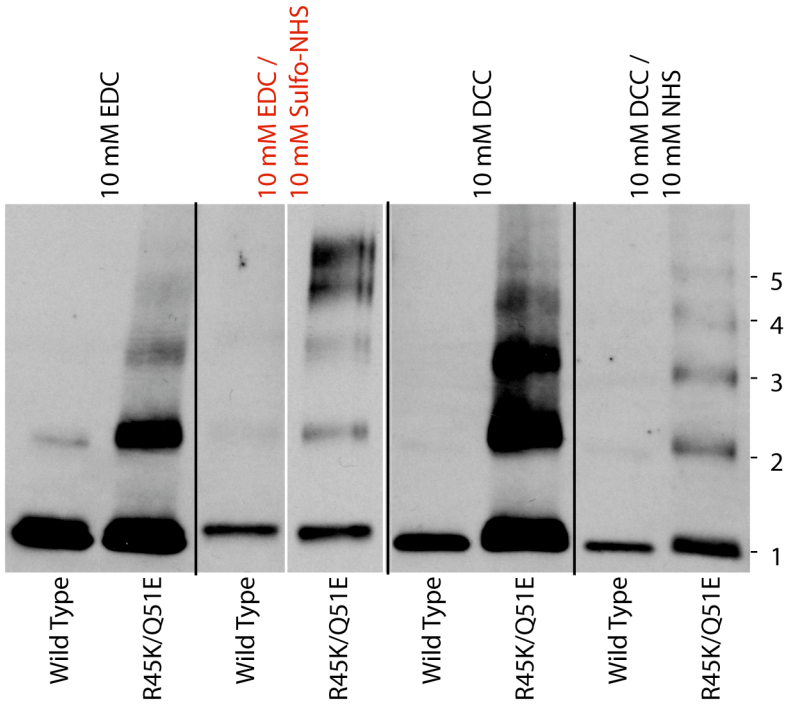

Cross-linking studies using R45C/Q51C Tb-MscL did not produce the quantitative results observed with R45K/Q51E Tb-MscL. However, high molecular weight bands were observed upon cross-linking, either by the formation of disulfide bonds between subunits or by reactions with bis-malimide reagents (Fig. 2.4). Since there are no cysteines other than the designed mutations in MscL, the occurrence of significant cross-linking further supports the crystal structure conformation of the Tb-MscL extracellular loop region. Interestingly, when R45C/Q51C Tb-MscL was cross-linked using bis-malimide reagents of varying tether lengths, no consistent distance dependence was observed for cross-linking efficiency.

Figure 2.4: Cross-linking of the R45C/Q51C mutant of *M. tuberculosis* MscL. Purified wild-type and R45C/Q51C *M. tuberculosis* MscL proteins were cross-linked for 2 hours at 4 ºC using copper phenanthroline, BMH, BMDB, of BMOE. The reactions were run on a 4-15% SDS-polyacrylamide gel and visualized by Western blotting with 6-His antibody. The copper phenathroline reactions were run in the absence of β-mercaptoethanol.

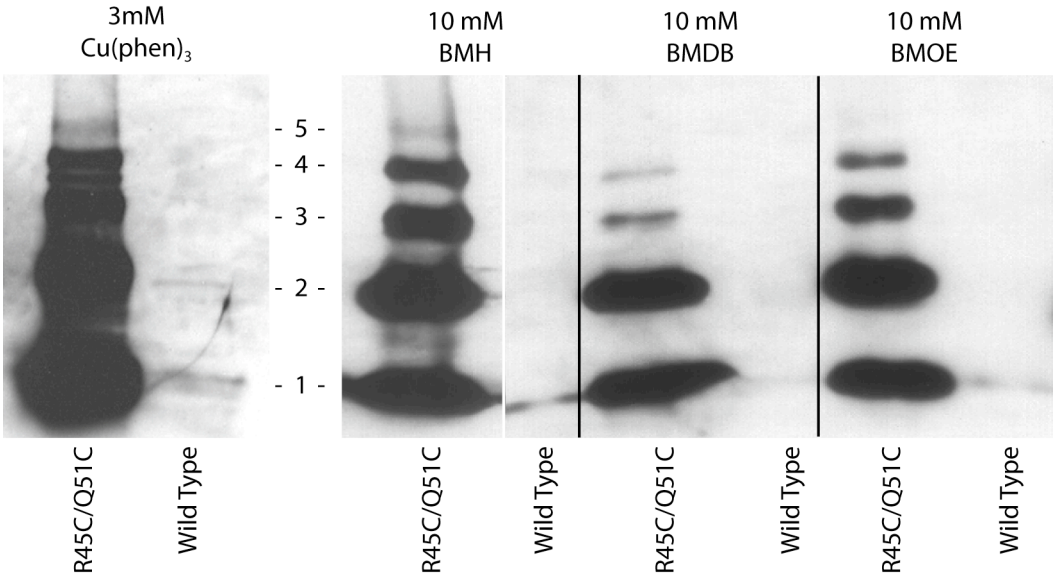

Sequence Analysis of the MscL Channel Family

Since the cross-linking studies helped confirm the crystal structure conformation of Tb-MscL, we began to consider how that channel compared to the well-characterized Ec-MscL and other MscL homologues. One way to perform such comparisons is through bioinformatics methods that compare the primary sequences of different channels and determine the extent of differences between members of the MscL family.

As a first step, the sequences of 35 MscL homologues were obtained from BLAST searches, including searches of several sequenced and partially sequenced bacterial genomes. A multiple sequence alignment of the sequences was obtained using AMPS (Alignment of Multiple Sequences) (Barton, 1990; Barton and Sternberg, 1987). Although clearly related, the mechanosensitive channels from various organisms show moderate to low sequence identities. For example, the sequence identity of Tb-MscL compared to Ec-MscL is 37%, while the sequence identity of *B. bronchiseptica* MscL compared to *M. leprae* MscL is 15%. Therefore, development of an optimal alignment was not straightforward. For this reason, we augmented the sequence alignment approache with MEME analysis (Bailey and Elkan, 1994; Bailey and Gribskov, 1998), which identifies conserved regions within a group of sequences. The AMPS multiple sequence alignment was slightly adjusted to align corresponding MEME groups from different sequences. Fig. 2.5 shows the final multiple sequence alignment and MEME group analysis of the 35 putative MscL sequences. The alignment was divided into regions—extracellular loop, carboxy terminus, and transmembrane regions one and two—using the helix definitions of Chang *et al*. (1998). The extracellular loop is defined as the region between the first and second transmembrane domains, and the carboxy

Figure 2.5: MEME consensus group analysis shown on the AMPS multiple sequence alignment of 35 putative MscL homologues. The colored regions on the sequence alignment indicate the MEME consensus groups.

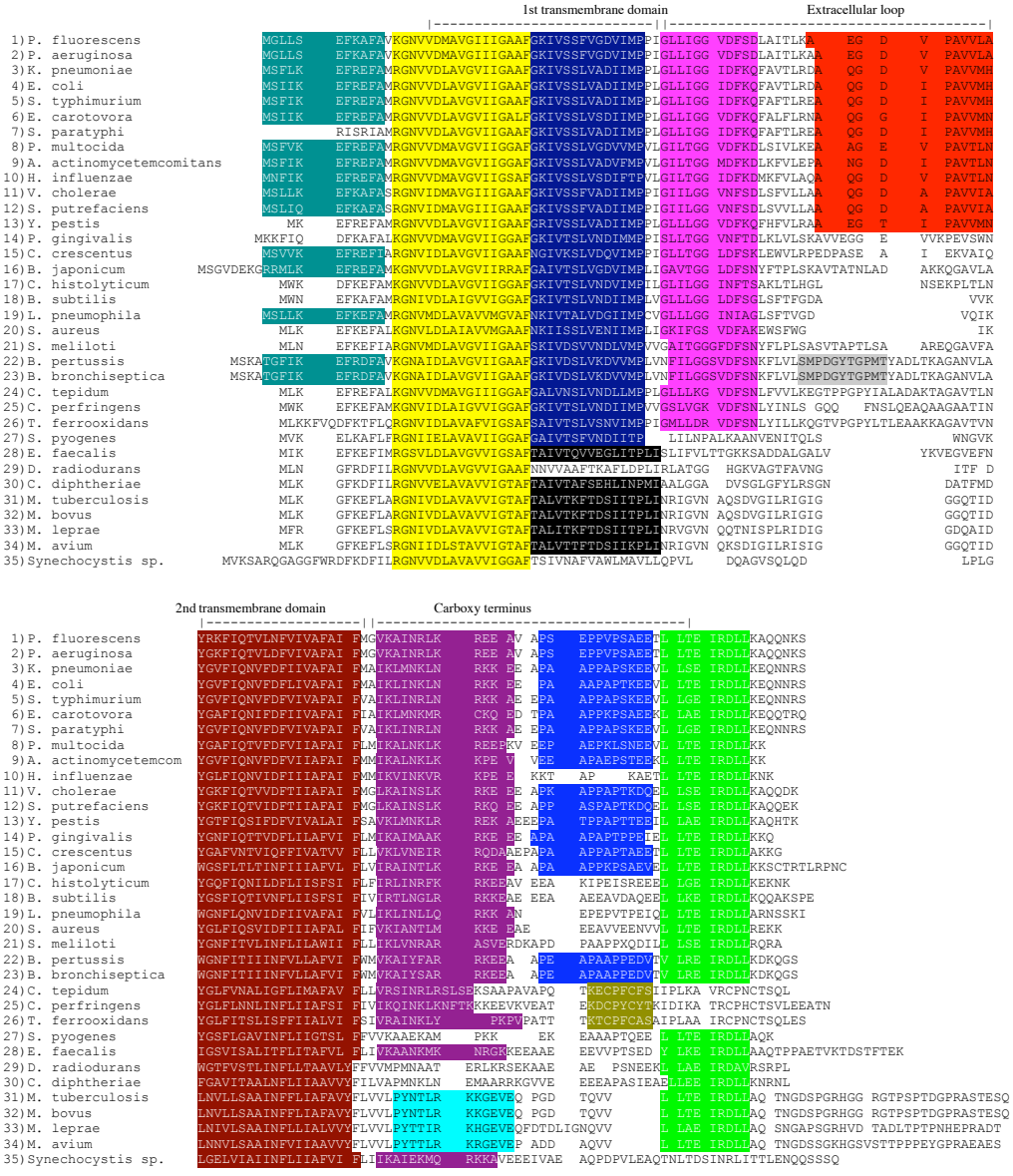

Group Definitions:

- Group I
- Group II
- Group III
- Group IV
- Group V
- Group VI
- Group VII
- Group VIII
- Group IX
- Group X
- Group XI
- Group XII
- Group XIII

terminus is the region from the end of the second transmembrane domain to the end of the carboxy helix.

The MEME sequence analysis gives insight into the overall similarity of the MscL homologues. Not surprisingly, the homologues are most similar in the transmembrane regions and most divergent in the loop and carboxy terminus regions. The strong similarities in the transmembrane domains are highlighted by the fully conserved groups, II and VIII, and the highly conserved group III. Additionally, members of the MscL family that lack group III in the first transmembrane region tend to have a similar conserved group IV in this region.

The carboxy terminus and loop region are much less conserved. Despite the appearance of three consensus groups in the loop region—V, VI and VII—these groups are clearly not universal. The carboxy terminus is more highly conserved than the loop region, containing two very highly conserved groups (IX and XIII), but it is clearly not as well conserved as the transmembrane helices. Mycobacteria do not contain group IX, but an analogous charged region is evident (group X). Previously, it has been shown that a large portion of the carboxy terminus in Ec-MscL can be deleted without affecting protein function (Blount et al., 1996b). Although the same may not be true for all homologues, this is consistent with the lack of sequence conservation in this region.

To further examine the similarities and differences among MscL homologues, a pairwise alignment of the various regions, such as the first and second transmembrane domains, the extracellular loop, and the carboxy terminus, was employed. Pairwise alignments of the various regions were performed using AMPS, and scores for each pair were summarized as contour plots. Scores reflect the alignment of sequence A to

sequence B relative to a shuffled sequence B and are therefore corrected for length. Scores above 5 indicate very good alignment between two protein sequences, scores between 2 and 5 indicate moderate alignment, and scores below 2 indicate poor alignment. Contour plots showing scores for the AMPS pairwise alignments of the first transmembrane domain, the extracellular loop, and the carboxy terminus are shown in (Fig. 2.6).

The pairwise alignments showed the same general trends observed with MEME analysis. In general, all regions of the MscL sequence are conserved, however the loop region has pairs of sequences with poor alignment. To some extent the sequence pairs within the loop region can be used to group the homologues into subfamilies. The largest and most obvious subfamily includes *E. coli* MscL and other sequences containing MEME group VI. Another distinctive subfamily includes the Mycobacteria. Thus, based on their primary sequences, Ec-MscL and Tb-MscL appear to reside in different subfamilies.

Figure 2.6: Regional AMPS pairwise alignments for the first transmembrane domain (*A*), the loop region (*B*), and the carboxyl terminus (*C*). Numbers on axes correspond to the sequence numbers in Figure 2.5. The grouping of sequences into two main subfamilies can be seen for the loop region (*B*), with a large subfamily containing Ec-MscL and a small subfamily containing Tb-MscL.

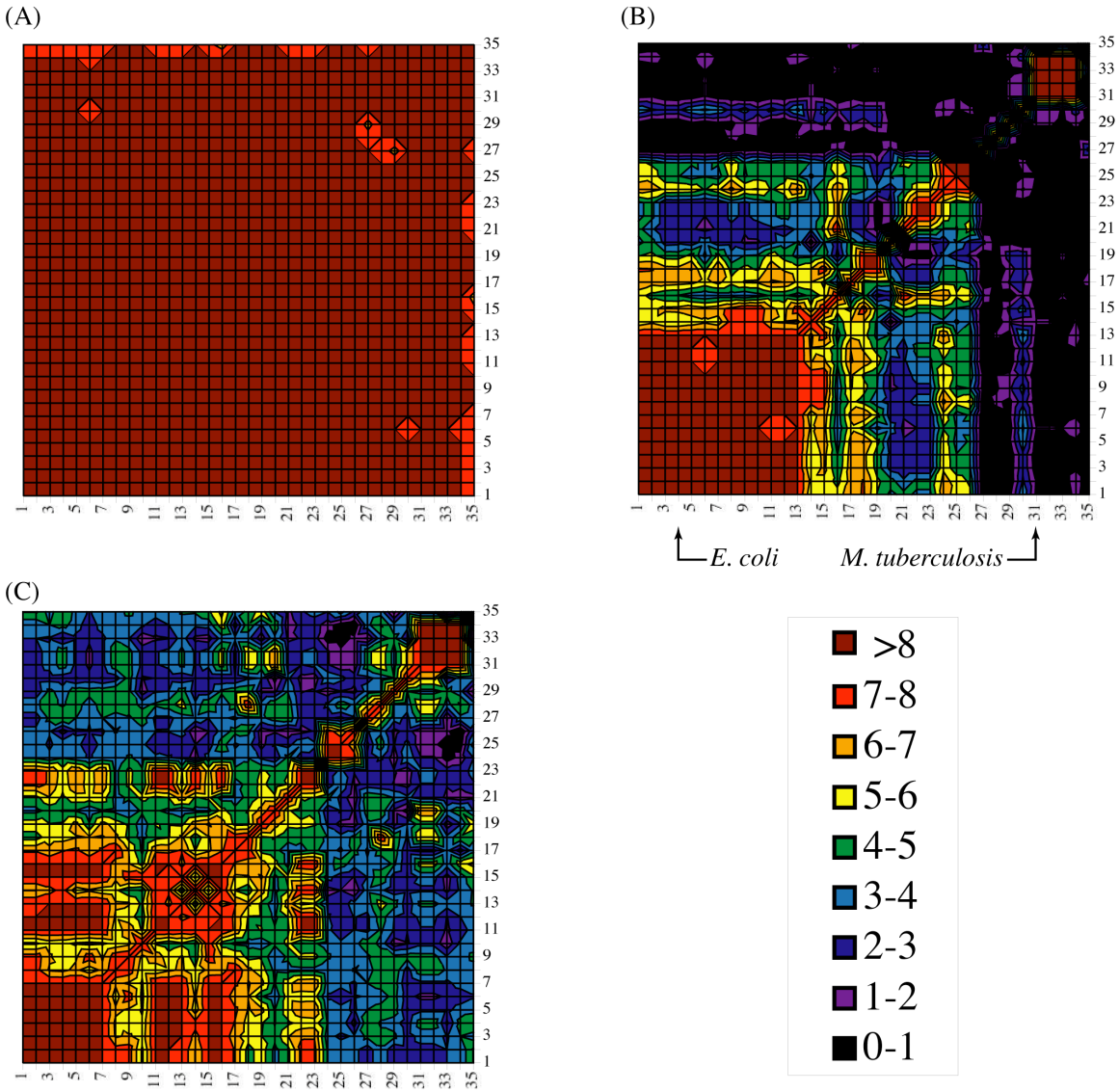

Analysis of the MscL Channel Family with Circular Dichroism

The secondary structure of MscL homologues was also compared using circular dichroism to measure relative helicity. To do this, protein samples were purified for the nine different MscL homologues that have been characterized by electrophysiology (Moe et al., 1998; Moe et al., 2000). This protein purification was done using the same methods described above to produce MscL proteins for cross-linking reactions. These protein samples were then used to obtain circular dichroism spectra on an Aviv 42a DS circular dichroism spectrometer using a strain-free circular cuvette with a pathlength of 0.1 cm. Spectra were collected between 260 nm and 185 nm and averaged over three scans. All data were collected at room temperature. Concentrations for conversion to molar ellipticy units were obtained using the BioRad DC compatible protein concentration kit and the Pierce BCA protein concentration kit.

The spectra obtained for these homologues are shown in Fig. 2.7, and selected features are listed in Table 2.1. As observed with the sequence alignment of MscL homologues, the homologues fall into two distinct families. However, the families resulting from the circular dichroism studies are different than those observed from the sequence alignment data. Based on the observed circular dichroism spectra, the first family is composed of *E. coli*, *H. influenza*, and *P. fluorescens* and the second family is composed of *M. tuberculosis*, *E. carotovora*, *C. perfringens*, *S. aureus*, *B. subtilis*, and *Synechocytis sp.*

Figure 2.7: Circular dichroism spectra for nine different MscL homologues. Two groups of channels are observed from the CD data, one with apparently more and one with less -helicity. From this analysis, Ec-MscL and Tb-MscL are in different groups. Abbreviations for the homologues are given in Table 2.1

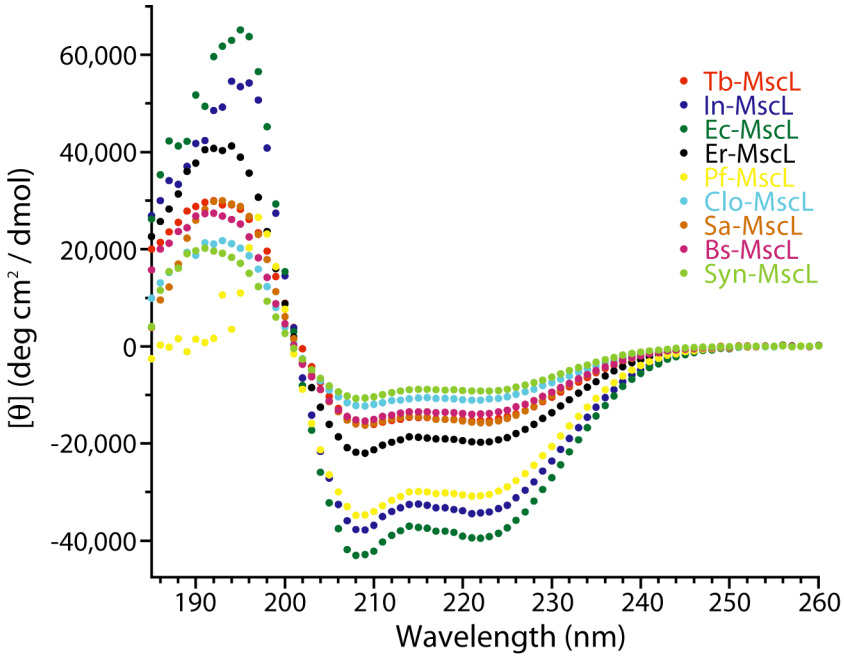

Using the elipticity at 222 nm observed in the circular dichroism spectra, the percent helicity of each MscL homologue was estimated as previously described for Ec-MscL (Table 2.1) (Arkin et al., 1998). The two sequence families show dramatic differences in their predicted helical content, with the first family exhibiting helical contents of 85-110% and the second family having a helical content between 25% and 55%.

To determine if the relative helicity values were predicted from differences in primary sequence, the amount of helix in each homologue was predicted using Jpred, a program that combines results from several independent secondary structure prediction methods. The predicted helicity values obtained for the MscL homologues using Jpred

are quite similar (Table 2.1), and would not predict two families as observed. It is true that the highest predicted value is for In-MscL, which lies in the Ec-MscL family, and the lowest predicted value is for Clo-MscL, which lies in the Tb-MscL family. However, in general, there is no trend between predicted helical secondary structure and the helical content determined by circular dichroism. In fact, it should be noted that Pf-MscL, which is in the Ec-MscL family with high apparent helicity, exhibits one of the lowest values for predicted helicity. This inconsistency could point to a flaw in Jpred for predicting □-helicity for MscL homologues. However, other structural features, such as tertiary structure and quaternary assembly, can affect observed circular dichroism signals. Thus, the differences in CD spectra could result from different folding or assembly of some portion of MscL channels in different subfamilies.

Table 2.1: A summary of the circular dichroism specra for various homologues of MscL. Helical content for the various MscL homologues was determined from the abosorbance in the CD spectrum at 222 nm using the method previously described for Ec-MscL (Arkin et al., 1998). Jpred predictions of helical content are based on sequence analaysis.

Species	Abbreviation	Sequence number	Helical Content from CD	Helical Content from Jpred
P. fluorescens	Pf	1	85-51%	48%
H. influenza	In	10	95-57%	56%
E. coli	Ec	4	110-66%	53%
E. carotovora	Er	6	55-33%	49%
M. tuberculosis	Tb	31	42-25%	45%
C. perfringens	Clo	25	31-18%	35%
S. aureus	Sa	20	44-26%	50%
B. subtilis	Bs	18	39-23%	52%
Synechocystis sp.	Syn	35	25-15%	50%

Since MscL homologues vary considerably in length from 143 amino acids to 175 amino acids, the observed helicity could be related to protein length. Fig. 2.8 shows a

plot of the maximal helicity predicted for each homologue as a function of homologue length. Clearly, the predicted helicity from circular dichroism does not correlate with protein length. The longest and shortest homologues both lie in the Tb-MscL family that displays relatively low helicity.

Figure 2.8: Comparison of protein length to the maximal predicted helical content for the various homologues of MscL . No clear trends between protein length and helical content are observerd.

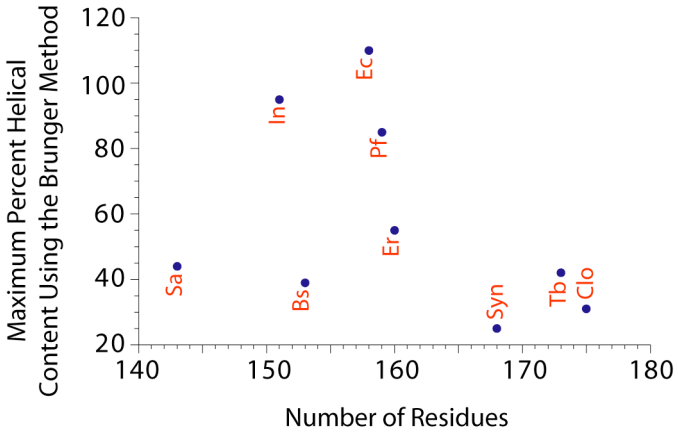

Interestingly, although Tb-MscL and Ec-MscL are in different MscL sub-families in both the sequence comparisons and CD analysis, the CD-based sub-families are somewhat different than those in the sequence analysis. As well, on the surface the Tb-MscL family from CD is composed of seemingly poorly related sequences. For example, some of the sequences in the Tb-MscL family contain MEME group V and/or MEME group XII, while other members lack these groups. Nonetheless, all of the members of the Ec-MscL family contain MEME group VI, which is located in the loop region. Similarly, none of the members of the Tb-MscL family, except for Er-MscL, contain

MEME group VI. Additionally, Er-MscL has the largest helicity of the Tb-MscL family. Thus, the structural differences between homologue subfamilies observed by CD may be due to interactions in the second half of the extracelluar loop region. Future studies of MscL channels with chimera loop regions could give insight into this possibility.

Summary

The absence of crosslinked protein with greater multimerization than pentamer supports the formation of a pentameric MscL structure under physiological conditions. Also, these results provide an important biochemical verification of the crystal structure in a relatively ambiguous region. This implies that the structure can be used as a basis for interpreting previous experimental data on MscL. As well, the success of the designed reactions shows that the Tb-MscL crystal structure could be used as a basis for other design efforts on the channel.

Using the sequence alignment in Figure 2.5, there is no obvious Ec-MscL analogue to the R45•••Q51 hydrogen bond seen in Tb-MscL. Technically, the alignment is L47/D53 (Ec-MscL numbering), which is not a favorable interaction. There is no cationic or hydrogen bond donating residue near L47 that could pair with D53. However, residues on either side of D53 are hydrophobic, suggesting that perhaps the ion pair of Tb-MscL is replaced by a hydrophobic contact such as L47/I52 or L47/F54 in Ec-MscL. Thus, in addition to investigating the physiological role of the R45•••Q51 interaction in Tb-MscL, it would be interesting to investigate the role of potentially analogous interactions in Ec-MscL. Also, these putative hydrophobic residue pairs in the Ec-MscL

loop may provide a site for design of a cross-linking reaction similar to that designed for Tb-MscL.

The differences among the families of MscL homologues obtained from sequence analysis and circular dichroism are quite intriguing. In particular, it is interesting that Tb-MscL and Ec-MscL consistently lie in different subfamilies. Thus, although there are clear overall similarities between those homologues, researchers may need to be careful before assuming results on one channel necessarily refect on the other. In fact, electrophysiological measurements have shown that Tb-MscL opens at a much greater tension than Ec-MscL in *E. coli* spheroplasts (Moe et al., 2000). Additional studies comparing members of different MscL subfamilies in detail could give further insights into how differences in sequence and helicity affect channel function.

References

Arkin, I. T., S. I. Sukharev, P. Blount, C. Kung, and A. T. Brunger. 1998. Helicity, membrane incorporation, orientation and thermal stability of the large conductance mechanosensitive ion channel from *E. coli*. *Biochim. Biophys. Acta-Biomembr*. 1369:131-140.

Bailey, T. L., and C. Elkan. Fitting a mixture model by expectation maximization to discover motifs in bioploymers.; 1994; Menlo Park, California. AAAI Press. p 28-36.

Bailey, T. L., and M. Gribskov. 1998. Combining evidence using p-values: application to sequence homology searches. *Bioinformatics* 14:48-54.

Barton, G. J. 1990. Protein multiple sequence alignment and flexible pattern-matching. *Method Enzymol*. 183:403-428.

Barton, G. J., and M. J. E. Sternberg. 1987. A strategy for the rapid multiple alignment of protein sequences—confidence levels from tertiary structure comparisons. *J. Mol. Biol*. 198:327-337.

Berrier, C., M. Besnard, B. Ajouz, A. Coulombe, and A. Ghazi. 1996. Multiple mechanosensitive ion channels from *Escherichia coli* activated at different thresholds of applied pressure. *J. Membrane Biol.* 151:175-187.

Blount, P., M. J. Schroeder, and C. Kung. 1997. Mutations in a bacterial mechanosensitive channel change the cellular response to osmotic stress. *J. Biol. Chem.* 272:32150-32157.

Blount, P., S. I. Sukharev, P. C. Moe, M. J. Schroeder, H. R. Guy, and C. Kung. 1996a. Membrane topology and multimeric structure of a mechanosensitive channel protein of *Escherichia coli*. *EMBO J.* 15:4798-4805.

Blount, P., S. I. Sukharev, M. J. Schroeder, S. K. Nagle, and C. Kung. 1996b. Single residue substitutions that change the gating properties of a mechanosensitive channel in *Escherichia coli*. *Proc. Natl. Acad. Sci. USA* 93:11652-11657.

Chang, G., R. H. Spencer, A. T. Lee, M. T. Barclay, and D. C. Rees. 1998. Structure of the MscL homolog from *Mycobacterium tuberculosis*: a gated mechanosensitive ion channel. *Science* 282:2220-6.

Cruickshank, C. C., R. F. Minchin, A. C. LeDain, and B. Martinac. 1997. Estimation of the pore size of the large-conductance mechanosensitive ion channel of *Escherichia coli*. *Biophys. J.* 73:1925-1931.

Hase, C. C., R. F. Minchin, A. Kloda, and B. Martinac. 1997. Cross-linking studies and membrane localization and assembly of radiolabelled large mechanosensitive ion channel (MscL) of *Escherichia coli*. *Biochem. Biophys. Res. Commun.* 232:777-782.

Martinac, B., M. Buechner, A. Delcour, J. Adler, and C. Kung. 1987. Pressure-sensitive ion channel in *Escherichia coli*. *Proc. Natl. Acad. Sci. USA* 84:2297-2301.

Moe, P. C., P. Blount, and C. Kung. 1998. Functional and structural conservation in the mechanosensitive channel MscL implicates elements crucial for mechanosensation. *Mol. Microbiol.* 28:583-592.

Moe, P. C., G. Levin, and P. Blount. 2000. Pursuing the roots of mechanosensation: A structure-based genetic analysis of the *M. tuberculosis* MscL channel. *Biophys. J.*

Nakamaru, Y., Y. Takahashi, T. Unemoto, and T. Nakamura. 1999. Mechanosensitive channel functions to alleviate the cell lysis of marine bacterium, *Vibrio alginolyticus*, by osmotic downshock. *FEBS Lett.* 444:170-172.

Oakley, A. J., B. Martinac, and M. C. J. Wilce. 1999. Structure and function of the bacterial mechanosensitive channel of large conductance. *Protein Sci.* 8:1915-1921.

Ou, X. R., P. Blount, R. J. Hoffman, and C. Kung. 1998. One face of a transmembrane helix is crucial in mechanosensitive channel gating. *Proc. Natl. Acad. Sci. USA* 95:11471-11475.

Saint, N., J. J. Lacapere, L. Q. Gu, A. Ghazi, B. Martinac, and J. L. Rigaud. 1998. A hexameric transmembrane pore revealed by two-dimensional crytalization of the large mechanosensitive ion channel (MscL) of *Escherichia coli. J. Biol. Chem.* 273:14667-14670.

Sukharev, S., M. J. Schroeder, and D. R. McCaslin. 1999a. Re-examining the multimeric structure of the large conductance bacterial mechanosensitive channel, MscL. *Biophys. J.* 76:A138-A138.

Sukharev, S. I., P. Blount, B. Martinac, F. R. Blattner, and C. Kung. 1994. A large-conductance mechanosensitive channel in *E. coli* encoded by MscL alone. *Nature* 368:265-268.

Sukharev, S. I., B. Martinac, V. Y. Arshavsky, and C. Kung. 1993. Two types of mechanosensitive channels in the *Escherichia-coli* cell-envelope—Solubilization and functional reconstitution. *Biophys. J.* 65:177-183.

Sukharev, S. I., M. J. Schroeder, and D. R. McCaslin. 1999b. Stoichiometry of the large conductance bacterial mechanosensitive channel of *E. coli.* A biochemical study. *J. Membrane Biol.* 171:183-193.

Sukharev, S. I., W. J. Sigurdson, C. Kung, and F. Sachs. 1999c. Energetic and spatial parameters for gating of the bacterial large conductance mechanosensitive channel, MscL. *J. Gen. Physiol.* 113:525-539.

Wood, J. M. 1999. Osmosensing by bacteria: Signals and membrane-based sensors. *Microbiol. Mol. Biol. Rev.* 63:230-262.

Yoshimura, K., A. Batiza, M. Schroeder, P. Blount, and C. Kung. 1999. Hydrophilicity of a single residue within MscL correlates with increased channel mechanosensitivity. *Biophys. J.* 77:1960-1972.

Chapter 3: Computational and Experimental Investigation of the C-terminal Region of *M. tuberculosis* MscL

Background

Although cross-linking data in the previous chapter supported the overall crystal structure conformation of Tb-MscL, there are still some ambiguities in the structure. For example, the crystal structure revealed Tb-MscL to be a homopentamer with an □-helical bundle formed by the intracellular C-terminal regions of each subunit (Fig. 3.1). This region has several acidic residues (Asp and Glu) which would be expected to repel one another electrostatically in a bundled structure at physiological pH. However, the crystallization protocol that succeeded in producing acceptable crystals involved a relatively low pH (3.6-3.8) (Chang et al., 1998; Spencer et al., 1999), which would protonate Asp and Glu, potentially reducing their repulsion and stabilizing the □-helical bundle structure. It is thus interesting to consider the extent to which charge neutralization resulting from low pH may have influenced this interesting structural element.

This chapter discusses both computational and experimental work addressing the effect of these charged residues on the conformation of the C-terminal region of MscL. The computational simulations suggest that the observed C-terminal helical bundle conformation may have resulted from the low pH crystallization conditions. In addition, they predict specific mutations that would promote the helix bundle conformation. The effect of these and other mutations on the structural stability of the channel was then tested experimentally using thermal melts monitored by circular dichroism (CD).

Figure 3.1: (*A*) Tb-MscL crystal structure, highlighting the C-terminal helical bundle. Acidic and basic residues in the region are shown in red and blue CPK, respectively. (*B*) Simulation system for MD simulations of the Tb-MscL C-terminal region. The channel is shown as white ribbon with water as blue wireframe and Na^+ and Cl^- ions in green and yellow CPK.

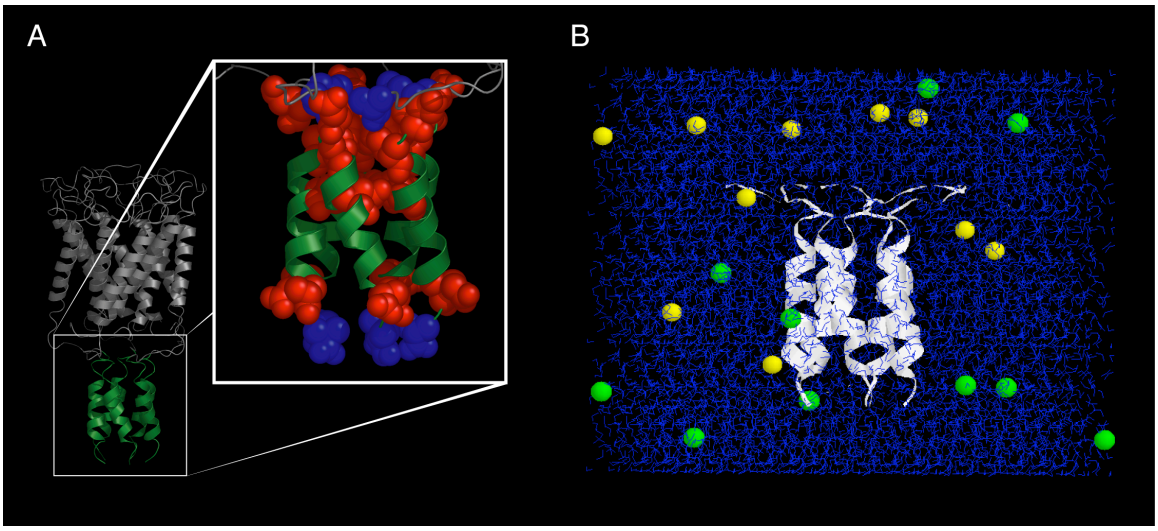

Methods for Computational Modeling of the C-terminal Region

Simulations of the C-terminal region used residues Tyr 94-Arg 118 from all five subunits of the Chang et al. (1998) crystal structure (1MSL) as a starting conformation. Uncharged N- and C-termini (-NH_2 and -COOH) were used, as neither end is a real protein terminus, and the additional charges could cause spurious interactions. Two simulations were performed, which we will refer to as pH 7 and low pH. For the pH 7 simulation, all ionizable residues (Asp, Glu, Lys, and Arg; no His are involved) in the protein were charged. Neutral forms of Asp and Glu were used in the low pH simulation. Additional simulations were performed with various Glu/Gln and Asp/Asn mutations. These were made to the original crystal structure by changing the second acidic O atom

of a residue to an amide N in all five subunits. All remaining ionizable residues were charged in these mutant simulations. These protein structures were then solvated by a box of SPC waters extending 1 nm from the protein in the X, Y, and Z directions. Ions were added randomly to these boxes: 10 Na^+ and 10 Cl^- ions for pH 7, 20 Cl^- ions for low pH, 7 Na^+ and 12 Cl^- for single mutations and 5 Na^+ and 15 Cl^- for the double mutant. These ions were added both to neutralize the charge in the low pH box and to maintain an approximately equal ionic strength between the simulations. The simulations included a total of about 27000 atoms, and after equilibration the system boxes were approximately 6.8 nm x 6.8 nm x 6 nm.

These structures were minimized for 50 steps of steepest descents minimization to reduce close contacts. Minimization was followed by a MD simulation which heated the system to 310 K over 20 ps; after heating all simulations were performed at 310 K. This and all subsequent MD runs on these systems included restraints on the Cα atoms of the two N-terminal residues of each subunit to represent conformational restrictions imposed by the overall assembly of the channel. All MD runs used a timestep of 2 fs along with the LINCS routine to constrain bond lengths (Hess et al., 1997) and SETTLE to constrain water geometries (Miyamoto and Kollman, 1992). Lennard-Jones and short-range Coulombic interactions were cutoff at 1.0 nm, and long-range electrostatics were calculated with particle-mesh Ewald methods, using Fourier grid spacing of 0.10 nm and cubic interpolation. The NPT ensemble with periodic boundary conditions was employed for all runs with isotropic pressure coupling to 1 bar and a coupling constant (τ_p) of 1.0 ps (Berendsen et al., 1984). All minimizations and MD simulations were performed using GROMACS 2.0 (Berendsen et al., 1995) with standard GROMACS parameters.

Analyses of the trajectories were primarily performed with tools included in the GROMACS suite (Berendsen et al., 1995). Properties were averaged over the last 1000 ps of trajectories. Additionally, the DSSP program was used to determine secondary structure (Kabsch and Sander, 1983).

The Effect of pH on the C-terminal Helix Bundle in MD Simulations

The pH 7 and low pH trajectories were noticeably different from one another. The pH 7 simulation had a much larger Cα RMS deviation from the crystal structure than the one at lower pH, showing the overall conformation was more preserved in the lower pH simulation (Fig. 3.2*A*). Although these 1.5 ns simulations are not particularly lengthy, computed RMS fluctuations may give qualitative insight into the relative stabilities of the trajectories, and the low pH case did exhibit consistently lower Cα RMS fluctuations for the majority of the structure (Fig. 3.2*B*).

In addition, the α-helical secondary structure is much better preserved in the low pH simulation, while many of the α-helices have been largely eroded by the end of the pH 7 trajectory. This can be seen by DSSP analysis per residue over the trajectories (Fig. 3.3), and from the final structures in Fig. 3.4. In the pH 7 simulation, the acidic groups appear to have repulsed each other, leading to the overall deformation of the crystal structure conformation. Such a repulsion is not seen with the neutralized residues in the low pH case, as can be seen by multiple Glu 104 and Asp 108 side chains pointing towards one another in the final structure.

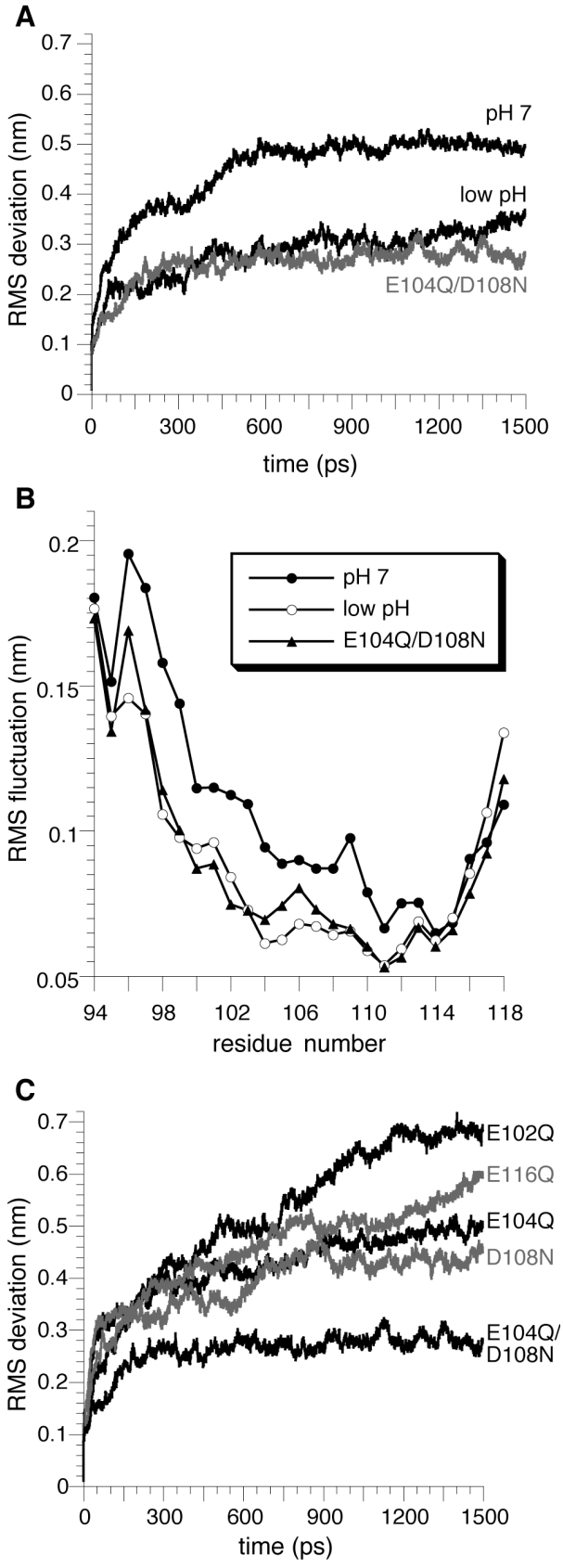

Figure 3.2: (*A*) RMS deviation of Cα from the crystal structure for the pH 7, low pH, and E104Q/D108N C-terminal region simulations, calculated for each frame after fitting the trajectory Cα to the crystal structure. (*B*) RMS fluctuation of Cα around an average structure for C-terminal region simulations plotted per residue. The computed RMS fluctuation is averaged over the five chains. Single mutant fluctuations are omitted for clarity. Values for the E102Q and E116Q simulations were generally in the range of the pH 7 simulation, while E104Q and D108N showed lower fluctuations than pH 7 from the N-terminus to the mutation sites. (*C*) RMS deviation of Cα from the crystal structure for amide mutation trajectories, calculated as described in *A*.

Figure 3.3: Analysis of secondary structure for the C-terminal region simulations performed with the DSSP method for the pH 7, low pH, and E104Q/D108N simulations. Black portions represent residues that are α-helical at a given point in the trajectories. Results for one representative "subunit" from each trajectory is shown.

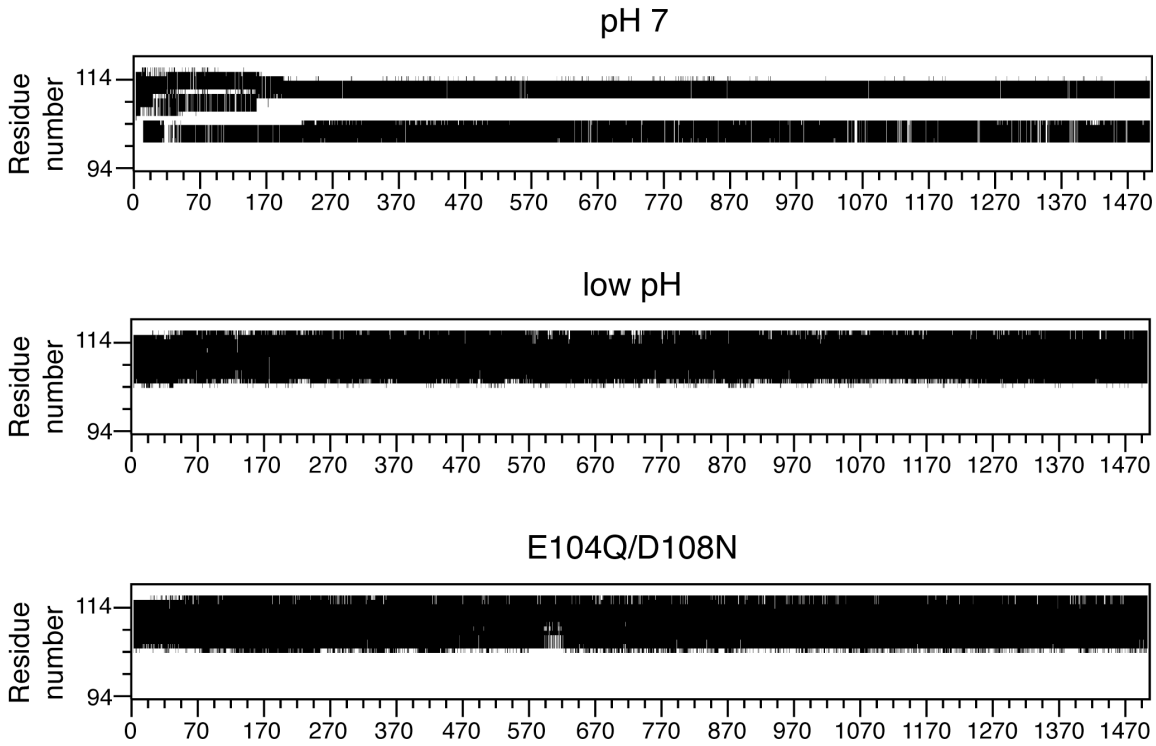

The present simulations suggest that the intracellular helix bundle of Tb-MscL was stabilized by the low pH of the crystallization medium, a possibility suggested by Rees and co-workers (Chang et al., 1998; Spencer et al., 1999). However, such a helix bundle might still be physiologically relevant, perhaps stabilized by binding to metal ions or polyamines. In a case where many acidic residues are constrained into close proximity they could exhibit a shifted pKa, causing some or all to remain protonated under physiological conditions. In fact, experimental data discussed below implies that such pKa shifts might occur to some, but likely not all, residues in the region. The region might also be stabilized by protein-lipid interactions, as discussed in Chapter 5.

Figure 3.4: Ribbon diagrams of the final frames (1500 ps) of the pH 7, low pH and E104Q/D108N C-terminal region simulations. The analogous region of the crystal structure is also shown. In all structures, the acidic residues (or their mutated amide counterparts) are shown in CPK.

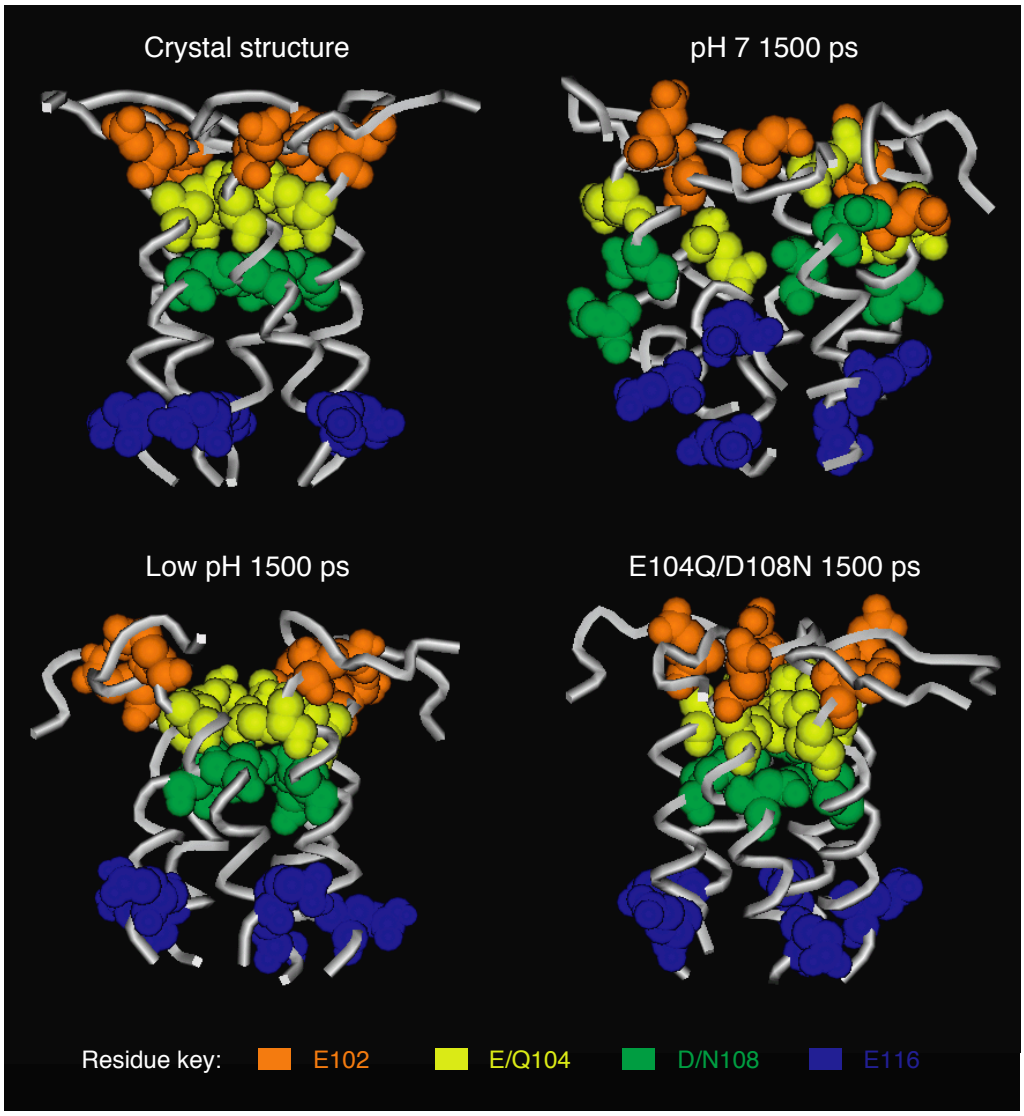

Additionally, ambiguity in the physiological conformation of the C-terminal helical bundle does not imply any uncertainty in the overall pentameric channel conformation observed in the crystal structure. In fact, the crystal structure

conformation, particularly that of the TM helices, was well preserved in simulations of the channel described in Chapters 4 and 5 with ionized side chain protonation states.

The Effect of Mutations to the C-terminal Helix Bundle in Computations

In order to determine if diminishing electrostatic repulsions in the C-terminal region could stabilize the helix bundle at pH 7, we have selectively converted acidic residues (Glu and Asp) to their amide counterparts (Gln and Asn). These Asn and Gln side chains would be extremely similar sterically and electrostatically to protonated Asp and Glu. Thus, trajectories for the C-terminal region with single mutations of all four acidic residues (E102Q, E104Q, D108N, and E116Q) were computed. For the most part these single mutations led to trajectories similar to that of the wild-type pH 7 simulation, as measured by Cα RMS deviation from the crystal structure (Fig. 8.2*C*), Cα RMS fluctuation, and secondary structure conservation by DSSP (data not shown). However, visual inspection of the E104Q and D108N trajectories did indicate that these mutations did somewhat conserve the helical bundle, albeit far less than seen in the low pH situation. As well, there was some reduction in Cα RMS fluctuation from the N-terminus to the mutation site in each of those simulations (data not shown).

These hints of partial stabilization with the E104Q and D108N mutations led us to perform an additional trajectory with a E104Q/D108N double mutant. As can be seen by Cα RMS deviation (Fig. 3.2*C*), Cα RMS fluctuation (Fig. 3.2*B*), and DSSP secondary structure determination (Fig. 3.3), the combined effect of the two mutations led to a trajectory equivalent to that of the low pH simulation. The final structure from the

E104Q/D108N simulation is also strikingly similar to that from the low pH simulation (Fig. 3.4).

Thus, an E104Q/D108N double mutation may have similar effects to low pH conditions on the structure of the Tb-MscL C-terminal helix bundle. As well, mutations of the other charged residues in the region may alter structural stability. Therefore, we attempted to experimentally investigate the effects of this and other mutations on MscL structural stability.

Experimental Production of MscL with C-terminal Mutations

The Tb-MscL channel was encoded in the pET 19b vector, and protein expression was performed in MscL null *E. coli* BL21 cells (Chang et al., 1998; Maurer et al., 2000). The pET 19b vector provides ampicillin resistance and IPTG control over protein expression. Site-directed mutagenesis of the channel was performed using the QuikChange protocol (Stratagene, La Jolla, CA) in order to make mutations to charged residues throughout the C-terminal region: K100Q, E102C, E104Q, D108N, E116Q, E116D, R118Q, D119N, D127N, D142N, and E149Q. As well, a few additional mutations were made to non-charged residues: L113I, T115A, L117I, and L121I. All mutants were verified by sequencing and enzymatic digestion.

For the production of channel protein, frozen permastocks of Tb-MscL or Tb-MscL mutations were used to inoculate 25 mL of LB media with 100 μg/mL ampicillin. The cultures were grown overnight at 37˚C with shaking, and were then used to inoculate 500 mL of TB media with ampicillin. The resulting TB cultures were grown to mid-log phase and then induced with 1 mM IPTG. After induction, the cultures were grown for

an additional 2 hours at 37 ˚C or in some cases for 3 hours at 30 ˚C. Bacteria were then pelleted, and resuspended in 50 mM Tris / 75 mM NaCl / 1% β-dodecyl maltoside (DDM) at pH 7.5 (10 mL) with Complete protease inhibitor cocktail (Roche, Indianapolis, IN). The suspensions were then probe sonicated (4 x 30 Sec.) and incubated with shaking for 1 hour at 37˚C. Following incubation, the suspensions were pelleted at 45,000 x g for 45 minutes and the resulting supernate was passed through a 0.2 μm filter. The L117I and R118Q mutant proteins showed extensive proteolysis of the carboxyl terminal tail that was not observed for other proteins. Therefore, they could not be produced in sufficient quantities for CD thermal melts.

All chromatography steps for protein purification were carried out on a Vision Workstation (Applied Biosystems, Foster City, CA). The clarified supernate was subjected to two-dimensional chromatography, using a POROS metal chelate affinity column (Applied Biosystems, Foster City, CA) charged with cobalt chloride in the first dimension and a POROS HQ anion exchange column (Applied Biosystems, Foster City, CA) in the second dimension. Elution from the metal chelate column was achieved using an imidazole gradient (0.25 mM-1 M at pH 7.5) with 0.05% DDM and elution from the HQ column was achieved using a sodium chloride gradient (0 mM-1 M) in the presense of 10 mM Tris at pH 7.5 and 0.05% DDM. Buffer exchange and desalting were then performed using a HiPrep 26/10 desalting column (Amersham Pharmacia Biotech, Piscataway, NJ) charged with 1 mM phosphate buffer and 0.05% DDM at pH 7.2.

Characterization of MscL Mutants with Thermal Melts

Thermal denaturation was used to investigate if the Tb-MscL C-terminal mutants caused structural perturbations in addition to inducing functional changes. All thermal denaturation was performed using an Aviv 62 DS circular dichroism spectrophotometer (Aviv Instruments, Lakewood, NJ). Purified Tb-MscL protein samples were diluted to approximately identical concentrations in 1 mM phosphate buffer (pH 7.2) for thermal denaturation. Circular dichroism scans (260-195 nm) showed equivalent helical propensities between samples. The denaturation consisted of heating from 25 °C to 95 °C, stepping every 2.5 °C, and allowing the sample to equilibrate at each temperature for 5 min. After equilibration, the ellipticity of samples at 220 nm was measured, averaging the signal over 30 s.

The denaturation curve for wild-type Tb-MscL shows a single melting transition (T_m) around 60 °C (Fig. 3.6). A reduction of 35% in the CD signal is observed between 25 °C and 95 °C. Thus, significant helicity remains in the sample even after the observed transition, which most likely corresponds to the transmembrane domains. After melting, Tb-MscL regains the majority (>90%) of its original elipticity upon returning to 25 °C.

The Tb-MscL C-terminal mutant denaturation curves were qualitatively similar to that of wild type. However, changes in T_m arose for some mutants. In particular, a major shift in T_m to a lower temperature was noted for E116D. Interestingly, an analogous shift was *not* noted for the E116Q mutation. In other words, shortening the carboxylic acid side chain by one methylene unit resulted in a dramatic change in structural stability, while neutralizing the charge on the residue had no effect on stability. Thus, it seems likely that this residue plays an important steric role in the C-terminal structure.

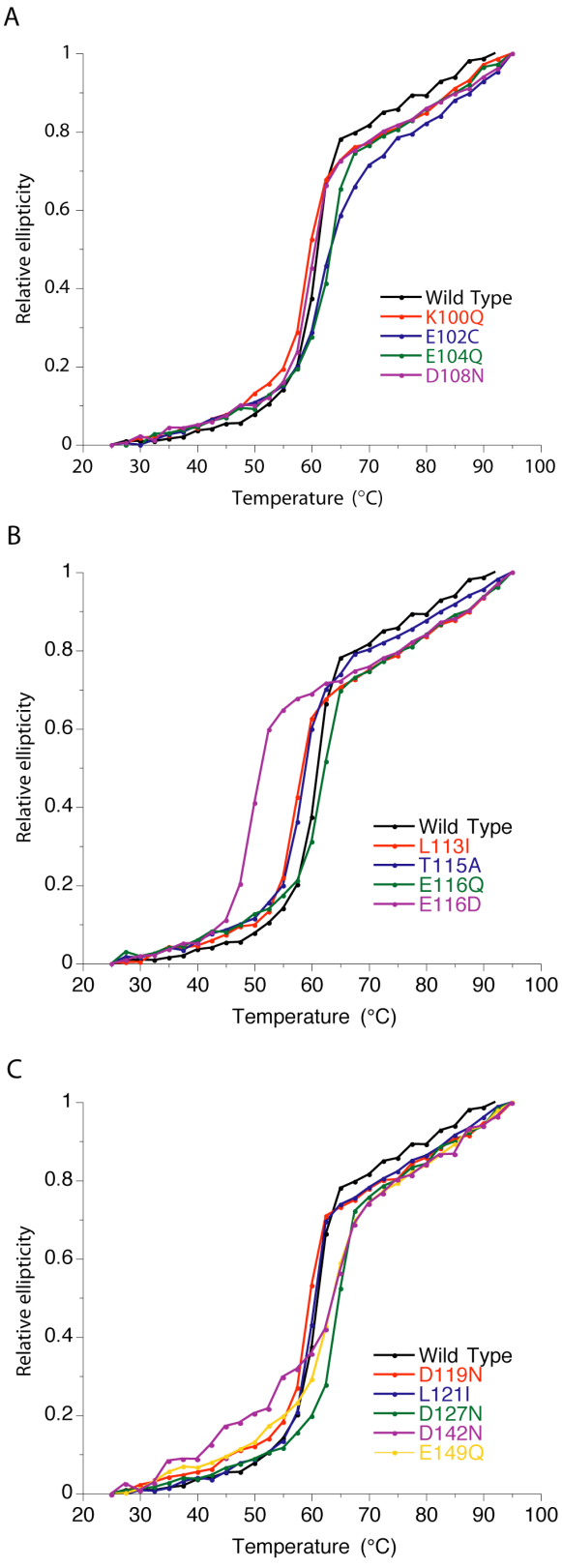

Figure 3.6: Circular dichroism thermal denaturation curves for wild-type Tb-MscL and a series of single-site C-terminal mutations. A) Mutations in the upper portion of the crystal structure C-terminal region. B) Mutations in the lower portion of the crystal structure C-terminal region. C) Mutations to residues not in the crystal structure.

Additionally, since there is no apparent effect of mutating the glutamic acid at position 116 to the corresponding amide, it seems that residue 116 either has a shifted pKa and is neutral at pH 7.2 or that the negative charge is not important at this position.

Other mutations showed an *increased* stability upon charge neutralization. The T_m shifted to a moderately higher temperature for D127N, and to slightly higher temperatures for E102C, E104Q, D142N, and E149Q. These results agree generally with the computational prediction that neutralizing negatively charged residues would lead to an overall stabilization in the region. In addition, these residues likely do *not* experience a significant pKa shift in the assembled channel structure, since neutralizing them has a distinct effect on channel stability.

Two mutations to uncharged residues, L113I and T115A, also showed an effect on structural stability, slightly decreasing T_m. L113I lies on the helical face discussed below that might line the inside of the helical bundle in the physiological structure. Thus, this site may be sensitive to mutation because of important steric contacts made by the leucine side chain. However, the effect observed for T115A is difficult to explain without further experimentation.

Developing Structural Models of the MscL C-terminal Region

Previous modeling has proposed a generally helical structure for the carboxyl terminus of many MscL homologues, including coiled coil regions for some species (Hamill and Martinac, 2001; Sukharev et al., 2001). As well, TASP studies have implied that the assembled Tb-MscL carboxyl terminal region is highly helical (Kochendoerfer et al., 2002). The experimental structural stability data in this chapter are consistent with

the C-terminal region having an extended α-helical secondary structure, since when the thermal melt data is mapped on a helical wheel, all of the mutations that led to altered structural stability reside on one face of the helix, except for E104Q and T115A (Fig. 3.7). This type of extended C-terminal helix structure would be reminiscent of the KcsA C-terminal structure determined by EPR (Cortes et al., 2001).

It is interesting to note that a stabilizing effect was not observed for D108N, although computations implied that charge neutralization at that site would significantly affect the stability of the region. This could mean that the D108 are in close proximity and undergo a pKa shift in the assembled structure. If this is true, then a mutation that decreases the steric bulk at site 108, such as D108A, might affect structural stability, analogous to how E116D showed a significant shift in T_m. However, it seems more likely that under physiological conditions that the C-terminal helical bundle might rearrange slightly, such that the helical face containing the mutants that alter stability line the inside of the bundle instead of the face containing E104 and D108, which lines the inside in the crystal structure. This would be consistent with E116 forming an important steric contact between helices and with the lack of effect seen for the D119N mutant, which lies on the same face as residues 104 and 108. A similar rearrangement of the helical bundle was also proposed by Sukharev and co-workers, although their proposed rotation is slightly different, placing the helical face between L114 and L120 at the inside of the bundle (Anishkin et al., 2003).

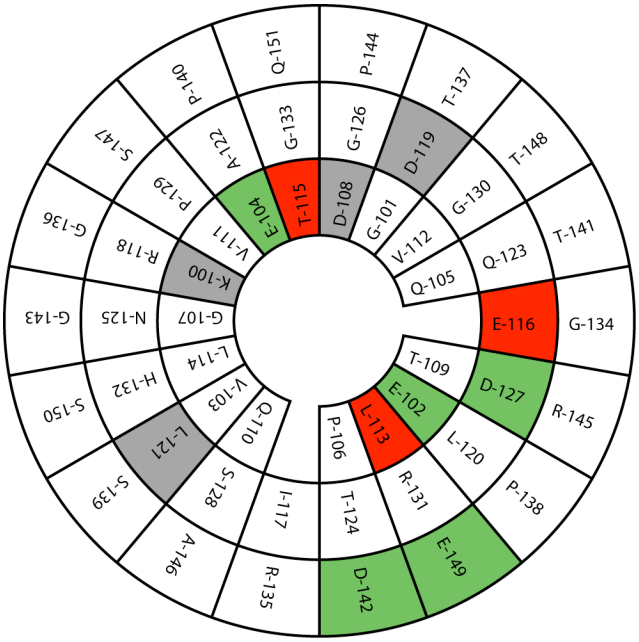

Figure 3.7: Helical wheel showing observed shifts in thermal stability for mutations in the carboxyl terminal region of Tb-MscL. Gray coloring indicates no shift, green indicates a shift to a higher T_m (a stabilizing mutant), and red indicates a shift to a lower T_m (a destabilizing mutant).

Although the helical rotations described above explain the stability data in a fairly straightforward manner, other structural models could be proposed. For example, it is also possible that instead of forming one long extended helix that the region contains a bend causing the most distal region to interact with the region visible in the crystal structure. A cartoon of this sort of structure is shown in Fig. 3.8. The high density of proline and glycine residues between sites 116 and 142 (32% of residues) could allow for this bend to occur, allowing interactions between regions separated in sequence space. Future work on the structural and functional affects of these and other mutations in the region may be able to support this model, the extended helix model, or another structural motif for the region.

Figure 3.8: A cartoon depicting one possible conformation of a Tb-MscL single subunit with a "bend" in the C-terminal region. The residues in the crystal structure are shown in blue and the C-terminus, which could not be resolved in the crystal structure, is shown in red.

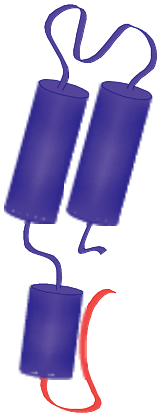

Summary

Calculations involving only the intracellular C-terminal region of Tb-MscL were used to investigate the effect of different side chain protonation states on the stability of the C-terminal helix bundle. Conservation of the crystal structure conformation was greatly increased by neutralizing the acidic Asp and Glu residues in this region, which would occur under low pH conditions such as those used for crystallization. This increased stability at low pH may have aided in the crystallization of the channel. Several computational mutations to this region were made in attempts to replicate the effects of low pH under physiological pH conditions. Although single mutations did not have much effect on the region, an E104Q/D108N double mutant afforded a helix bundle conformation equivalent to that of the low pH model.

One limitation of these simulations is that they do not include any interactions that might occur between the C-terminus and the lipid. If lipid interactions play a significant role in stabilizing—or destabilizing—the C-terminal region, then considering these interactions more explicitly in other simulations could lead to more detailed insights

into the structure of this region. In fact, subsequent simulations of the full channel structure embedded in the lipid membrane described in Chapter 5 have pointed to a significant role for lipid stabilization in this region.

Although the experimental data has begun to give us some insight into the effect of mutations in the Tb-MscL C-terminus on the stability of the channel, many questions remain. Most importantly, it is still unknown whether or not most of these mutations affect channel function. One of the mutants, E104Q, has been electrophysiologically characterized as a gain-of-function mutation, requiring much less membrane tension to open than wild-type Tb-MscL (Shapovalov et al., 2003). This mutation was also observed to stabilize the structure of the channel in thermal denaturation studies. It will be interesting to investigate whether similar physiological effects will be observed for the other mutations that altered structural stability. In addition, functional characterization will give interesting insight into the intriguing pair of mutations to E116.

References

Anishkin, A., V. Gendel, N. A. Sharifi, C. S. Chiang, L. Shirinian, H. R. Guy, and S. Sukharev. 2003. On the conformation of the COOH-terminal domain of the large mechanosensitive channel MscL. *J. Gen. Physiol.* 121:227-44.

Berendsen, H. J. C., J. P. M. Postma, W. F. van Gunsteren, A. DiNola, and J. R. Haak. 1984. Molecular dynamics with coupling to an external bath. *J. Chem. Phys.* 81:3684-3690.

Berendsen, H. J. C., D. van der Spoel, and R. van Drunen. 1995. GROMACS: A message-passing parallel molecular dynamics implementation. *Comp. Phys. Comm.* 91:43-56.

Chang, G., R. H. Spencer, A. T. Lee, M. T. Barclay, and D. C. Rees. 1998. Structure of the MscL homolog from *Mycobacterium tuberculosis*: a gated mechanosensitive ion channel. *Science* 282:2220-6.

Cortes, D. M., L. G. Cuello, and E. Perozo. 2001. Molecular architecture of full-length KcsA: role of cytoplasmic domains in ion permeation and activation gating. *J Gen Physiol* 117:165-80.

Hamill, O. P., and B. Martinac. 2001. Molecular basis of mechanotransduction in living cells. *Physiological Reviews* 81:685-740.

Hess, B., H. Bekker, H. J. C. Berendsen, and J. G. E. M. Fraaije. 1997. LINCS: A linear constraint solver for molecular simulations. *J. Comp. Chem.* 18:1463-1472.

Kabsch, W., and C. Sander. 1983. Dictionary of protein secondary structure—Pattern-recognition of hydrogen-bonded and geometrical features. *Biopolymers* 22:2577-2637.

Kochendoerfer, G. G., J. M. Tack, and S. Cressman. 2002. Total chemical synthesis of a 27 kDa TASP protein derived from the MscL ion channel of *M. tuberculosis* by ketoxime-forming ligation. *Bioconjugate Chemistry* 13:474-480.

Maurer, J. A., D. E. Elmore, H. A. Lester, and D. A. Dougherty. 2000. Comparing and contrasting *Escherichia coli* and *Mycobacterium tuberculosis* mechanosensitive channels (MscL) - New gain of function mutations in the loop region. *Journal of Biological Chemistry* 275:22238-22244.

Miyamoto, S., and P. A. Kollman. 1992. SETTLE: An analytical version of the SHAKE and RATTLE algorithms for rigid water models. *J. Comp. Chem.* 13:952-962.

Shapovalov, G., R. Bass, D. C. Rees, and H. A. Lester. 2003. Open-state disulfide cross-linking between *Mycobacterium tuberculosis* mechanosensitive channel subunits. *Biophys J* 84:2357-65.

Spencer, R. H., G. Chang, and D. C. Rees. 1999. "Feeling the pressure": Structural insights into a gated mechanosensitive channel. *Curr. Opin. Struct. Biol.* 9:448-454.

Sukharev, S., S. R. Durell, and H. R. Guy. 2001. Structural models of the MscL gating mechanism. *Biophys. J.* 81:917-936.

Chapter 4: Initial Molecular Dynamics Simulations of *M. tuberculosis* MscL Embedded in an Explicit Lipid Membrane

Background

Mechanosensitive channels, which gate in response to the application of tension to a phospholipid membrane, are implicated in a wide range of biological processes, such as touch, hearing, and circulation (Hamill and McBride, 1995). Despite this importance in multiple contexts, the mechanism(s) by which channel proteins can "sense" membrane tension and the structural changes associated with gating are not well understood. A more complete understanding of mechanosensitive signal transduction processes is increasingly desirable with the cloning of vertebrate mechanosensitive channels, such as the vanilloid receptor-related osmotically activated channel (VR-OAC) (Liedtke et al., 2000). Recently, the 3.5 Å resolution crystal structure (Fig. 4.1*A*) of the *M. tuberculosis* homologue of the bacterial mechanosensitive channel of large conductance (Tb-MscL) was reported by Rees and co-workers (Chang et al., 1998). This structure provides a unique opportunity to consider the structure-function relationships of a mechanosensitive channel on an atomic level. MscL, which is thought to protect bacterial cells from severe osmotic downshock (Levina et al., 1999; Nakamaru et al., 1999; Wood, 1999), is the best characterized mechanosensitive ion channel. The *E. coli* homologue (Eco-MscL) was the first to be cloned (Sukharev et al., 1994) and has received the most attention (Batiza et al., 1999; Blount and Moe, 1999; Oakley et al., 1999; Spencer et al., 1999; Sukharev, 1999; Sukharev et al., 1997). One focus of these studies has been the determination of single site mutations that affect gating properties. In particular, several "gain of function" (GOF) mutations have been characterized in which lower tension is needed to gate the channel (Blount et al., 1997; Blount et al., 1996b; Ou et al., 1998; Yoshimura et al., 1999). Recently, Tb-MscL has been subjected to more limited structure-function

studies, a major goal of which has been to determine the extent to which the extensive studies on Eco-MscL can be translated to Tb-MscL (Maurer et al., 2000; Moe et al., 2000).

This chapter discusses molecular dynamics (MD) simulations utilizing the Tb-MscL crystal structure to help develop structure-based explanations of these experimental observations about the channel. Since the early simulations of lipid bilayer systems (Egberts and Berendsen, 1988), MD calculations of proteins with explicit lipid and solvent molecules have become increasingly common. Many of these simulations have been reviewed recently (Forrest and Sansom, 2000; Roux, 2002). Some work has focused on MD simulations of ion channels, considering small channels such as gramicidin A (Chiu et al., 1999a; Chiu et al., 1999b; Tang et al., 1999; Woolf and Roux, 1996) or ion channel models often consisting of TM helix bundles (Capener et al., 2000; Fischer et al., 2000; Forrest et al., 2000; Husslein et al., 1998; Law et al., 2000; Lin and Baumgaertner, 2000; Randa et al., 1999; Schweighofer and Pohorille, 2000; Tieleman et al., 1999a; Tieleman et al., 1998a). The determination of crystal structures for KcsA and

Figure 4.1 (On next page): (*A*) Tb-MscL crystal structure with the five subunits shown in different colors. The intersubunit H-bond between Arg 45 and Gln 51 residues in adjacent subunits and the point (Asp 108) where the structure is cleaved for embedded simulations are highlighted. (*B*) The embedded wild-type Tb-MscL simulation system after 100 ps of MD simulation, before restraints were gradually removed from protein Cα atoms. The system included 495 protein residues, 290 POPE molecules, and 17851 SPC water molecules for a total of 73313 atoms. The protein is shown in white CPK with charged residues (Lys, Arg, Asp, Glu) highlighted in red. The lipid and water are shown in green and blue wireframe, respectively, with lipid phosphorous atoms in yellow CPK. (*C*) A single subunit of the Tb-MscL crystal structure with the regions used for embedded MD analyses shown in different colors. In addition, the two residues altered by computational mutations in embedded MD simulations, Val 21 and Gln 51, are shown in CPK.

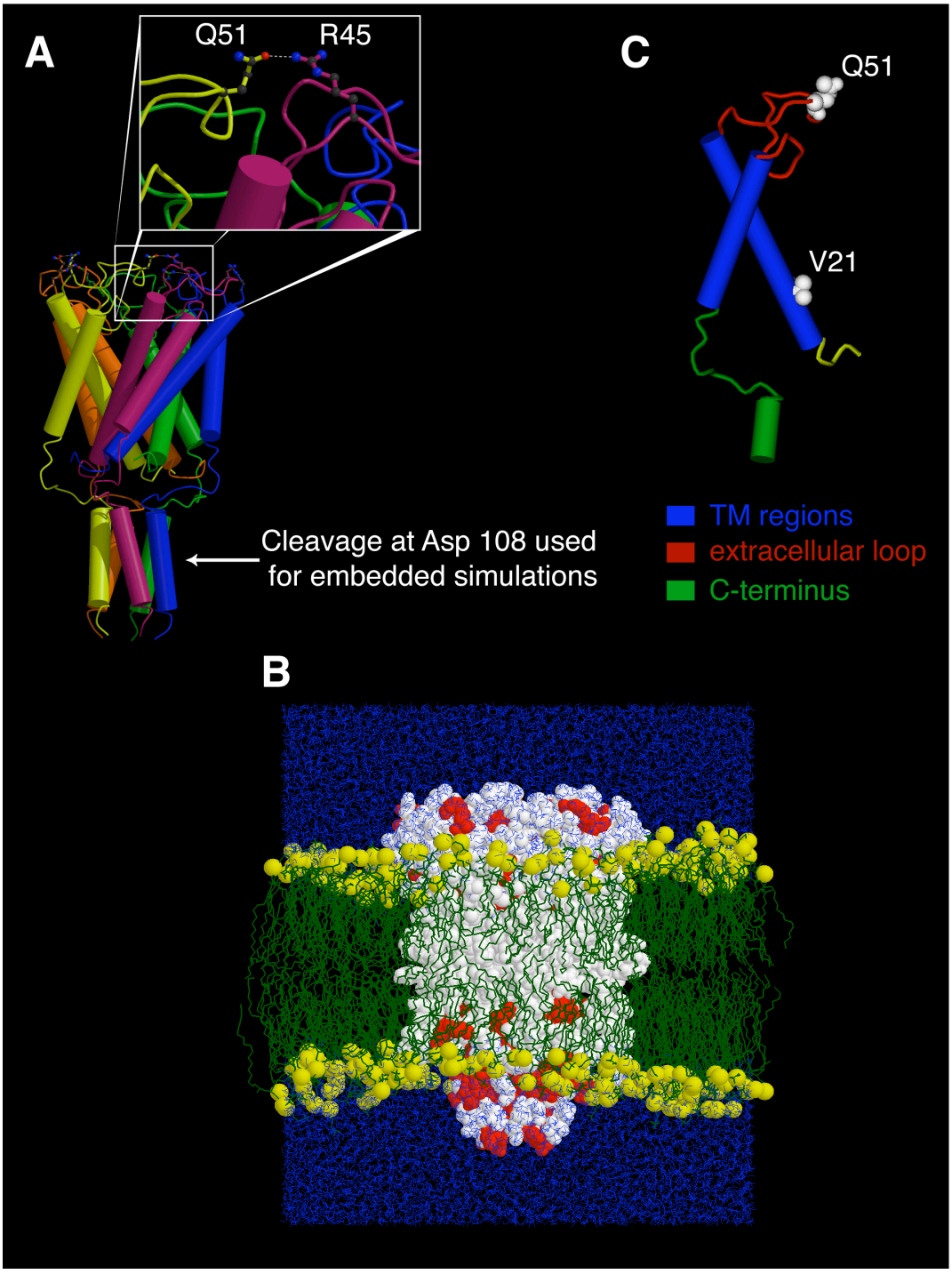
A
Q51
R45
Cleavage at Asp 108 used
for embedded simulations
C
Q51
V21
TM regions
extracellular loop
C-terminus
B

OmpF also allowed simulations of more complete channels in both explicit lipid (Bernèche and Roux, 2000; Shrivastava and Sansom, 2000; Tieleman and Berendsen, 1998) and lipid-mimetic environments such as octane (Guidoni et al., 1999; Guidoni et al., 2000). These MD studies described the dynamics and conformations of protein structures, the movements and orientations of water and lipid molecules, and interactions between protein, lipid, and water throughout the simulations. Unlike the crystal structures of KcsA and OmpF, the Tb-MscL channel has a domain that extends significantly outside the membrane. Roughly 15-20 C-terminal residues of each subunit in the crystal structure are intracellular, forming the helical bundle discussed above. This complicates the simulation, in that a much more extensive water layer must be present on the intracellular side.

The simulations discussed in this chapter include one wild-type and two mutant (V21A and Q51E) trajectories of Tb-MscL embedded in an explicit palmitoyloleoyl-phosphatidylethanolamine (POPE) membrane, totaling over 4 ns in length (Berrier et al., 1989; Blount et al., 1996a; Lee et al., 1996). Previous work has indicated that both mechanosensitive responses in general (Berrier et al., 1989) and MscL in particular (Blount et al., 1996a; Häse et al., 1997) are associated with the inner membrane in *E. coli*. In the *M. tuberculosis* inner membrane, phosphatidylethanolamine (PE) lipids are more prevalent than other lipids for which parameters are readily available, such as phosphatidylcholine (PC) (Lee et al., 1996). POPE lipid was also used in a previous simulation of the *E. coli* OmpF porin (Tieleman and Berendsen, 1998). Although some recent simulations have begun to consider heterogeneous membranes, such as lipid/steroid (Pasenkiewicz-Gierula et al., 2000; Smondyrev and Berkowitz, 1999;

Smondyrev and Berkowitz, 2000; Tu et al., 1998) or two lipid mixtures (Murzyn and Pasenkiewicz-Gierula, 1999), simulations of embedded proteins have thus far included only single lipids.

The present simulations provide insights into the general dynamics of the wild-type Tb-MscL channel and differences in the V21A and Q51E mutant channel dynamics potentially related to their experimental phenotypes. Other analyses of the trajectories point to protein-lipid interactions that may increase our understanding of tension transduction between lipid and protein.

Computational Methods

The Tb-MscL crystal structure (1MSL) solved by Chang et al. was used as a starting structure for all MscL simulations (1998). Previous experimental work on Eco-MscL has shown that C-terminal cleavage at Ala 110 or later has no significant effect on channel function (Blount et al., 1996b). Thus, all simulations in this chapter used Tb-MscL with a similar cleavage after Asp 108, based on sequence alignment to Eco-MscL, to reduce system size. The nine residues missing from the crystal structure N-terminus were not included as their conformation is unknown. Uncharged N- and C-termini were used. All potentially ionizable residues (no His are present in Tb-MscL) were charged, as they generally were exposed to the pore water or to bulk solvent after embedding in the membrane.

An equilibrated hydrated membrane of 340 POPE lipid molecules and 6728 SPC waters similar to that used for simulations of OmpF was obtained from D. P. Tieleman (Tieleman and Berendsen, 1998). Throughout, the membrane will be oriented in the XY

plane with the Z-axis as the membrane normal. This membrane was equilibrated further for 500 ps of NPT simulation at 310 K before embedding Tb-MscL. Embedding of Tb-MscL was performed by superimposing the channel structure onto the lipid and removing a minimal number of lipids (50) that were in the pore region or had extensive overlap with MscL. Although the exact decision about what lipids overlapped "too much" with the channel was somewhat arbitrary, a few guidelines were followed. First, lipids that had atoms extremely close (i.e. < 1-2 Å) to the channel were removed. After the most clearly overlapping lipids were removed, the system was tested by minimizing it and seeing if it could be used to start a MD run (using the parameters discussed below). If enough lipids had not been removed, overlaps between lipid and protein would lead to system "blowup," which typically causes a fatal breakdown in the ability of LINCS to constrain bond lengths. When such a "blowup" occurred, the lipids causing the "blowup" were removed and the system was tested again, repeating this process until a useable system was obtained.

The optimal positioning of the channel in the Z-direction also was somewhat ambiguous; patterns of charged, polar, and aromatic residues were used to estimate the proper position. As seen in Fig. 4.1*B*, this approach placed almost all charged residues outside of the membrane region. Other concurrent simulations in which the transmembrane (TM) helices of Tb-MscL were embedded at different membrane positions (Philipson, Elmore, and Dougherty, unpublished data) were also used for guidance. These simulations included residues Ala 10-Asn 44 for TM1 and Thr 66-Leu 97 for TM2, along with 166 lipids and 4742 SPC water molecules. In these simulations, three positions along the Z-axis were chosen for the TM bundle: the same one used in

the full channel simulations, one with the channel moved 3 Å towards the intracellular side of the membrane, and one with the channel moved 8 Å towards the intracellular side. In all three simulations, the bundle remained generally intact, showing that the system was fairly tolerant of different positions. This agrees with the observation discussed below that protein-lipid interactions during the trajectory appear to adjust to initial channel placement. Although no experimental data on the position of the channel in the membrane had been obtained when these simulations were performed, after their original publication EPR measurements on spin-labeled MscL confirmed that the positioning used was reasonable (Perozo et al., 2001).

After the membrane embedding procedure, this system was then solvated fully, including inside the pore, with SPC waters (Berendsen et al., 1981), which have been shown to reproduce experimental properties well in membrane simulations (Tieleman and Berendsen, 1996). Sufficiently large layers of water were placed above and below the membrane to prevent the intracellular and extracellular Tb-MscL domains from being within the electrostatic cutoff of one another through the box edges. This total system, which was initially about 9.6 nm x 9.5 nm x 10.5 nm, included 495 protein residues, 290 POPE, and 17851 SPC waters for a total of 73313 atoms, and is shown in Fig. 4.1*B*. This initial system was used to begin the wild-type and Q51E simulations.

The wild-type simulation began with 150 steps of steepest descents minimization on the embedded structure to reduce close contacts. The system was then heated to 310 K over 20 ps with restraints on all Cα atoms of the protein; after heating all simulations were run at 310 K. Restraints were used for an additional 80 ps of

simulation, and were then released in gradual steps over the subsequent 165 ps. This was followed by 1335 ps of simulation without restraints, for a total trajectory of 1500 ps.

The Q51E mutation was made to the embedded structure by deleting the two amide protons of the Glu 51 side chains and changing their amide N atoms to unprotonated acidic O atoms. These changes were made for all five subunits of the channel. The Q51E mutation also required the addition of five sodium cations to neutralize the overall charge of the system box. The simulation followed the same protocol as the wild type, except that 50 steps of minimization were before and 100 steps were after the addition of Na^+.

The V21A mutant trajectory began with the 700 ps structure from the wild-type trajectory. The V21A mutation was made by deleting the two Val 21 Cγ methyl groups and converting the Cβ to a methyl group for all five subunits. This mutated structure was then run at 310 K without restraints for 1100 ps. A schematic of the embedded simulations performed can be seen in Fig. 4.2.

Figure 4.2: Schematic of the embedded Tb-MscL MD trajectories reported in this chapter.

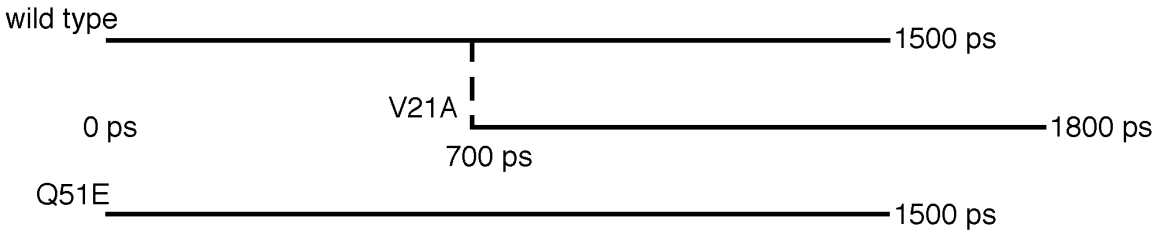

All minimizations and MD simulations were performed using GROMACS 2.0 (Berendsen et al., 1995). Standard GROMACS parameters were used. The MD protocol used for the membrane embedded simulations in this study followed those applied successfully for previous embedded full channel structure systems (Bernèche and Roux, 2000; Shrivastava and Sansom, 2000; Tieleman and Berendsen, 1998). Lipid parameters were taken from previous work by Berger et al., with extra parameters for the oleoyl double bond taken from the GROMOS force field (Berger et al., 1997). All MD runs used a timestep of 2 fs along with the LINCS routine to constrain bond lengths (Hess et al., 1997) and SETTLE to constrain water geometries (Miyamoto and Kollman, 1992). The NPT ensemble with periodic boundary conditions was employed for all runs with pressure coupled anisotropically to 1 bar individually in each of the three directions with a coupling constant (τ_p) of 1.0 ps (Berendsen et al., 1984). This ensemble should allow the embedded system to adjust its surface area appropriately after the embedding procedure. System temperatures were coupled separately for protein, lipid, solvent, and ions to a temperature bath with a coupling constant (τ) of 0.1 ps (Berendsen et al., 1984). A twin-range cutoff was used for determining non-bonded interactions: 1.0 nm for Lennard-Jones and short-range Coulombic and 1.8 nm for long-range Coulombic interactions. Although there are some advantages to using Ewald sum methods to calculate long-range electrostatics in lipid membrane systems (Feller et al., 1996), the cutoff method employed here is less computationally expensive and has been used previously in embedded channel systems using these lipid parameters (Capener et al., 2000; Fischer et al., 2000; Forrest et al., 2000; Randa et al., 1999; Shrivastava and Sansom, 2000; Tieleman and Berendsen, 1998; Tieleman et al., 1999a; Tieleman et al.,

1998a). Differences resulting from using Ewald sum methods for MscL MD simulations are discussed in Chapter 5.

Analyses of the trajectories were primarily performed with tools included in the GROMACS suite (Berendsen et al., 1995). Properties were averaged over the last 1000 ps of trajectories unless otherwise noted. Additionally, the DSSP program was used to determine secondary structure (Kabsch and Sander, 1983) and the HOLE program was used to calculate pore diameter profiles (Smart et al., 1997). Channel regions used for analyses were: TM1 (15-43), extracellular loop (44-69), TM2 (69-89), and C-terminal region (90-108), analogous to those defined in previous sequence analyses and highlighted in Fig. 4.1*C* (Maurer et al., 2000). Hydrogen bond and salt bridge interactions are defined geometrically as interactions in which the distance between the hydrogen and acceptor atoms is less than 0.25 nm and the interaction angle is less than or equal to 60°. Amide N atoms were omitted as possible H-bond acceptors. Some figures were made using MOLSCRIPT (Kraulis, 1991) or RasMol (Sayle and Milner-White, 1995).

Protein Stucture in the Wild-Type MscL Simulation

The average MD structure from the final 1 ns of the embedded wild-type Tb-MscL trajectory was generally close to that of the crystal structure, as can be seen by visual inspection (Fig. 4.3). This relative conservation of the crystal structure conformation with all side chains ionized suggests that neutral (low pH) residue ionization states would not alter the trajectory as drastically as in the C-terminal bundle simulations discussed in Chapter 3. In particular, the TM domain structure remained

very similar to the crystal structure. However, a greater structural difference is seen in the extracellular loop and C-terminal regions. These trends of structural conservation are also apparent in the computed Cα RMS deviation after fitting to the crystal structure over the trajectory. The RMS was calculated both for all Cα and for Cα in specific regions of the protein (Fig. 4.4). The overall Cα RMS of about 0.33 nm is somewhat higher than that of previous channel simulations, which generally have reported values of 0.18-0.25 nm (Bernèche and Roux, 2000; Shrivastava and Sansom, 2000; Tieleman and Berendsen, 1998). However, the RMS deviation of the MscL TM helices ($\approx$ 0.17 nm) is quite comparable to previous simulations of both KcsA and OmpF, both of which have much less extensive extramembrane regions. As well, the RMS deviation for Tb-MscL TM

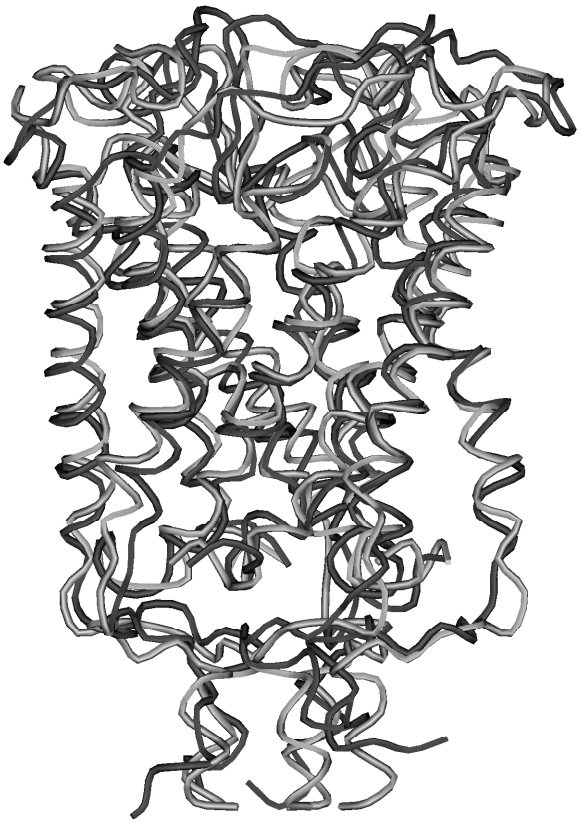

Figure 4.3: Superimposed Cα traces for the Tb-MscL crystal structure (light gray) and the average structure for the final 1000 ps of the wild-type simulation (dark gray). The crystal structure is cleaved at Asp 108 as was done in the simulated channel.

domains was similar to those seen for stable TM bundle calculations (Capener et al., 2000; Fischer et al., 2000; Forrest et al., 2000; Husslein et al., 1998; Law et al., 2000; Lin and Baumgaertner, 2000; Randa et al., 1999; Schweighofer and Pohorille, 2000; Tieleman et al., 1999a; Tieleman et al., 1998a). It is not particularly surprising that an increased deviation from the crystal structure was seen in the extracellular loop and C-terminal regions, as those regions had greater uncertainty in the crystal structure. In addition, repulsions between acidic residues in their negatively charged physiological protonation states caused large structural deformations in the C-terminal simulations discussed in Chapter 3. The computationally imposed cleavage at Asp 108 in the C-terminal region may also impact the RMS deviation in that region.

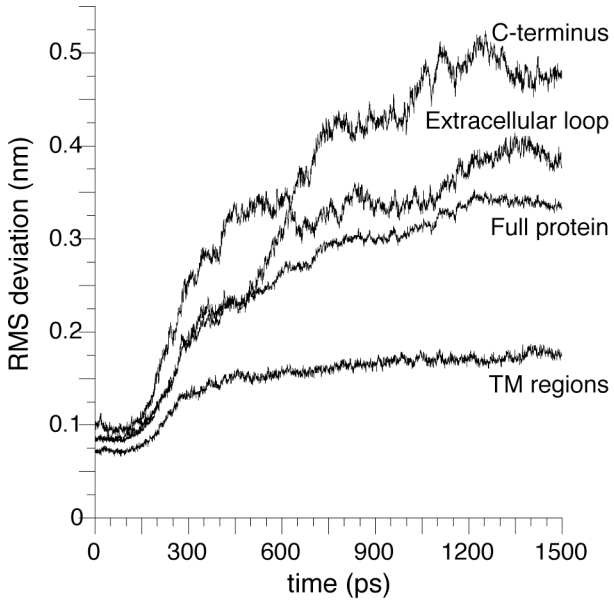

Figure 4.4: RMS deviation of Cα from the crystal structure for the wild-type Tb-MscL trajectory. RMS values were determined both for the full protein and for selected regions, and were calculated for each frame after fitting the Cα for the region under consideration to the crystal structure.

The Tb-MscL extramembrane regions are also more conformationally flexible than the TM domains, as can be seen by the substantially larger Cα RMS fluctuations in

these regions (Fig. 4.5). The increased fluctuation is in agreement with the increased temperature factors for those regions in the crystal structure (Chang et al., 1998). Increases in fluctuation, although smaller in magnitude, were also seen for loop regions in the OmpF simulation (Tieleman and Berendsen, 1998).

The relative structural stability of the ten TM helices is also apparent in their conservation of α-helical structure throughout the simulation, as measured with DSSP (data not shown). As well, no other regions of consistent secondary structure, such as 3$_{10}$-helices or β-sheets, arise during the simulation.

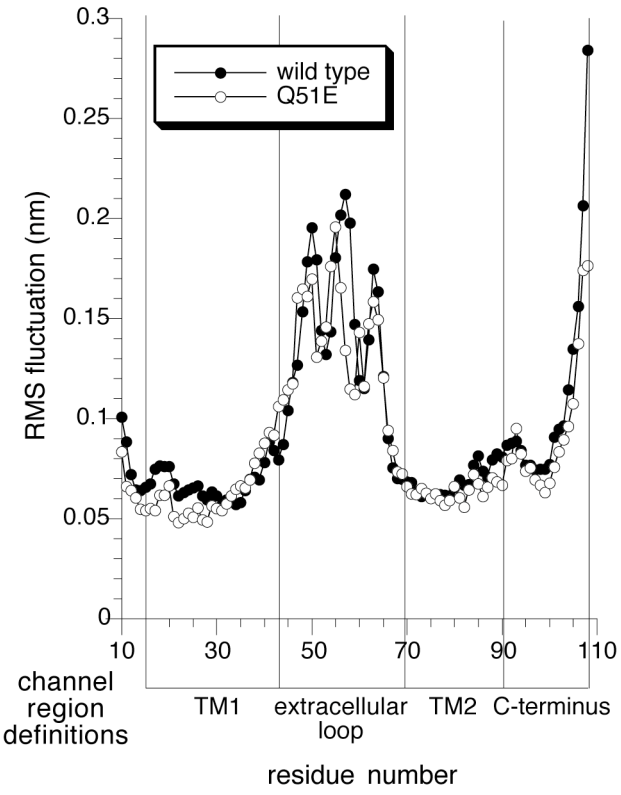

Figure 4.5: RMS fluctuation of Cα around an average structure for the wild-type and Q51E trajectories plotted per residue. Fluctuations for the V21A mutant trajectory were very similar, and are omitted for clarity. The computed RMS fluctuation is averaged over the five chains.

Structural Changes in Mutant Trajectories

The wild-type, V21A and Q51E trajectories display similar Cα RMS deviations from the crystal structure (data not shown), and all three show similar Cα RMS fluctuations (Fig. 4.5). The Cα RMS deviations from the crystal structure for the TM, extracellular loop and C-terminal regions of the mutants likewise were very similar to those for the wild type. As well, secondary structures throughout the mutant trajectories were similar to those in wild type, with the ten TM helices well preserved (data not shown). Thus, neither of the mutant trajectories showed a significantly larger difference from the crystal structure than wild-type. As well, the equilibrium structures from all 3 trajectories were at least as similar to each as other as they were to the crystal structure (data not shown).

While no significant global change in structure is seen for either mutant, the V21A mutant does display an increased pore radius in the general region around residue 21 (Fig. 4.6). Some increase was expected given the reduction in steric size of this putative plug residue from Val to Ala. This increase from steric reduction can be seen by comparing the radii of the 700 ps wild-type frame (the frame from which the V21A trajectory was begun) with and without the mutation. However, as the V21A trajectory equilibrates, the observed pore widening extends through a longer section of the channel than seen for the initial change from Val to Ala. It has been postulated that a V21A mutation may decrease the van der Waals interactions among pore lining TM1 helices, weakening a "hydrophobic lock" that stabilizes the channel closed state (Moe et al., 2000; Yoshimura et al., 1999). The simulations support this view in that there is a widening of the pore, perhaps indicative of weakened helix-helix interactions, across a

significant section of the channel. Note, however, that there is no evidence for an increased structural instability of the TM1 region in either comparisons of Cα RMS fluctuations for wild-type and V21A simulations (Fig. 4.5) or conservation of α-helical secondary structure measured by DSSP (data not shown).

Figure 4.6: Pore radius profiles for the wild-type and V21A Tb-MscL simulations in the membrane region calculated with the HOLE program. Each profile given is the average of profiles taken every 100 ps over the final 500 ps of the simulations. The calculated pore radius of the initial V21A mutation frame (the 700 ps wild-type frame with the V21A mutation) is also shown to show the change in pore radius resulting from the Val to Ala steric change before equilibration of the mutant structure. Numbering on the Z-axis begins with the intracellular side of the simulation box at 0 nm. The average position of the "plug" residue 21 is denoted.

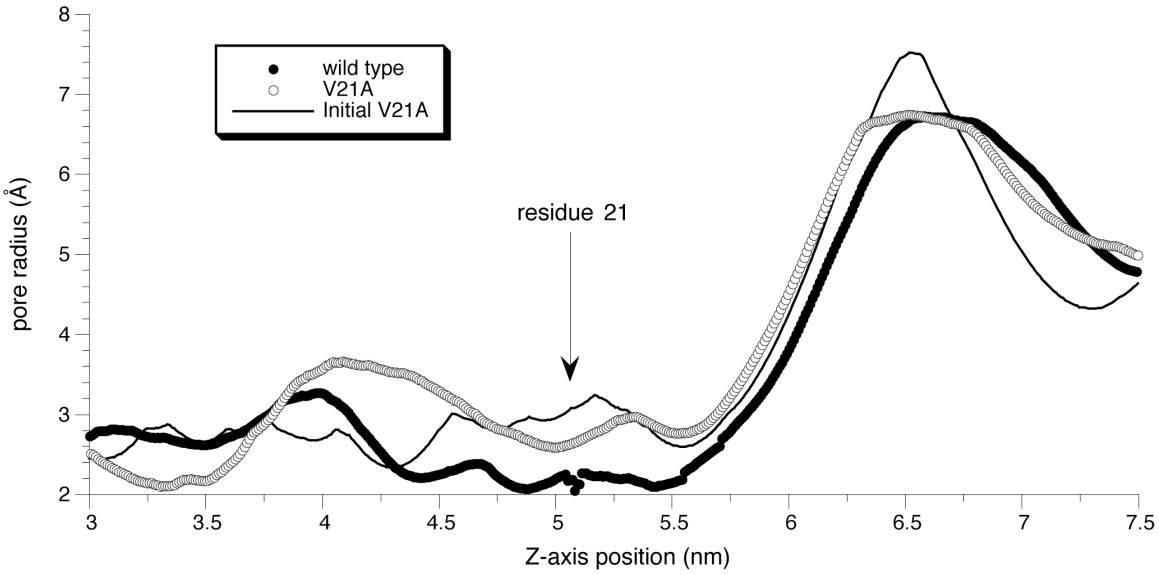

The R45-Q51 Hydrogen Bonding Interaction

An intersubunit hydrogen bond is apparent between the R45 and Q51 side chains in adjacent extracellular loop regions of the Tb-MscL crystal structure. The actual proximity of these residues has been verified through designed cross-linking reactions,

and this proximity hints at a possible physiological role of this interaction (Maurer et al., 2000). In order to better understand the effect of this mutation, the presence of hydrogen bonding (or in the case of Q51E, salt bridge formation) between these residues in the trajectories was considered.

The populations of the five possible intersubunit interactions between residues 45 and 51 show very different patterns in the wild-type and Q51E Tb-MscL trajectories (Fig. 4.7). In the wild-type trajectory after approximately 250 ps, a maximum of 2 of the possible 5 hydrogen bonds are usually formed at any one time. Two of the residue pairs (pairs 3 and 4) drift apart after that first portion, and another (pair 1) is very rarely formed as the simulation continues. As well, one of the pairs that shows a reasonable interaction is fairly flickery (pair 5). Notably, one of the pairs that drifted apart early in the simulation (pair 3) does form a few isolated interactions later in the trajectory, showing that interactions are not prevented because of some major deformation in the loop structure. Similar trends of hydrogen bond occupancy are seen for the V21A mutant (data not shown).

In contrast, all five possible salt bridges are formed early in the Q51E trajectory (Fig. 4.7). After that point, two of the interactions essentially break (pairs 2 and 3); two are almost always formed (pairs 4 and 5); and one other fluctuates (pair 1). The net result is that the 45•••51 intersubunit interaction is significantly more prevalent in the Q51E mutant than in the wild type. This is confirmed by the fact that the dwell time of salt bridges in the Q51E trajectory is considerably longer than that of the hydrogen bonds in the wild-type trajectory (Fig. 4.7). In other words, when a salt bridge is formed in Q51E, it remains intact longer on the average than a hydrogen bond that is formed in the wild

type. Thus, there is a structural change in the protein that can be associated with the Q51E mutation. There is a definite change in the intersubunit 45•••51 interactions, which may be related to phenotypic changes that may be caused by Q51E mutations.

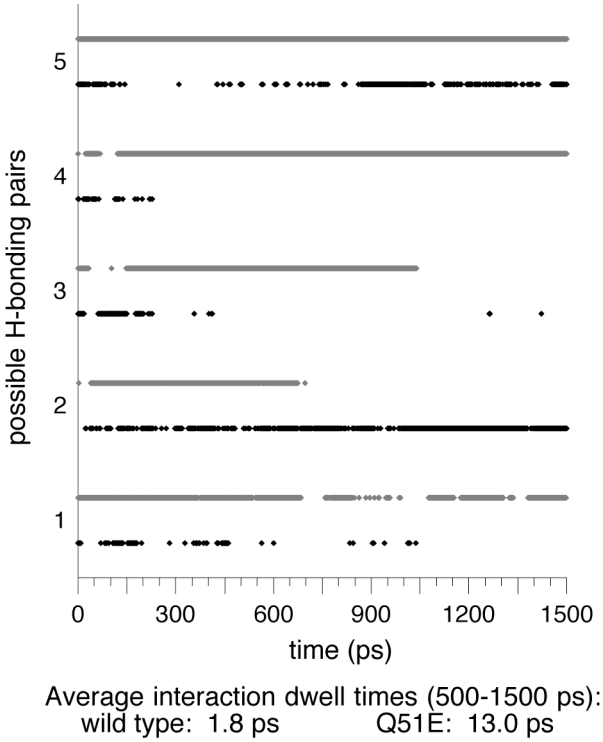

Figure 4.7: Hydrogen bond/salt bridge interaction populations of the five possible R45-Q51 pairs in the wild-type Tb-MscL simulation (black) and of the five possible R45-E51 pairs in the Q51E simulation (gray). The average interaction dwell times were calculated over the final 1000 ps of each simulation.

On a more general note, our results may be considered a bit surprising. We have converted a hydrogen bond between a neutral acceptor (Q51) and a cationic donor (R45) to one between an anionic acceptor (E51) and a cationic donor (R45), a salt bridge. The quantitative contribution of salt bridges to protein stability remains controversial. The 45•••51 interaction is in a region of the protein that is highly exposed to the aqueous medium, (Fig. 4.1*A*) and often a salt bridge is considered to be fairly ineffective in this environment (Dao-pin et al., 1991; Hendsch and Tidor, 1994). Conversely, other studies have shown that charge•••charge side chain interactions are slightly stronger and require

less orientational specificity than charged•••neutral interactions (Scholtz et al., 1993). In this particular system there is the possibility of a double hydrogen bond in the R45•••E51 interaction that is not possible with R45•••Q51, and in fact over 65% of the R45•••E51 interactions include such double interactions.

Protein-Lipid Interactions

MscL is gated by membrane tension, and since purified MscL is fully functional when reconstituted alone into lipid vesicles it is thought that tension is transduced directly from the lipid molecules to the protein (Häse et al., 1995). A more complete description of protein-lipid interactions may give insight into this poorly understood tension transduction process. The total numbers of hydrogen bonds between the lipid and the extracellular loop, C-terminal region, and the whole protein are shown in Fig. 4.8*A*. The total hydrogen bonding between protein and lipid steadily increases over the simulation, reaching a total of about 60 hydrogen bonds by the end of the run. This hydrogen bonding seems extensive, compared to the less than 10 between lipid and hexameric alamethicin channels (Tieleman et al., 1998a), which are known to exhibit some mechanosensitive properties (Opsahl and Webb, 1994). However, the POPC lipid in those simulations had a different headgroup than that used here, and alamethicin is comprised primarily of TM helices that do not cross the headgroup interface as extensively as Tb-MscL. The majority of the Tb-MscL hydrogen bonding occurs with the C-terminal region of the protein, which contains multiple polar and charged residues; relatively few hydrogen bonds were formed between POPE and the extracellular loop region.

Figure 4.8: (*A*) Total number of hydrogen bonds between POPE and protein in the wild-type Tb-MscL simulation. The numbers of hydrogen bonds involving only the extracellular loop or the C-terminal region of the channel are also shown. (*B*) The percentage of hydrogen bonds between POPE and protein that involve PE ammonium groups (-NH_3^+) in the wild-type Tb-MscL trajectory. These percentages are given for both hydrogen bonds to the full protein and for hydrogen bonds in only the extracellular loop or C-terminal regions. (*C*) The percentage of the hydrogen bonds and close contacts (less than 0.25 nm) between POPE and the extracellular loop that involve only the first eight residues of the loop.

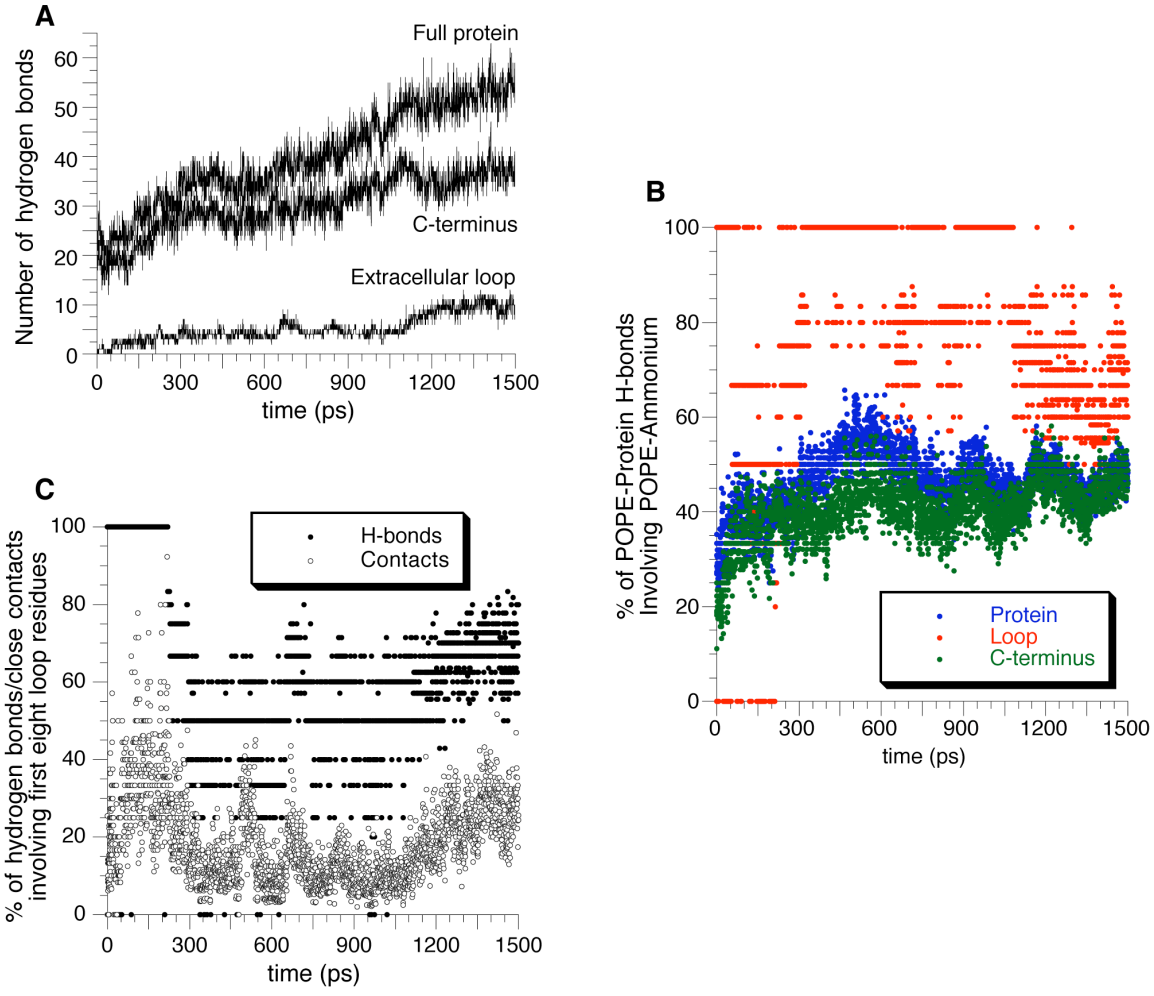

About half of the total protein-lipid hydrogen bonds involve the ammonium (NH_3^+) of the PE headgroup (Fig. 4.8*B*), and the percentage involving the ammonium

group is even higher, around 70%, for the extracellular loop region, although there is considerable variability in this region. Thus, a large proportion of protein-lipid hydrogen bonds include a hydrogen donor from a very small part of the lipid molecules. It is also notable that 73% of the Coulombic interaction between protein and lipid in the wild-type trajectory arises from interactions including the PE ammonium group (Table 4.1). Other common lipid headgroups, such as phosphatidylcholine and phosphatidylglycerol, do not have a hydrogen bond donating group analogous to the PE ammonium and would therefore be expected to show different patterns of hydrogen bonding with embedded Tb-MscL. Such differences in hydrogen bonding interactions could contribute to the differences in Tb-MscL gating tension observed for channels in membranes with different lipid compositions (Moe et al., 2000). Additional simulations using lipids with different headgroups would give further insight into lipid-protein hydrogen bonds and their effect on protein dynamics; some such simulations will be described in the next chapter.

Table 4.1: Average protein-lipid interaction energies (in kcal/mol) over the last 1 ns of the wild-type and Q51E simulations. Energies were computed for protein interactions with different portions of the lipids. Coulombic energies are given in plain font, and Lennard-Jones energies are given in parenthetical italics.

Lipid region	**Wild type**	**Q51E**
PE NH_3 group only	-4346 (*-69*)	-5467 (*-68*)
Entire headgroup	-5990 (*-1836*)	-4960 (*-1742*)
Tails	0 (*-5689*)	0 (*-5827*)

In addition to the alterations in intersubunit hydrogen bonding discussed above, the Q51E mutation also shows altered protein-lipid interactions. The Q51E trajectory showed no notable differences from the wild-type simulation in protein-lipid hydrogen bonding. However, some differences were apparent in average Coulombic interactions between the protein and lipid. Although the negatively charged Glu 51 mutant residues had an increased interaction with the positively charged PE ammonium groups, they showed a reduced electrostatic interaction with the overall headgroup due to unfavorable interactions with the phosphate group (Table 4.1). Simulations utilizing more sophisticated methods, such as PME, for calculating long-range interactions, would be necessary to more fully characterize any electrostatic differences such as these, and the significance of the difference for channel dynamics is unclear in the present simulations. Nonetheless, such changes in protein-lipid interactions could be plausible mechanisms by which loop mutations could lead to altered channel physiology.

The distribution of protein-lipid hydrogen bonds in the extracellular loop region is also notable. Around two-thirds of the hydrogen bonds between POPE and the extracellular loop involve the first 8 residues (44-51), the first third, of the loop (Fig. 4.8*C*). This distribution does not merely reflect an increased number of protein-lipid contacts for these particular loop residues, as only about one-third of the loop-lipid atomic contacts within the hydrogen bonding distance cutoff occur in this section of the loop. The sequence of this portion of the Tb-MscL loop directly after TM1 is quite different from that in other non-Mycobacterial MscL homologues, such as Eco-MscL. Moreover, a group of MscL homologues, including Eco-MscL, which have similar gating tensions in *E. coli* spheroplasts (Moe et al., 1998)—and thus lower gating tensions than

Tb-MscL (Moe et al., 2000)—share a highly conserved region directly after TM1 (Maurer et al., 2000). The lipid hydrogen bonding of Tb-MscL channels mutated to include part or all of this conserved Eco-MscL sequence would be interesting to investigate. Along with the particularly high ratio of hydrogen bonds involving PE ammonium groups in the extracellular loop, the localization of Tb-MscL hydrogen bonds in the loop is particularly interesting in light of experimental results that implicate the loop region in attenuation of the Eco-MscL gating tension (Ajouz et al., 2000).

It should be noted that the positioning of the embedded protein in the membrane could affect protein-lipid interactions observed during these trajectories. However, the increased number of hydrogen bonding interactions during the simulation implies that the interactions represent favorable conformations sampled during the MD run and not just close contacts in the first frames of the simulation. In other words, the channel seems able to adjust its interactions regardless of initial positioning. As noted in previous analyses of protein-lipid hydrogen bonds, increased simulation times would help ensure more complete sampling of relevant side-chain conformations (Forrest et al., 1999). Such extended simulation trajectories may be particularly interesting to consider for this system, as the lipid-protein hydrogen bonding equilibrated fairly slowly, and was perhaps not fully equilibrated in these trajectories. In addition, it would be interesting to consider how applying tension to a system would affect the observed hydrogen bond distributions. These initial analyses highlight intriguing trends in interactions between the Tb-MscL channel and its membrane environment which warrent further investigation.

Particularly strong interactions between Tb-MscL and lipid tails could also occur to aid in tension transduction. Thus, hydrocarbon tail ordering could be different for

lipids bordering the channel and those in the "bulk" lipid. To probe for such ordering in the simulation, the deuterium order parameter (S_{CD}) was calculated for the saturated palmitoyl tails of the lipid. In this analysis, lipids that had at least one atom with an average minimum distance of 0.35 nm from the protein over the last 1 ns of the simulation were considered to be "bordering" the protein; all other lipids were defined as "bulk." This cutoff was set to include all of the closest "shell" of lipids around the channel while omitting a maximal number of lipids outside of this shell (Fig. 4.9*A*). The calculated S_{CD} values show that the channel has some *dis*ordering effect on the bordering lipids relative to bulk (Fig. 4.9*B*). A similar but larger decrease in S_{CD} was also seen for OmpF, a non-mechanosensitive channel, in simulations with a POPE bilayer (Tieleman et al., 1998b). Other helical bundle channel models also have shown analogous trends in computed S_{CD} (Husslein et al., 1998; Tieleman et al., 1998b). As well, there was essentially no difference in the *trans*/*gauche* fraction for tail dihedrals between bordering and bulk lipids. Thus, although the lipid tails are energetically important in channel-lipid interactions (Table 4.1), it appears that Tb-MscL is not causing unusual lipid tail properties.

Figure 4.9: (*A*) Visual depiction of the cutoff between protein "bordering" lipids (dark gray) and "bulk" lipids (light gray). The protein is shown as a ribbon structure. The definition of "bordering" and "bulk" lipids is given in the text, and selects all lipids in the first "shell" around the protein as "bordering." (*B*) Deuterium order parameters (S_{CD}) for protein bordering and bulk lipids in the wild-type Tb-MscL simulation.

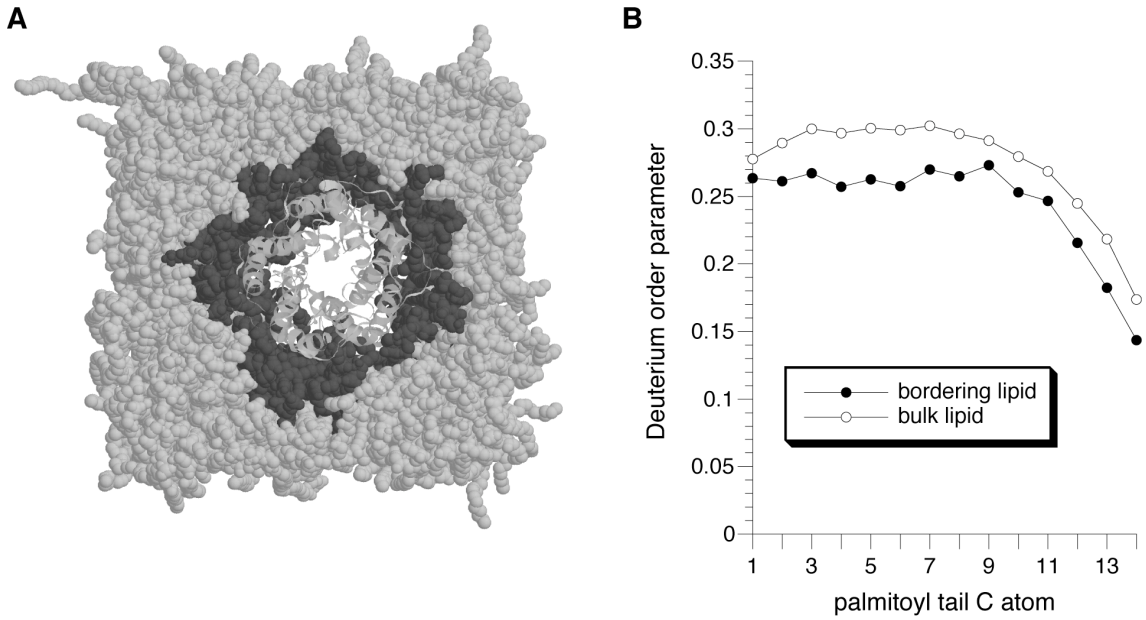

Pore Water Properties in the Wild-type MscL Simulation

Although the channel certainly does not sample an open state—or even an intermediate to an open state—during the simulations, consideration of waters in the pore region can give some insight into closed channel dynamics. As shown in Fig. 4.10, water in the closed Tb-MscL channel orients distinctly along the pore axis, with water O atoms pointing towards the intracellular region in the main pore and reversing their orientation in the wider region near the top of the membrane. This ordering most likely is driven by the helix dipoles of the TM1 helices, as the water oxygens point towards the helix N-terminus inside the pore and begin to reverse as they reach the extracellular side of the pore and pass the C-termini of the helices. The magnitude of dipole orientation is the

greatest in the most constricted part of the channel, around residue 21, where the fewest waters would have to be ordered to obtain this effect. However, the magnitude of ordering is not greatly affected by the increase of pore radius in the V21A simulation (Fig. 4.10). Similar trends of water dipole ordering explained by helix dipoles are seen in simulations of alamethicin channels, the OmpF porin, and KcsA channels (Guidoni et al., 2000; Tieleman and Berendsen, 1998; Tieleman et al., 1999b). In addition, charged TM1 residues, such as Asp 36, could play a role in water ordering. Such a distinct water orientation in the MscL pore is perhaps surprising since it is not an ion selective channel, but such electrostatic ordering would likely decrease in the presumably much wider open channel.

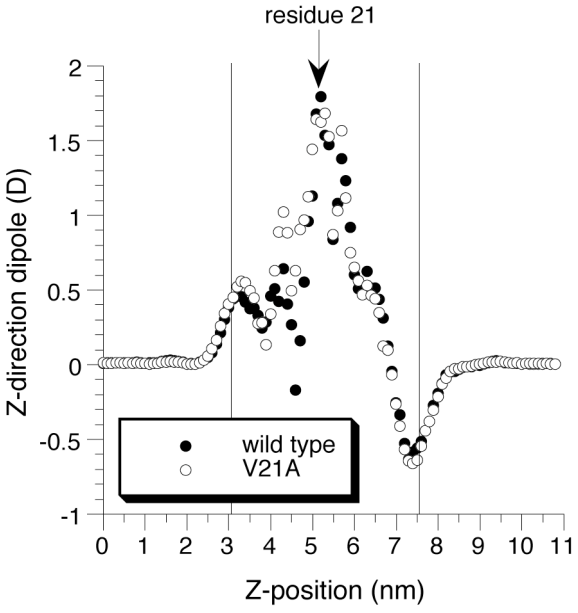

Figure 4.10: Average orientation of pore water dipoles along the membrane normal (Z-axis) over the last 1 ns of the wild-type and V21A simulations. Numbering on the Z-axis begins with the intracellular side of the simulation box at 0 nm. Positive dipole values result from the water O pointing towards the intracellular region (Z-position of zero); negative dipoles are directed in the opposite direction. The black vertical lines mark the average position of the phosphorous atoms of each lipid leaflet, and the average position of the "plug" residue 21 is denoted.

Summary

Simulations of the embedded channel showed the applicability of such computational methods to the Tb-MscL crystal structure. Wild-type and mutant trajectories showed an overall conservation of the crystal structure conformation. As expected, the TM regions show very little deviation from the crystal structure, while the extracellular loop and C-terminal regions are much more flexible. Simulations of two mutants, V21A and Q51E, showed no large changes in the global structure of the protein. It is possible that in a longer timescale simulation more significant changes would develop, but there is no hint of any such alterations in the over 1 ns of dynamics on each mutant presented here. Nonetheless, these mutations did lead to some interesting, more subtle changes in the trajectories. In particular, the Q51E mutation caused a dramatic alteration of intersubunit hydrogen bonding between residues 45 and 51. This mutation also caused an alteration in protein-lipid electrostatic interactions. One or both of these changes could lead to functional effects from the mutation, suggesting that further experimental studies of this and other mutations in this region could be interesting. The V21A mutation caused a widening of the constricted region of the pore. Although partially due to the steric reduction in the pore plug, the widening does extend past the close vicinity of residue 21. Although the widening was not accompanied by analogous structural deformation or instability in the pore region, it could be part of the perturbation leading to the lower gating tension of that mutant.

Several interesting aspects of protein-lipid interactions were apparent in the calculations. Half of the hydrogen bonds between protein and lipid, and two-thirds of those between extracellular loop and lipid, involved the ammonium moiety of the PE

headgroup, which represents an extremely small portion of the entire POPE lipid. Additionally, this functionality would not be present in other common lipids, implying that hydrogen bonding between Tb-MscL and lipid would be very dependent on the types of lipids present. This hydrogen bonding pattern may be related to differences in gating tension that have been observed for Tb-MscL in differing lipid environments, such as *E. coli* spheroplasts vs. azolectin membranes (Moe et al., 2000). An analogous dependence on lipid composition also has been observed for Eco-MscL gating tensions (Sukharev et al., 1993), so an increased understanding of lipid-specific interactions may be of general interest for MscL homologues. It is also noteworthy that protein-lipid hydrogen bonding was highly localized to a particular region in the extracellular loop. In Tb-MscL, this region directly after TM1 has a very divergent sequence from Eco-MscL and many other non-Mycobacterial MscL homologues (Maurer et al., 2000).

Thus, this series of simulations has given insight into the overall dynamics and conformational stability of wild-type Tb-MscL and two mutant forms of the channel. In addition, they suggest potential directions for future experimental and theoretical investigations of Tb-MscL, such as more complete considerations of protein-lipid interactions and the intersubunit interaction between residues 45 and 51.

References

Ajouz, B., C. Berrier, M. Besnard, B. Martinac, and A. Ghazi. 2000. Contributions of the different extramembranous domains of the mechanosensitive ion channel MscL to its response to membrane tension. *J. Biol. Chem.* 275:1015-1022.

Batiza, A. F., I. Rayment, and C. Kung. 1999. Channel gate! Tension, leak, and disclosure. *Structure* 7:R99-R103.

Berendsen, H. J. C., J. P. M. Postma, W. F. van Gunsteren, A. DiNola, and J. R. Haak. 1984. Molecular dynamics with coupling to an external bath. *J. Chem. Phys.* 81:3684-3690.

Berendsen, H. J. C., J. P. M. Postma, W. F. van Gunsteren, and J. Hermans. 1981. Interaction models for water in relation to protein hydration. In: Pullman B., editor. *Intermolecular Forces*. Dordrecht, the Netherlands: Reidel. p 331-342.

Berendsen, H. J. C., D. van der Spoel, and R. van Drunen. 1995. GROMACS: A message-passing parallel molecular dynamics implementation. *Comp. Phys. Comm.* 91:43-56.

Berger, O., O. Edholm, and F. Jähnig. 1997. Molecular dynamics simulations of a fluid bilayer of dipalmitoylphosphatidylcholine at full hydration, constant pressure, and constant temperature. *Biophys. J.* 72:2002-2013.

Bernèche, S., and B. Roux. 2000. Molecular dynamics of the KcsA K^+ channel in a bilayer membrane. *Biophys. J.* 78:2900-2917.

Berrier, C., A. Coulombe, C. Houssin, and A. Ghazi. 1989. A patch-clamp study of ion channels of inner and outer membranes and of contact zones of *E. coli*, fused into giant liposomes. Pressure-activated channels are located in the inner membrane. *FEBS Lett.* 259:27-32.

Blount, P., and P. C. Moe. 1999. Bacterial mechanosensitive channels: integrating physiology, structure and function. *Trends. Microbiol.* 7:420-424.

Blount, P., M. J. Schroeder, and C. Kung. 1997. Mutations in a bacterial mechanosensitive channel change the cellular response to osmotic stress. *J. Biol. Chem.* 272:32150-32157.

Blount, P., S. I. Sukharev, P. C. Moe, M. J. Schroeder, H. R. Guy, and C. Kung. 1996a. Membrane topology and multimeric structure of a mechanosensitive channel protein of *Escherichia coli*. *EMBO J.* 15:4798-4805.

Blount, P., S. I. Sukharev, M. J. Schroeder, S. K. Nagle, and C. Kung. 1996b. Single residue substitutions that change the gating properties of a mechanosensitive channel in *Escherichia coli*. *Proc. Natl. Acad. Sci. USA* 93:11652-11657.

Capener, C. E., I. H. Shrivastava, K. M. Ranatunga, L. R. Forrest, G. R. Smith, and M. S. P. Sansom. 2000. Homology modeling and molecular dynamics simulation studies of an inward rectifier potassium channel. *Biophys. J.* 78:2929-2942.

Chang, G., R. H. Spencer, A. T. Lee, M. T. Barclay, and D. C. Rees. 1998. Structure of the MscL homolog from *Mycobacterium tuberculosis*: a gated mechanosensitive ion channel. *Science* 282:2220-6.

Chiu, S.-W., S. Subramaniam, and E. Jakobsson. 1999a. Simulation study of a gramicidin/lipid bilayer system in excess water and lipid. I. Structure of the molecular complex. *Biophys. J.* 76:1929-1938.

Chiu, S.-W., S. Subramaniam, and E. Jakobsson. 1999b. Simulation study of a gramicidin/lipid bilayer system in excess water and lipid. II. Rates and mechanisms of water transport. *Biophys. J.* 76:1939-1950.

Dao-pin, S., U. Sauer, H. Nicholson, and B. W. Matthews. 1991. Contributions of engineered surface salt bridges to the stability of T4 lysozyme determined by directed mutagenesis. *Biochemistry* 30:7142-7153.

Egberts, E., and H. J. C. Berendsen. 1988. Molecular dynamics of a smectic liquid crystal with atomic detail. *J. Chem. Phys.* 89:3718-3732.

Feller, S. E., R. W. Pastor, A. Rojnuckarin, S. Bogusz, and B. R. Brooks. 1996. Effect of electrostatic force truncation on interfacial and transport properties of water. *J. Phys. Chem.* 100:17011-17020.

Fischer, W. B., M. Pitkeathly, B. A. Wallace, L. R. Forrest, G. R. Smith, and M. S. P. Sansom. 2000. Transmembrane peptide NB of influenza B: A simulation, structure and conductance study. *Biochemistry* 39:12708-12716.

Forrest, L. R., A. Kukol, I. T. Arkin, D. P. Tieleman, and M. S. P. Sansom. 2000. Exploring models of the influenza A M2 channel: MD simulations in a phospholipid bilayer. *Biophys. J.* 78:55-69.

Forrest, L. R., and M. S. P. Sansom. 2000. Membrane simulations: Bigger and better? *Curr. Opin. Struct. Biol.* 10:174-181.

Forrest, L. R., D. P. Tieleman, and M. S. P. Sansom. 1999. Defining the transmembrane helix of M2 protein from influenza A by molecular dynamics simulations in a lipid bilayer. *Biophys. J.* 76:1886-1896.

Guidoni, L., V. Torre, and P. Carloni. 1999. Potassium and sodium binding to the outer mouth of the K^+ channel. *Biochemistry* 38:8599-8604.

Guidoni, L., V. Torre, and P. Carloni. 2000. Water and potassium dynamics inside the KcsA K^+ channel. *FEBS Lett.* 477:37-42.

Hamill, O. P., and D. W. McBride, Jr. 1995. Mechanoreceptive membrane channels. *Am. Sci.* 83:30-37.

Häse, C. C., A. C. Le Dain, and B. Martinac. 1995. Purification and functional reconstitution of the recombinant large mechanosensitive ion channel (MscL) of *Escherichia coli*. *J. Biol. Chem.* 270:18329-18334.

Häse, C. C., R. F. Minchin, A. Kloda, and B. Martinac. 1997. Cross-linking studies and membrane localization and assembly of radiolabelled large mechanosensitive ion channel (MscL) of *Escherichia coli*. *Biochem. Biophys. Res. Commun.* 232:777-782.

Hendsch, Z. S., and B. Tidor. 1994. Do salt bridges stabilize proteins? A continuum electrostatic analysis. *Protein Sci.* 3:211-226.

Hess, B., H. Bekker, H. J. C. Berendsen, and J. G. E. M. Fraaije. 1997. LINCS: A linear constraint solver for molecular simulations. *J. Comp. Chem.* 18:1463-1472.

Husslein, T., P. B. Moore, Q. Zhong, D. M. Newns, P. C. Pattnaik, and M. L. Klein. 1998. Molecular dynamics simulation of a hydrated diphytanol phosphatidylcholine lipid bilayer containing an alpha-helical bundle of four transmembrane domains of the Influenza A virus M2 protein. *Faraday Discuss.* 111:201-208.

Kabsch, W., and C. Sander. 1983. Dictionary of protein secondary structure—Pattern-recognition of hydrogen-bonded and geometrical features. *Biopolymers* 22:2577-2637.

Kraulis, P. J. 1991. MOLSCRIPT: A program to produce both detailed and schematic plots of protein structures. *J. Appl. Cryst.* 24:946-950.

Law, R. J., L. R. Forrest, K. M. Ranatunga, P. La Rocca, D. P. Tieleman, and M. S. P. Sansom. 2000. Structure and dynamics of the pore-lining helix of the nicotinic receptor: MD simulations in water, lipid bilayers, and transbilayer bundles. *Proteins Struct. Funct. Genet.* 39:47-55.

Lee, R. E., P. J. Brennan, and G. S. Besra. 1996. *Mycobacterium tuberculosis* cell envelope. *Curr. Topics Microbiol. Immunol.* 215:1-27.

Levina, N., S. Tötemeyer, N. R. Stokes, P. Louis, M. A. Jones, and I. R. Booth. 1999. Protection of *Escherichia coli* cells against extreme turgor by activation of MscS and MscL mechanosensitive channels: Identification of genes required for MscS activity. *EMBO J.* 18:1730-1737.

Liedtke, W., Y. Choe, M. A. Martí-Renom, A. M. Bell, C. S. Denis, A. Sali, A. J. Hudspeth, J. M. Friedman, and S. Heller. 2000. Vanilloid receptor-related osmotically activated channel (VR-OAC), a candidate vertebrate osmoreceptor. *Cell* 103:525-535.

Lin, J.-H., and A. Baumgaertner. 2000. Stability of a melittin pore in a lipid bilayer: A molecular dynamics study. *Biophys. J.* 78:1714-1724.

Maurer, J. A., D. E. Elmore, H. A. Lester, and D. A. Dougherty. 2000. Comparing and contrasting *Escherichia coli* and *Mycobacterium tuberculosis* mechanosensitive channels (MscL): New gain of function mutations in the loop region. *J. Biol. Chem.* 275:22238-22244.

Miyamoto, S., and P. A. Kollman. 1992. SETTLE: An analytical version of the SHAKE and RATTLE algorithms for rigid water models. *J. Comp. Chem.* 13:952-962.

Moe, P. C., P. Blount, and C. Kung. 1998. Functional and structural conservation in the mechanosensitive channel MscL implicates elements crucial for mechanosensation. *Mol. Microbiol.* 28:583-592.

Moe, P. C., G. Levin, and P. Blount. 2000. Correlating a protein structure with function of a bacterial mechanosensitive channel. *J. Biol. Chem.* 275:31121-31127.

Murzyn, K., and M. Pasenkiewicz-Gierula. 1999. Construction and optimisation of a computer model for a bacterial membrane. *Acta Biochim. Polonica* 46:631-639.

Nakamaru, Y., Y. Takahashi, T. Unemoto, and T. Nakamura. 1999. Mechanosensitive channel functions to alleviate the cell lysis of marine bacterium, *Vibrio alginolyticus*, by osmotic downshock. *FEBS Lett.* 444:170-172.

Oakley, A. J., B. Martinac, and M. C. J. Wilce. 1999. Structure and function of the bacterial mechanosensitive channel of large conductance. *Protein Sci.* 8:1915-1921.

Opsahl, L. R., and W. W. Webb. 1994. Transduction of membrane tension by the ion channel alamethicin. *Biophys. J.* 66:71-4.

Ou, X. R., P. Blount, R. J. Hoffman, and C. Kung. 1998. One face of a transmembrane helix is crucial in mechanosensitive channel gating. *Proc. Natl. Acad. Sci. USA* 95:11471-11475.

Pasenkiewicz-Gierula, M., T. Róg, K. Kitamura, and A. Kusumi. 2000. Cholesterol effects on the phosphatidylcholine bilayer polar region: A molecular simulation study. *Biophys. J.* 78:1376-1389.

Perozo, E., A. Kloda, D. M. Cortes, and B. Martinac. 2001. Site-directed spin-labeling analysis of reconstituted MscL in the closed state. *J. Gen. Physiol.* 118:193-205.

Randa, H. S., L. R. Forrest, G. A. Voth, and M. S. P. Sansom. 1999. Molecular dynamics of synthetic leucine-serine ion channels in a phospholipid membrane. *Biophys. J.* 77:2400-2410.

Roux, B. 2002. Theoretical and computational models of ion channels. *Curr. Opin. Struct. Biol.* 12:182-189.

Sayle, R., and E. J. Milner-White. 1995. RasMol: Biomolecular graphics for all. *TIBS* 20:374-376.

Scholtz, J. M., H. Qian, V. H. Robbins, and R. L. Baldwin. 1993. The energetics of ion-pair and hydrogen-bonding interactions in a helical peptide. *Biochemistry* 32:9668-9676.

Schweighofer, K. J., and A. Pohorille. 2000. Computer simulation of ion channel gating: The M_2 channel of influenza A virus in a lipid bilayer. *Biophys. J.* 78:150-163.

Shrivastava, I. H., and M. S. P. Sansom. 2000. Simulations of ion permeation through a potassium channel: Molecular dynamics of KcsA in a phospholipid bilayer. *Biophys. J.* 78:557-570.

Smart, O. S., J. Breed, G. R. Smith, and M. S. P. Sansom. 1997. A novel method for structure-based predictions of ion channel conductance properties. *Biophys. J.* 72:1109-1126.

Smondyrev, A. M., and M. L. Berkowitz. 1999. Structure of dipalmitoylphosphatidylcholine/cholesterol bilayer at low and high cholesterol concentrations: Molecular dynamics simulation. *Biophys. J.* 77:2075-2089.

Smondyrev, A. M., and M. L. Berkowitz. 2000. Molecular dynamics simulation of dipalmitoylphosphatidylcholine membrane with cholesterol sulfate. *Biophys. J.* 78:1672-1680.

Spencer, R. H., G. Chang, and D. C. Rees. 1999. "Feeling the pressure": Structural insights into a gated mechanosensitive channel. *Curr. Opin. Struct. Biol.* 9:448-454.

Sukharev, S. I. 1999. Mechanosensitive channels in bacteria as membrane tension reporters. *FASEB J.* 13:S55-S61.

Sukharev, S. I., P. Blount, B. Martinac, F. R. Blattner, and C. Kung. 1994. A large-conductance mechanosensitive channel in *E. coli* encoded by MscL alone. *Nature* 368:265-268.

Sukharev, S. I., P. Blount, B. Martinac, and C. Kung. 1997. Mechanosensitive channels of *Escherichia coli*: The MscL gene, protein, and activities. *Annu. Rev. Physiol.* 59:633-657.

Sukharev, S. I., B. Martinac, V. Y. Arshavsky, and C. Kung. 1993. Two types of mechanosensitive channels in the *Escherichia coli* cell-envelope—Solubilization and functional reconstitution. *Biophys. J.* 65:177-183.

Tang, Y. Z., W. Z. Chen, C. X. Wang, and Y. Y. Shi. 1999. Constructing the suitable initial configuration of the membrane-protein system in molecular dynamics simulations. *Eur. Biophys. J.* 28:478-488.

Tieleman, D. P., and H. J. C. Berendsen. 1996. Molecular dynamics simulations of a fully hydrated dipalmitoylphosphatidylcholine bilayer with different macroscopic boundary conditions and parameters. *J. Chem. Phys.* 105:4871-4880.

Tieleman, D. P., and H. J. C. Berendsen. 1998. A molecular dynamics study of the pores formed by *Escherichia coli* OmpF porin in a fully hydrated palmitoyloleoylphosphatidylcholine bilayer. *Biophys. J.* 74:2786-2801.

Tieleman, D. P., H. J. C. Berendsen, and M. S. P. Sansom. 1999a. An alamethicin channel in a lipid bilayer: Molecular dynamics simulations. *Biophys. J.* 76:1757-1769.

Tieleman, D. P., J. Breed, H. J. C. Berendsen, and M. S. P. Sansom. 1998a. Alamethicin channels in a membrane: Molecular dynamics simulations. *Faraday Discuss.* 111:209-223.

Tieleman, D. P., L. R. Forrest, M. S. P. Sansom, and H. J. C. Berendsen. 1998b. Lipid properties and the orientation of aromatic residues in OmpF, influenza M2, and alamethicin systems: Molecular dynamics simulations. *Biochemistry* 37:17554-17561.

Tieleman, D. P., M. S. P. Sansom, and H. J. C. Berendsen. 1999b. Alamethicin helices in a bilayer and in solution: Molecular dynamics simulations. *Biophys. J.* 76:40-49.

Tu, K., M. L. Klein, and D. J. Tobias. 1998. Constant-pressure molecular dynamics investigation of cholesterol effects in a dipalmitoylphosphatidylcholine bilayer. *Biophys. J.* 75:2147-2156.

Wood, J. M. 1999. Osmosensing by bacteria: Signals and membrane-based sensors. *Microbiol. and Mol. Biol. Rev.* 63:230-262.

Woolf, T. B., and B. Roux. 1996. Structure, energetics, and dynamics of lipid-protein interactions: A molecular dynamics study of the gramicidin A channel in a DMPC bilayer. *Proteins Struct. Funct. Genet.* 24:92-114.

Yoshimura, K., A. Batiza, M. Schroeder, P. Blount, and C. Kung. 1999. Hydrophilicity of a single residue within MscL correlates with increased channel mechanosensitivity. *Biophys. J.* 77:1960-1972.

Chapter 5: Effects of Lipid Composition and Transmembrane Kinking on the Mechanosensitive Channel of Large Conductance (MscL)

Background

Mechanosensitive channels are proposed to play a central role in a variety of physiological processes, including touch, hearing, and circulation (Hamill and Martinac, 2001). The best studied channel of this class is the bacterial mechanosensitive channel of large conductance (MscL) (Batiza et al., 1999; Spencer et al., 1999). Rees and co-workers solved a crystal structure of *M. tuberculosis* MscL (Tb-MscL), showing the channel assembles as a homopentamer (Chang et al., 1998). In the structure, each of the channel subunits contains two transmembrane domains connected by an extracellular loop and a sizable C-terminal domain forming a helical bundle. The first transmembrane domain (TM1) lines the pore, while the second transmembrane domain (TM2) faces the lipid.

MscL is gated by the application of tension to the lipid bilayer (Sukharev et al., 1999), and its gating is not dependent on any other protein or cellular structure as it is fully functional when purified and reconstituted alone in lipid vesicles (Häse et al., 1995). When a bacterium experiences osmotic downshock it swells, producing a tension in the membrane. At a critical value for the tension, MscL opens, acting as a "safety valve" to prevent lysis (Levina et al., 1999; Nakamaru et al., 1999; Wood, 1999). The open channel is not ion selective and can pass relatively large organic ions (Cruickshank et al., 1997), leading to a predicted pore diameter of ≈40 Å. Researchers have debated whether MscL can pass small proteins, such as thioredoxin and EF-Tu (Ajouz et al., 1998; Berrier et al., 2000; Vasquez-Laslop et al., 2001).

It is clear that interactions between the channel and surrounding lipid are central to MscL gating. Not surprisingly, MscL gating properties are dependent on membrane

lipid composition. Recent work has shown that *E. coli* (Ec) MscL incorporated into lipid vesicles gates at a lower tension when the lipid tails are shortened (Kloda and Martinac, 2001; Perozo et al., 2002b). It is thought that the channel opens more easily because of better hydrophobic matching between the shorter lipid tails of the thinned membrane and the intermediate and/or open states of MscL. Such hydrophobic matching has been proposed to play a major role in channel gating, since the membrane thins upon the application of tension (Hamill and Martinac, 2001; Sukharev et al., 2001b). Other work has shown that the gating physiology of both Tb-MscL (Moe et al., 2000) and Ec-MscL (Sukharev et al., 1993) differs when the channels are expressed in spheroplasts versus incorporated into asolectin vesicles. However, systematic studies of the effects of lipid identity and composition on MscL gating have not been reported.

Molecular dynamics (MD) simulations can give further insight into how lipid composition affects MscL structure and dynamics on the molecular level. As described in Chapter 4, the Tb-MscL crystal structure has provided a starting point for previous MD simulations of the channel embedded in an explicitly represented lipid membrane (Elmore and Dougherty, 2001; Gullingsrud et al., 2001). Such simulations did point to some intriguing protein-lipid interactions (Elmore and Dougherty, 2001). However, each of these previous MD studies considered only one type of lipid, palmitoyloleoyl-phosphatidylethanolamine (POPE) (Elmore and Dougherty, 2001) or palmitoyloleoylphosphatidylcholine (POPC) (Gullingsrud et al., 2001), so comparisons of the effects of different lipids in directly analogous simulations were not possible. Similarly, most MD studies of membrane proteins only consider a single type of lipid (see (Roux, 2002) and (Forrest and Sansom, 2000) for recent reviews of these

simulations). Recent studies have compared how different lipids affect trajectories of glycophorin (Petrache et al., 2000b) and WALP peptides (Petrache et al., 2002). In particular, Petrache et al. investigated the hydrophobic matching of WALP peptides in membranes with two different tail lengths (2002). As well, other MD studies have focused on characterizing protein interactions with a single type of lipid through interaction energies and changes in lipid properties (Mihailescu and Smith, 2000; Tieleman et al., 1998; Woolf, 1998; Zhu et al., 2001). Using static protein-lipid systems, other computational methods have been used to evaluate the interaction energies between proteins and lipid membranes of varying lipid composition (Arbuzova et al., 2000; Murray et al., 1998; Murray and Honig, 2002). However, these electrostatic studies are limited as they generally do not consider possible changes in protein conformation between different lipid environments.

This chapter describes MD simulations of Tb-MscL embedded in a lipid membrane, addressing the effects of lipid headgroup type and lipid tail length on MscL. In a first set of simulations, directly comparable trajectories of Tb-MscL in POPE and POPC lipid were computed. These simulations show that the structure and dynamics of the MscL channel are directly affected by changes in lipid headgroup, particularly in the C-terminal region. In the second set of simulations, lipid tails were progressively reduced in length, producing a gradual thinning of the membrane over a multi-nanosecond trajectory. These simulations differ from previous MD simulations of proteins that separately embedded the protein of interest into lipids with differing chain lengths (Petrache et al., 2000b; Petrache et al., 2002). In the present study, gradual thinning could be particularly advantageous, as it may serve as a crude proxy for the

application of tension to the protein-lipid system. Since possible problems in attempting to simulate MscL gating with computationally applied tension have been outlined (Bilston and Mylvaganam, 2002), our indirect approach could be particularly useful. Overall, these shortening simulations support the previously proposed hydrophobic matching of MscL. The lipid shortening simulations implied that gating intermediates might have kinked TM2 helices. Thus, additional simulations and experiments with mutant MscL channels designed to have a TM2 were performed to further consider this possibility. Additionally, in light of recent extensive random mutagenesis of Ec-MscL (Maurer and Dougherty, 2003), consideration of protein-lipid and intersubunit interactions in both sets of trajectories further highlight the central importance of protein-lipid interactions to proper channel function.

Molecular Dynamics Simulations

General Simulation Setup

The Tb-MscL crystal structure (Chang et al., 1998) with all ionizable residues charged (Asp, Glu, Lys, and Arg; no His are present in Tb-MscL) and uncharged N- and C-termini (-NH_2 and -COOH) was used as the starting structure for the channel in all simulations. The termini were left uncharged since they are the extent of the experimentally determined structure but are not the physiological termini of the channel. This structure was initially embedded into an equilibrated POPE membrane (Tieleman and Berendsen, 1998) as in previous Tb-MscL MD simulations (Elmore and Dougherty, 2001). Throughout, the membrane was oriented in the *xy* plane, with the *z*-axis as the membrane normal. The positioning of the channel in the normal of the membrane (the *z*-

axis) was consistent with the EPR results of (Perozo et al., 2001). Unlike the simulations in Chapter 4, all residues in the Tb-MscL channel crystal structure (Ala 10-Arg 118) were included in the simulations. This was done because mutagenic data, described in Chapter 3, has begun to probe the functional and structural importance of the Tb-MscL C-terminal region, despite its demonstrated unimportance in Ec-MscL (Blount et al., 1996). Overall, this system included 545 protein residues, 290 POPE lipids, and 23,523 water molecules, for a total of 90,829 atoms; the initial system size is about 9.7 nm x 9.5 nm x 12.4 nm. The full simulation system is shown in Fig. 5.1. This initial system was treated analogously to previous simulations, applying 150 steps of steepest descents minimization to reduce close contacts and gradually heating to 310 K over 20 ps with restraints on all Cα atoms of the channel. All subsequent simulations were performed at 310 K.

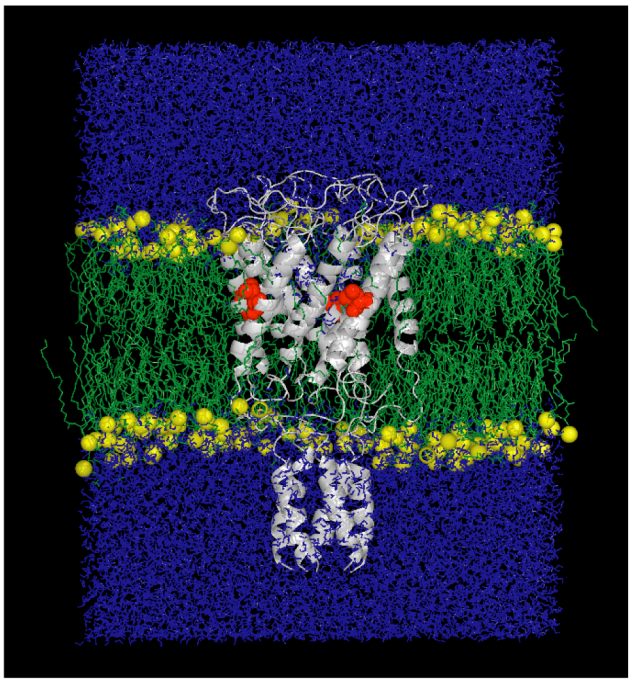

Figure 5.1: The full simulation system at the end of 100 ps of MD simulation. The channel is shown in white ribbon with residue L81, shown by EPR measurements to lie near the middle of the bilayer (Perozo et al., 2001), highlighted as red spacefilling. Water is depicted as blue wireframe, and lipid molecules are green wireframe with phosphate atoms in yellow spacefilling.

Simulations with Different Lipid Headgroups

In the initial POPE system, the full Cα restraints were maintained after heating for 180 ps. Subsequently, they were released in gradual steps over an additional 330 ps; afterwards no restraints were placed on the system.

The headgroup change from POPE to POPC was performed at the 1000 ps frame of the POPE trajectory. This point was chosen because the membrane had been allowed to grossly adjust to the channel after embedding, but the protein structure had not fully entered into its equilibrium interactions with the lipid. At this frame, all the hydrogens attached to the N of the ethanolamine moiety of the POPE headgroups were changed into methyl groups (Fig. 5.2A), and the system was subjected to 50 steps of steepest descents minimization to reduce newly introduced close contacts before extending the POPC trajectory for an additional 6 ns. The POPE trajectory was extended to a total of 5 ns.

Differences between PE and PC headgroup interactions may be due to differences in electrostatics. Recent work has advocated the use of particle mesh Ewald (PME) methods for optimal handling of long-range electrostatics in simulations of lipid bilayers and membrane proteins (Faraldo-Gómez et al., 2002; Feller et al., 1996). However, since others report that the two methods yield quite similar results for some systems (Capener and Sansom, 2002), we compared simulations of Tb-MscL in POPE that utilized either an electrostatic cutoff (1.8 nm) or PME for long-range electrostatics. The channel structures in these simulations were qualitatively similar except for the C-terminal region, which exhibited a greater deviation from the crystal structure in the cutoff simulation. Since recent experimental work, described in Chapter 3, has focused on this region in Tb-MscL and lipid interactions could be important in that region, we opted to use PME (Darden et

al., 1993) for long-range electrostatics in POPE and POPC comparison simulations, with 1.0 nm Coulombic and Lennard-Jones cutoffs. The PME calculations utilized a Fourier grid spacing of 0.10 nm and cubic interpolation.

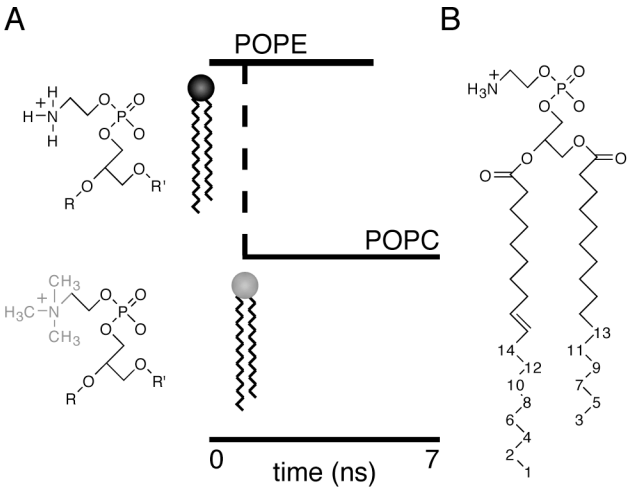

Figure 5.2: A) Chemical structures of POPE and POPC headgroups are shown on the left, with the portion differing in POPC highlighted in gray. On the right is a schematic of the lipid headgroup changing simulations. In the schematic, the dashed line shows where all lipids in the 1 ns frame of the POPE trajectory were converted to POPC.

B) The structure of 16/18 PE showing the order in which carbons were removed from lipid tails in lipid shortening simulations. As discussed in the text, the first two carbons were removed from the oleoyl chain, after which carbons were removed from alternating chains.

Simulations with Lipid Tail Shortening

For lipid shortening simulations, full Cα restraints were applied to the heated system for 80 ps. This was followed by a gradual release of those restraints over the following 165 ps of the trajectory; no restraints were placed on the system after that point.

Lipid tail shortening simulations started from the 500 ps frame of a POPE trajectory. Shortening was done by removing the terminal methyl group of one lipid tail and equilibrating the system for 300 ps. After this equilibration time, another methyl was removed, followed by another equilibration window. The order in which carbons were removed is depicted in Fig. 5.2B. Initially, the lipid tails were 16 (palmitoyl) and 18

(oleoyl) C atoms in length; this is denoted as 16/18 lipid throughout this paper. The two terminal carbons of the 18 C chain were removed first. After this removal, the lipid was 16/16, and carbons were removed from alternating tails, beginning with the tail that was initially 16 C. In the case where the lipid was shortened to 10/10, the oleoyl double bond was converted to a single bond between the removal of C11 and C12. This was done in order to prevent an unsaturated unit from occurring at the end of a lipid tail, as this could lead to unusual lipid dynamics. After the lipid tails were reduced to the desired length—14/14, 12/12, or 10/10—the trajectory was extended (2 ns for 14/14 and 12/12 simulations, and 5 ns for the 10/10 simulation). Since previous embedded systems began to show equilibration of protein-lipid interactions after 1 ns (Zhu et al., 2001), these extensions allowed the system to adjust before an averaging period for analyses. The 16/18 trajectory was extended to a total of 3 ns.

In order to confirm that the 300 ps equilibration between shortening steps is sufficiently long, an additional shortening trajectory to 14/14 was performed using 600 ps equilibration times. This trajectory was qualitatively similar to the 300 ps step trajectory, although some details of the simulations were different. For example, the 600 ps trajectory showed somewhat less overall bilayer thinning. This might occur because the bilayer initially overcompensates after some lipid shortening events, and this slight overthinning is not fully remediated in the shorter time steps. Also, the relative sizes of the hydrophobic matching effects (border/bulk lipid thickness differences and protein hydrophobic surface length adjustment) differed between the simulations, although their total effect (defined in Eq. 1 below) was the same. Nonetheless, since both methods led

to the same interpretations for the system, the more extensive 300 ps step shortening simulations will be discussed in this work.

Lennard-Jones energies and electrostatics were cutoff at 1.0 nm and 1.8 nm, respectively, in these simulations. Similar cutoffs were used in previous simulations of Tb-MscL (Elmore and Dougherty, 2001) and other ion channels, such as KcsA (Shrivastava and Sansom, 2000; Shrivastava et al., 2002). Despite the possible benefits of PME methods described above, cutoffs were utilized for long-range electrostatics in these simulations to increase computational efficiency and allow consideration of a greater variety of lipid lengths and shortening protocols. Moreover, these simulations were primarily aimed at investigating the lipid exposed TM domains, which are generally dominated by hydrophobic interactions, while the main differences between cutoff and PME simulations appeared to be in the C-terminal domain of the channel.

F80P Simulations

The F80P mutation was made to the POPE embedded MscL system described above before minimization. After making the mutation, the system was minimized for 150 steps of steepest descents minimization. Molecular dynamics simulations on the minimized F80P system were performed using the same heating and restraint release protocol utilized for the lipid headgroup simulations. Also, PME methods were used to compute long-range electrostatics for these simulations. The F80P simulation was extended to a total of 5 ns.

Simulation Details

All minimizations and MD simulations were performed using the GROMACS 3 suite of programs (Berendsen et al., 1995; Lindahl et al., 2001). The protocols for MD used in this study were analogous to those used in our previous Tb-MscL simulations (Elmore and Dougherty, 2001). Lipid parameters were from (Berger et al., 1997), with additional parameters for the oleoyl double bond taken from the GROMOS force field. GROMACS atomic parameters were used for protein and water, with some non-bonded parameters determined by standard combination rules. All MD runs used a time step of 2 fs along with the LINCS routine to constrain bond lengths (Hess et al., 1997) and SETTLE to constrain rigid water geometries (Miyamoto and Kollman, 1992). Structures from the trajectories were stored every 0.5 ps for analysis. The NPT ensemble was employed with anisotropic pressure coupling in each direction to 1 bar with a time constant (τ_p) of 1.0 ps (Berendsen et al., 1984); this coupling scheme should allow the bilayer system to properly adjust to the embedded protein and alterations in lipid composition. Temperatures were coupled separately for protein, lipid, and solvent to a temperature bath with a coupling constant (τ) of 0.1 ps (Berendsen et al., 1984).

Analysis of the trajectories was primarily performed with the GROMACS suite. All average properties, such as energies and distances, were computed over the final 1 ns of a particular trajectory, unless otherwise noted. Interaction energies were averaged over all saved frames, including both short and long-range electrostatics and Lennard-Jones energies. Due to the difficulty of calculating long-range energies between several different portions of the system with PME, per residue long-range interaction energies were calculated with cutoffs of 2.25 nm for simulations run with PME. These energies

were unaffected qualitatively by changing the cutoff value used for this analysis. The definitions of the protein regions—TM1, extracellular loop, TM2 and C-terminal—were residues 15-43, 44-68, 69-89, and 90-118, respectively, as defined previously (Maurer et al., 2000). Hydrogen bonds were defined geometrically as interactions in which the distance between the hydrogen and the acceptor is < 0.25 nm and the interaction angle is ≤ 60°; amide N atoms were omitted as possible hydrogen bond acceptors. Bordering lipids were defined as those with an average minimal distance of 0.35 nm or less from the channel, as in past Tb-MscL simulations (Elmore and Dougherty, 2001). Additional analyses were performed using the HOLE (Smart et al., 1997) and HELANAL (Bansal et al., 2000) programs. Statistical analyses were performed using SPSS (SPSS, Inc.). Molecular graphics were generated with Pymol (DeLano, W.L., http://www.pymol.org).

Simulations with Different Lipid Headgroups

Overall Comments

The transformation of lipid from POPE to POPC resulted in a system that adjusted and stabilized its membrane properties, such as lipid density and lipid P-P distance, in a few ns (data not shown). This included the expected lateral spreading of the PC membrane accompanied by an overall thinning of the bilayer. As well, the protein was generally stable throughout equilibration. The overall channel RMS deviation from the crystal structure was very similar for the first few ns following the change to POPC (Fig. 5.3). However, there was then a rapid transition in the RMS deviation around 2 ns after the alteration. This transition corresponded to changes in the structure of the C-terminal domain. The RMS deviations for other regions of the protein remained very

similar between the trajectories and were comparable to those observed in previous Tb-MscL simulations (Elmore and Dougherty, 2001; Gullingsrud et al., 2001).

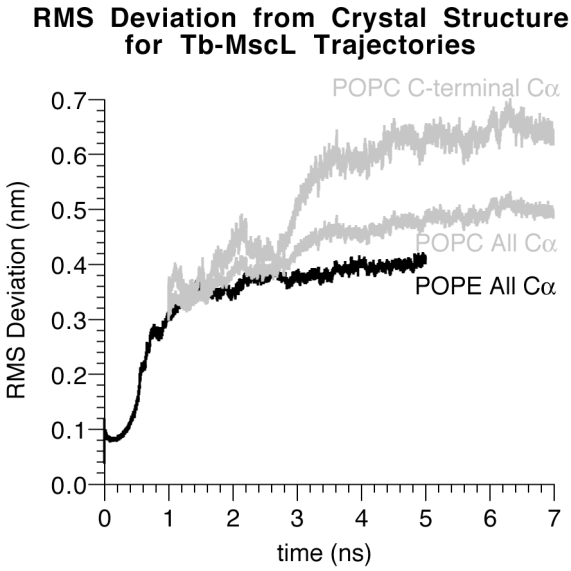

Figure 5.3: RMS deviation from crystal structure for POPE (black) and POPC (gray) trajectories. These values were calculated for each frame of the simulations by first fitting all protein C□ to the crystal structure. RMS deviations after fitting are reported for all C□ in both trajectories and for C□ in only the C-terminal region in the POPC trajectory.

The number of protein-lipid hydrogen bonds decreased upon the change from POPE to POPC (Fig. 5.4). Previous simulations in POPE had shown that the lipid ethanolamine moiety was the donor in a high proportion of all MscL-lipid hydrogen bonds (Elmore and Dougherty, 2001). Since such hydrogen bond donation is not possible with POPC, the observed decrease in hydrogen bonding was expected. Diminished hydrogen bonding was most notable in the extracellular loop (Fig. 5.4), which after equilibration had only 40% as many hydrogen bonds in POPC as in POPE. The drop in the C-terminal region was also marked, but of a lower magnitude (69% of POPE).

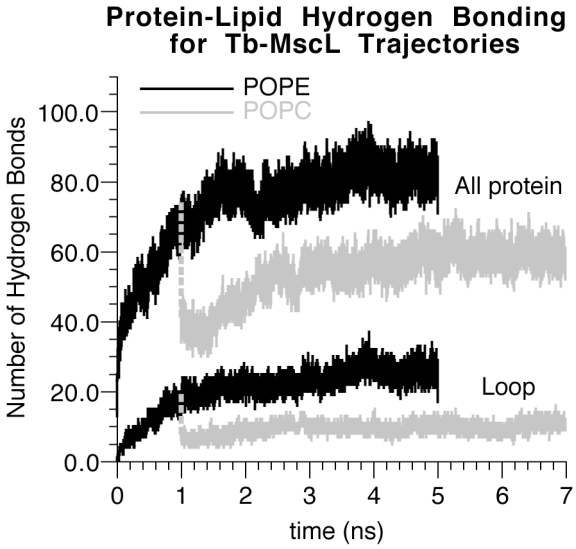

Figure 5.4: Number of hydrogen bonds between lipid and either the entire channel or only the extracellular loop in the POPE and POPC trajectories. Dashed lines show where POPE lipids were converted to POPC at 1 ns.

Lipid-Dependent Conformation of the C-terminal Region

The most notable effects resulting from changing the lipid headgroup from PE to PC are in the Tb-MscL C-terminal region. As discussed above, this region shows a structural transition about 2 ns after the change, resulting in greatly increased RMS deviation from the crystal structure (Fig. 5.3). In this transition, the upper portion of the C-terminal region appears to adjust its conformation, leading the helical regions to approach the membrane more closely (Fig. 5.5). The decrease in C-terminal protein-lipid hydrogen bonding interactions in POPC likely plays a role in this conformational transition. The energetic factors leading to the observed structural changes can be considered by examining protein-lipid interaction energies per residue in the two trajectories (Fig. 5.6A). In POPC, protein-lipid interactions are markedly decreased at Y94 and E102. Without these strong interactions, the channel rearranges in POPC to make interactions at K99 and K100 more favorable. These structural changes bring the C-terminal region closer overall to the membrane (Fig. 5.5B), increasing lipid interaction with D108 and E116 (Fig. 5.6A). As well, these rearrangements lead to the opposite

effect in intersubunit interactions at the same sites: decreased intersubunit interactions at K99 and K100 and more favorable intersubunit interactions at E102 (Fig. 5.6B). Most of the residues showing altered lipid interactions are highly conserved among MscL orthologues (Maurer et al., 2000). K99, K100, and E102 are part of a highly charged region found in all orthologues and determined to be essential for channel function in cleavage studies of Ec-MscL (Blount et al., 1996). D108 and E116 also have acidic counterparts in other MscL channels. Thus, lipid interactions noted in these simulations may play a general role in influencing the structure and the functional role of MscL C-terminal regions.

Figure 5.5: Pictures of the final frames of the POPE (A) and POPC (B) trajectories, with the protein shown as white ribbon and the lipid phosphate atoms shown as gray spacefilling.

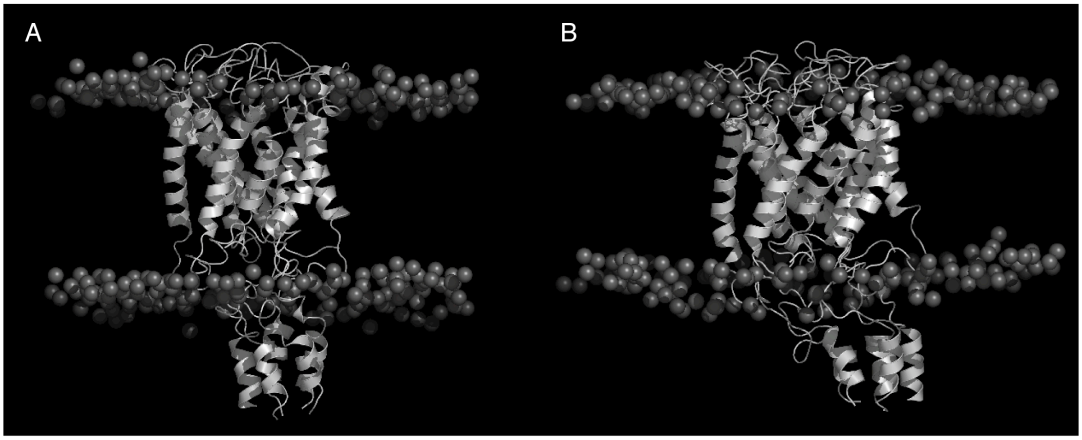

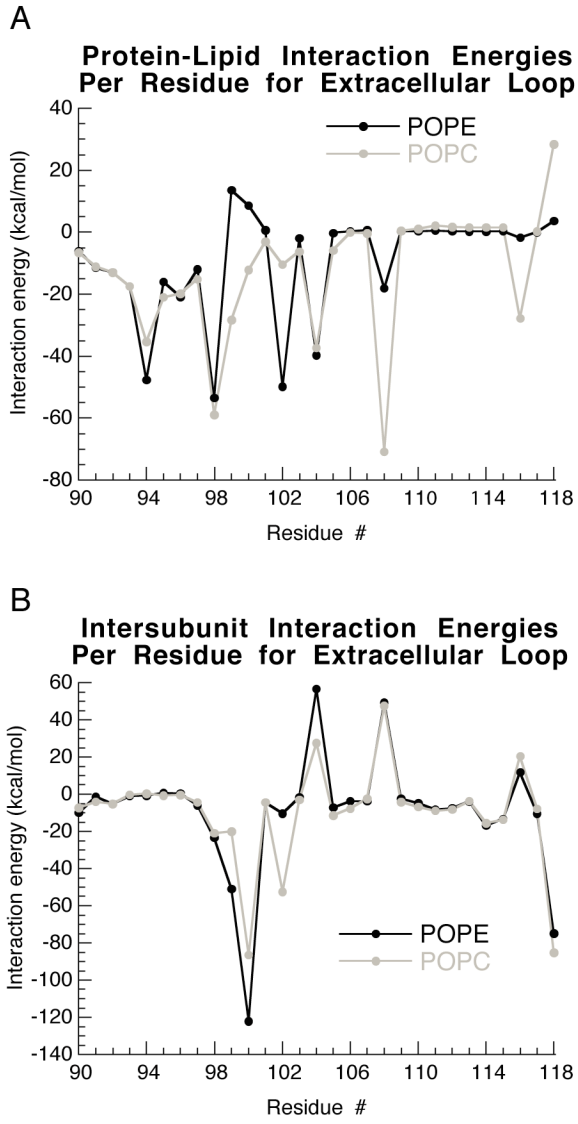

Figure 5.6: Protein-lipid (A) and intersubunit (B) interaction energies per residue for the C-terminal region in POPE (black) and POPC (gray) simulations.

Thus, it appears that interactions with POPE lipids can promote the crystal structure conformation of the Tb-MscL C-terminal helical domain. Recent data (reported in Chapter 3) has shown that some single site mutations in this region lead to altered thermal stability as determined by CD melting studies. It would be particularly interesting to determine the relationship between these structural changes and Tb-MscL function. As well, the gating tension of Tb-MscL is quite high (compared to that of Ec-

MscL) when expressed in *E. coli* spheroplasts (Moe et al., 2000), which have a high proportion of PE lipid (≈ 75%) in their inner membrane (Raetz, 1978). Conversely, *M. tuberculosis* membranes contain comparatively little PE lipid, less than 15% of their total lipid (Khuller et al., 1982; Lee et al., 1996). Instead, the majority of their membrane consists of glycolipids, phosphatidylinositol mannosides (PIMs). Although the sugars on PIMs do have hydroxyl groups that could serve as hydrogen bond donors, they would not form interactions as strong as the charged hydrogen bonds from PE headgroups. However, since PIMs are most prevalent in the outer leaflet of the membrane, such interactions may be most relevant in the extracellular loop region discussed below. Interestingly, ornithine-based lipids, which contain an amine moiety and are hypothesized to be functionally interchangable with PE lipids (Wilkinson, 1972), have been isolated from *M. tuberculosis* (Lanéelle et al., 1990); however, there is no direct evidence ornithine lipids are located in the *M. tuberculosis* plasma membrane (Daffé and Draper, 1998). These observations lead to the intriguing idea that the difficulty of gating Tb-MscL in spheroplasts may be related to its adaptation for a different native lipid environment. Such a proposal merits further experimental consideration with electrophysiological and structural measurements.

The promotion of the crystal structure C-terminal conformation by lipid interactions may also reconcile some apparently conflicting results concerning the Tb-MscL C-terminal region. Previous MD simulations of the C-terminal region predicted that the region would only maintain its helical structure at low pH (or with neutralizing mutations) (Elmore and Dougherty, 2001). Similarly, individual peptides with the sequence of the Tb-MscL C-terminal region only showed significant helicity at a low pH.

However, these peptides showed significant □-helicity at physiological pH when attached to a TASP system (Kochendoerfer et al., 2002). The TASP system started at residue 102 of the C-terminal region, which means that the TASP would have imposed structural constraints in the region involved with POPE-protein interactions. Conversely, the previous MD simulations of the C-terminal region alone included no lipid and only had moderate restraints on residues 94 and 95, more N-terminal than either the TASP attachment to the peptide or some residues that appear to mediate important lipid interactions in our present simulations. Thus, all these studies highlight that the structure and dynamics of the C-terminal region depend on the interplay of protein-protein and protein-lipid interactions in the region directly following TM2.

Extracellular Loop Region

In addition to the marked decrease in hydrogen bonding described above, the protein-lipid energy profile for the extracellular loop region shows decreased interactions after the change from POPE to POPC (Fig. 5.7A). Changes are particularly evident for two residues at the water/lipid interface, R45 and D68. This drop in protein-lipid interactions does not appear to be compensated by increased protein intersubunit interactions in POPC (Fig. 5.7B). However, despite these energetic changes resulting from the lipid headgroup alteration, no clear structural correlates were evident in the loop region in either measurements of RMS deviation and fluctuation or by visual inspection (data not shown). Since previous work has proposed functional importance

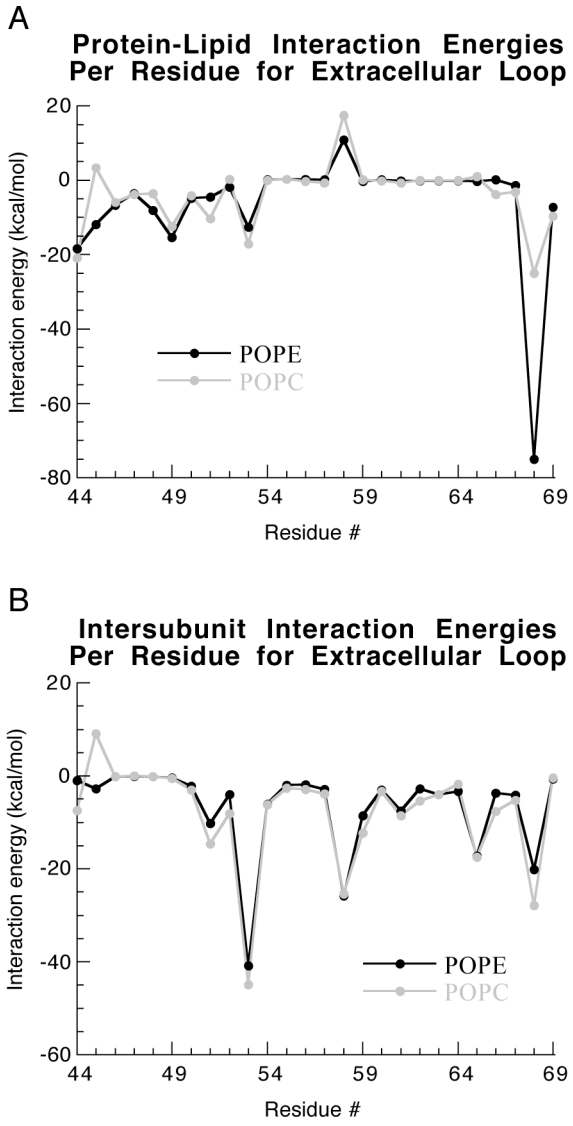

Figure 5.7: Protein-lipid (A) and intersubunit (B) interaction energies per residue for the extracellular loop region in POPE (black) and POPC (gray) simulations.

for this region in Tb-MscL (Maurer et al., 2000) and Ec-MscL (Ajouz et al., 2000), further site-specific dissection may implicate a functional importance of interactions modulated by lipid changes in this region. As well, unlike in the C-terminal region these Tb-MscL lipid interacting residues are not well conserved among MscL orthologues outside of the Mycobacteria (Maurer et al., 2000). In fact, D68 is aligned, or closely aligned, with a positively charged K or H residue in most non-Mycobacterial channels, including Ec-MscL. These differences could be related to the known physiological

differences between Tb-MscL and other MscL channels (Moe et al., 1998; Moe et al., 2000).

Simulations with Lipid Tail Shortening

Overall System Adjustment to Lipid Shortening

To simulate the bilayer thinning that accompanies a rise in tension, we progressively shortened the lipid tails by successive removals of terminal methyl groups of the lipid chains. The lipid bilayer adjusted quite rapidly to the removal of each methyl group. Bilayer thickness, measured by the distance between phosphorous atoms on opposite sides of the bilayer, decreased quickly after each shortening step and generally remained level after a few hundred ps (Fig. 5.8A). On the average, each step thinned the membrane by 0.75-1 Å, which agrees with experimental measurements on lipid vesicle bilayers with varying tail lengths (Lewis and Engelman, 1983). In addition, the protein structure was not grossly altered in the simulations with lipid shortening, as shown by the RMS deviations between the trajectories and the starting crystal structure (Fig. 5.8B). The RMS deviation for all Cα is relatively high in these simulations, primarily due to large deviations in the extramembrane regions. The extracellular loop was fairly disordered in the crystal structure, and the C-terminal region does not exhibit the lipid stabilization noted above when PME is not used to compute long-range electrostatics, leading to disorder similar to simulations of this region without lipid present (Elmore and Dougherty, 2001). As well, the RMS fluctuations (data not shown) of Cα atoms in equilibrated systems were essentially identical, showing no clear regions of increased or decreased structural stability in the systems with shortened lipid.

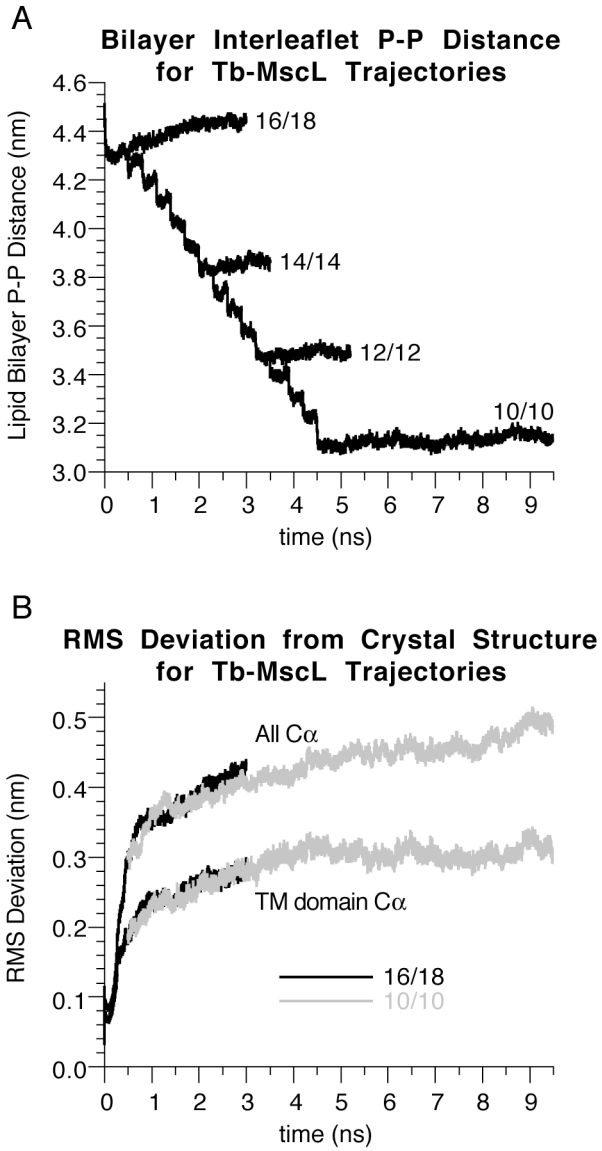

Figure 5.8: A) Distance between the phosphorous atoms of the two lipid bilayer leaflets for all lipid shortening trajectories. This distance was calculated as the difference between the average *z*-axis positions of all phosphorous atoms in the leaflets. B) RMS deviation from crystal structure for the trajectories ending with 16/18 lipid (black), and 10/10 lipid (gray). These values were calculated as in Figure 3; values are reported for the RMS deviation of all Cα and just the Cα of the TM1/TM2 regions. The RMS deviation values for the trajectories ending in 14/14 and 12/12 were essentially the same as those shown.

Evidence of Hydrophobic Matching in the Simulations

Hydrophobic matching between MscL and the surrounding lipid has been proposed as a possible driving force for channel gating (Hamill and Martinac, 2001; Sukharev et al., 2001b). Both the lipid properties and protein movements in the lipid shortening trajectories exhibit clear signs of such hydrophobic matching. First, during membrane thinning, lipids that directly border the protein thin less than lipids in the bulk of the membrane (Fig. 5.9). Thus, it appears that favorable interactions with the protein

"restrain" the nearby lipids from compressing as much as those that are not directly coupled to the protein. Interestingly, in the 16/18 trajectory the opposite effect is observed, in that the bordering lipids are actually thinner than those in the bulk. This implies that the channel actually matches better to a lipid somewhat thinner than 16/18. Thus, despite the tendency of a lipid with a given tail length to form a bilayer of a particular thickness, hydrophobic matching with the channel causes lipids close to the channel to adopt a different thickness.

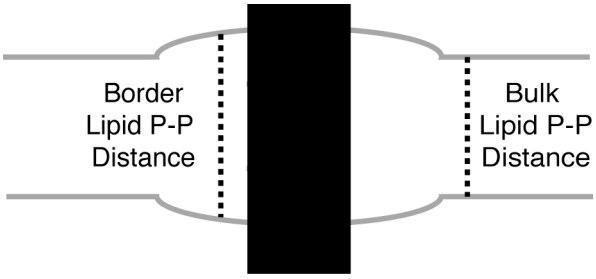

Lipid Tail	Border P-P (Å)	Bulk P-P (Å)	Δ (Border-Bulk) (Å)
16/18	43.3	44.8	-1.5
14/14	40.7	38.0	2.7
12/12	37.4	34.1	3.3
10/10	33.9	30.6	3.3

Figure 5.9: Average transbilayer distances between phosphorous atoms of lipids bordering Tb-MscL and in the bulk for lipid shortening simulations. The diagram on top schematically shows the difference between bordering and bulk lipids, with the channel depicted as a black rectangle and the lipid phosphorous atoms shown in gray. The average values for the final 1 ns of each lipid shortening simulation are given below along with the difference between values for the bordering and bulk lipids.

Changes in protein conformation in the simulations are also driven by hydrophobic matching. The majority of the channel-lipid interface consists of the second transmembrane domain and early portions of the C-terminal region. These regions can be used to define a "hydrophobic surface" on the outer face of Tb-MscL, as seen in Fig. 5.10. Although the exact definition of this surface is somewhat arbitrary, the analyses presented are robust to changing the definition by a few residues. The length of this hydrophobic surface along the bilayer normal (in the *z* direction) decreases during the

membrane thinning simulations. Fig. 5.10 shows this length averaged over all five subunits for trajectories with membranes of different thickness. Clearly, these surfaces attempt to compress to better match the shortened lipid.

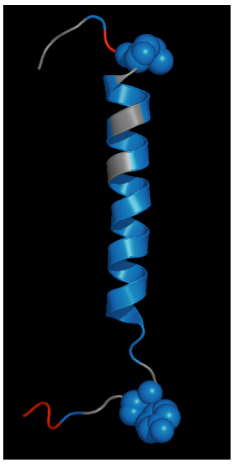

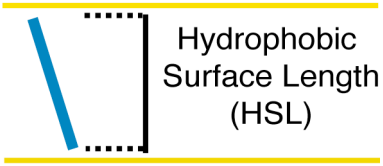

Lipid Tail	HSL (Å)
16/18	37.9
14/14	37.0
12/12	36.3
10/10	35.3

Figure 5.10: Average values for channel hydrophobic surface length (HSL) in lipid shortening simulations. The structure on the left denotes residues included in the "hydrophobic surface" of Tb-MscL, encompassing all of the TM2 helix and a portion of the C-terminus. Hydrophobic residues (Leu, Val, Ile, Ala, Phe, Tyr, Trp) are shown in blue, charged residues (Arg, Lys, Asp, Glu) are shown in red. The residues chosen as the termini of the "hydrophobic surface," L69 and Y94, are displayed in spacefilling. The diagram on the top right shows the definition of HSL for a single subunit, shown as a blue line, with the lipid phosphorous atoms denoted in yellow. Average HSL values for all lipid shortening simulations are given on the bottom right.

Thus, hydrophobic matching leads to a balance between bordering lipid being restrained from full thinning and the channel decreasing its hydrophobic length. One can calculate the extent to which these combined effects compensate for the overall thinning of the bulk membrane from 16/18 to X/X using the expression:

$$\%\ \textbf{compensation} = \frac{\textbf{border lipid effect} + \textbf{HSL effect}}{\textbf{total bulk lipid thinning}} = \frac{\left[\textbf{border PP(X/X)} - \textbf{bulk PP(X/X)}\right] + \left[\textbf{HSL(16/18)} - \textbf{HSL(X/X)}\right]}{\textbf{bulk PP(16/18)} - \textbf{bulk PP(X/X)}}$$

where PP(X/X) is the average interleaflet P-P distance for the lipid X/X and HSL(X/X) is the hydrophobic surface length in the lipid X/X. Using this expression, the hydrophobic matching effects are 40-50% of the overall bulk membrane thinning in the 14/14, 12/12, and 10/10 trajectories, with the percentage decreasing for the increasingly thinner bilayers. Thus, the system shows only a partial compensation for the thinning effects. Perhaps more extensive lipid or protein perturbations would occur on a longer simulation timescale. Also, since the percent compensation decreased with more extensive thinning, the lipid and channel may have become increasingly decoupled from one another under such extreme shortening.

A border lipid effect also was observed in the POPC simulation described above. In the bulk, POPC thins considerably compared to POPE, from 44.2 Å to 38.1 Å. This thinning is in agreement with experimental comparisons between PE and PC lipids with identical hydrocarbon tails (Petrache et al., 2000a; Rand and Parsegian, 1989). However, our magnitude of thinning is somewhat greater than the 1-4 Å observed experimentally. This may result from bulk lipids overcompensating from the lack of thinning in border lipids, which are highly restrained, maintaining a thickness of 43.2 Å. The protein HSL showed no change in POPC vs. POPE. These simulations used the PME electrostatic model, and interestingly, the thinning of the border lipids noted above for the 16/18 POPE system was not seen when PME electrostatics were used. Thus, the inverse effect seen for 16/18 border lipids may have been an artifact of the less sophisticated cutoff electrostatics. However, the POPC results confirm that hydrophobic matching upon thinning is insensitive to the electrostatic method employed.

Structural Rearrangements Upon Bilayer Thinning

The decreased average hydrophobic surface length discussed above is not a consequence of a smooth, concerted motion of the 5 subunits of MscL, but rather results from especially large movements in one or two of the subunits. We considered the possibility that these motions could provide insights into the early conformational changes of Tb-MscL resulting from membrane thinning upon the application of tension to the membrane. One feature of the simulations was that pore constrictions were observed in the 14/14 and 12/12 shortening simulations (Fig. 5.11A). These trajectories exhibited a narrowed pore in the region near the V21 plug residue, extending to more extracellular portions of the pore.

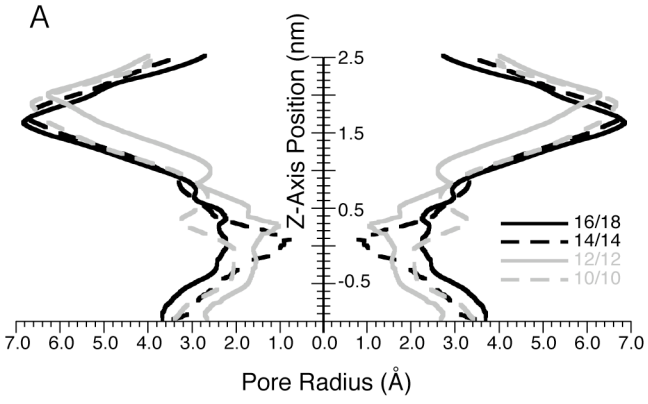

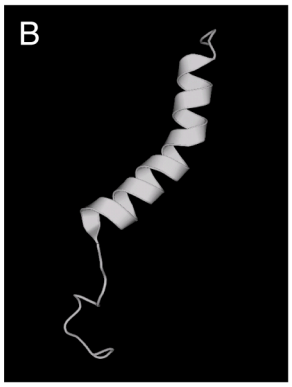

Figure 5.11: A) Pore radius profiles for lipid shortening simulations calculated with HOLE. Frames taken every 50 ps for the final 250 ps of a trajectory were averaged for the profiles presented. The *z*-axis position of each profile was adjusted such that V21 was at 0 nm.
B) An example of a kinked TM2 helix from the final frame of the 10/10 trajectory.

Our MD simulations also showed changes in TM2 conformation, and these contribute to the decreased hydrophobic surface length of the channel. However, these movements were not consistent between simulations. In some cases, the hydrophobic shortening resulted from tilting and/or kinking motions of the helical TM2 region (Fig. 5.11B). However, in other cases, thinning resulted from a compression of the less structured C-terminal portion of the hydrophobic surface. The potential role of TM2 kinking has been investigated using both additional MD simulations and experimental mutagenesis, as described below. This motion was focused on initially since helical kinking has been proposed in the gating of other ion channels (Tieleman et al., 2001).

Additionally, it is interesting to note that the channel seems to adjust its average hydrophobic length with relatively minor conformational changes. Thus, t he trajectories imply that although hydrophobic matching clearly occurs between Tb-MscL and the lipid membrane, this effect alone may not be sufficient to cause the major conformational changes leading to channel gating. This view is consistent with recent experiments showing that although MscL is easier to gate in vesicles with shorter lipid tail lengths, the channels still require some additional tension or perturbation in membrane structure to actually open (Perozo et al., 2002b).

Comparisons to Experimentally Derived Intermediate Gating Models

The motions observed in our lipid shortening simulations clearly do not lead to an open state of MscL. However, it is interesting to consider them in light of gating intermediates developed by Sukharev, Guy, and co-workers (Sukharev et al., 2001a; Sukharev et al., 2001b) and Perozo, Martinac, and co-workers (Perozo et al., 2002a;

Perozo et al., 2002b). The Sukharev/Guy intermediate model is much further along the gating pathway than any state we observe, making comparisons to it impossible. However, the relatively early Perozo/Martinac intermediate model, which was based on EPR measurements of spin-labeled MscL incorporated in thin (14/14) membranes, seems ideal for comparison. In fact, one significant feature of their model was a pore constriction analogous to that described above for the 14/14 and 12/12 trajectories (Perozo et al., 2002a). As well, this constriction was not observed for EPR measurements in the shortest lipids, similar to its disappearance upon shortening to 10/10 lipid in our simulations (Perozo et al., 2002b).

While this agreement between experiment and simulation is gratifying, another feature of the Perozo/Martinac model, a consistent TM1 rotation and tilt, was not observed in the simulations. Instead, extracellular portions of TM1 regions moved inwards towards the pore. Additionally, the Perozo/Martinac intermediate structure in 14/14 lipid does not propose any TM2 movements of the sort observed here. These differences between simulation and experiment could be a result of the relatively short timescale of these MD simulations. We note, however, that the model building used to interpret the experimental EPR was fairly simplistic, involving rigid helices and imposed five-fold symmetry (Perozo et al., 2002a). The MD simulations reported here do not involve such constraints and could therefore include helical deformations, such as TM2 kinking. Regardless, the idea of a slightly constricted intermediate state is intriguing, and determining its physiological relevance, if any, warrants further effort.

Correlations Between TM2 Energetic Profiles and Mutagenic Data

The protein-lipid and intersubunit interaction energy profiles for the Tb-MscL TM2 region both show distinct peaks that follow a helical pattern (Fig. 5.12A). This pattern occurs because one face of the TM2 helix faces the lipid bilayer, while another face interacts with the TM1 region of an adjacent subunit. These profiles are qualitatively unaltered by changes in lipid headgroup or lipid tail shortening.

Figure 5.12: A) Protein-lipid (yellow) and intersubunit (green) interaction energies per residue for the TM2 region of the POPE trajectory. Analogous profiles for the POPC and lipid shortening trajectories were essentially the same, showing identical energy peaks for protein-lipid and intersubunit energies. B) The correlation between Ec-MscL random mutagenesis data (Maurer and Dougherty, 2003) and MD interaction energies. The sequence alignment for Tb-MscL and Ec-MscL in the TM2 region is given on the two top rows. Below this, residues that are peaks for protein-lipid (yellow) and intersubunit (green) interactions in MD simulations are denoted. On the bottom three rows, results from random mutagenesis are summarized, showing Ec-MscL mutations which yielded GOF (blue), LOF (red), and wild-type-like (black) phenotypes.

A

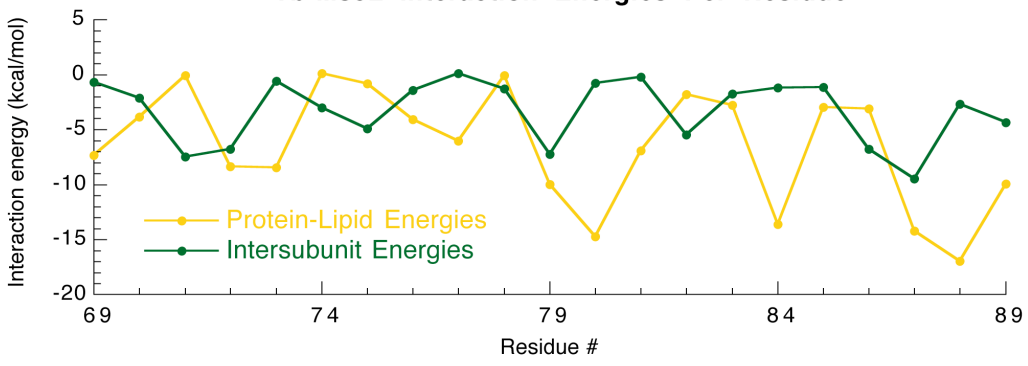

B

Tb-MscL	L69	N70	V71	L72	L73	S74	A75	A76	I77	N78	F79	F80	L81	I82	A83	F84	A85	V86	Y87	F88	L89
Ec-MscL	Y75	G76	V77	F78	I79	Q80	N81	V82	F83	D84	F85	L86	I87	V88	A89	F90	A91	I92	gap	F93	M94
Intersubunit																					
Lipid																					
LOF	D			YS	LN			D	G			P		E				F			
GOF									Y			R									
wt	C	S	AD	LI	V	R	DIS	AP	ILS	EGV	L		TVF	GL		CLSV	T	TVL		LS	

Recent random mutagenesis studies of Ec-MscL have characterized several mutations in the TM2 region (Maurer and Dougherty, 2003). Many such mutations were determined to be gain-of-function (GOF), i.e., gating more easily than wild type, or loss-of-function (LOF), i.e., gating with more difficulty than wild type. Since the sequence homology between Ec-MscL and Tb-MscL is fairly high in this region (Maurer et al., 2000), we have compared this mutagenic data with our computed energetic profiles. In particular, we were interested in seeing whether residues that interact with lipid or those that interact with other subunits would be more sensitive to mutation. The experimental and computational results are summarized in Fig. 5.12B. Strikingly, almost all mutations that lead to an altered channel phenotype occur at positions in Ec-MscL that align to lipid interacting residues in Tb-MscL; this distribution is statistically significant by Fisher's exact test ($p=0.042$). An analogous correlation does not exist for residues that mediate intersubunit interactions ($p=1.0$).

These results imply that lipid interactions are more important than intersubunit interactions in determining normal MscL function. Mutation of lipid interacting residues could feasibly alter channel function in at least two manners. First, these mutations could affect interactions between the channel and surrounding lipid that are necessary for the transduction of tension between the bilayer and protein. Since MscL is known to gate when reconstituted alone in lipid vesicles (Häse et al., 1995), such protein-lipid interactions must be essential to transmitting the gating tension to the channel. However, the LOF phenotype observed for many mutations at lipid interacting residues could also result from improper assembly of the channel in the membrane, since a non-functional channel would appear as LOF in the assay used for characterization (Maurer and

Dougherty, 2001). This possibility seems most likely for mutations that would place charged or polar residues directly next to the hydrophobic membrane if MscL assembled properly, for example Y75D. The importance of lipid interactions for proper channel assembly has been noted for other ion channels, such as KcsA (van Dalen et al., 2002).

Conversely, this analysis implies that residues which mediate MscL intersubunit interactions can be altered more readily without greatly affecting channel function. This may result from a redundancy in these interactions. There are several pairs of TM1-TM2 interactions that likely help transduce bilayer forces between the TM domains to gate the channel (Sukharev et al., 2001b), so other interactions may be able to compensate for the loss from a single mutation.

Investigation of the Role of TM2 Kinking in MscL Gating

Molecular Dynamics Simulations of F80P

The potential physiological relevance of the TM2 kinking behavior noted in simulations with gradually shortened lipid was probed further with a combination of MD simulations and experimental mutagenesis. First, we performed simulations of Tb-MscL with an F80P mutation in all five subunits (Fig. 5.13) to induce a kink in the middle of TM2 where a kink was observed in lipid shortening simulations. The F80P simulation showed an overall RMS deviation from crystal structure similar to that of other MscL simulations (data not shown), showing that the mutation did not appear to lead to an unreasonable trajectory. However, the channel did show significantly greater TM2 kinking in the F80P mutant trajectory (Fig. 5.14). While at almost all times after equilibration the wild-type structure would only have none or 1 kinked TM2 helix (as

evaluated using HELANAL (Bansal et al., 2000)), four or five of the helices typically were kinked after equilibration in the F80P trajectory (Fig. 5.14A). The proline-induced kink also leads to a notable "hinging" motion of the TM2 helices (Fig. 5.14B). Additionally, although the RMS *deviation* from crystal structure is similar for the TM helices in the wild-type and F80P trajectories, the RMS *fluctuations* of TM residues are higher in F80P (Fig. 5.15). Often an increase in RMS fluctuation, which is analogous to the temperature factor of a residue in crystal structures, is associated with increased structural instability in a region. Thus, this result hinted that a kink in TM2 might lead to structural destabilization of the closed state of MscL, thus promoting channel gating.

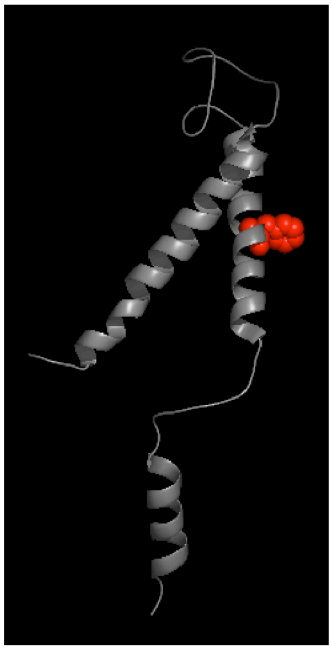

Figure 5.13: Single subunit from the Tb-MscL crystal structure with the F80 residue highlighted in red spacefilling.

However, the F80P simulation does not show characteristics associated with the putative "intermediate" structure from lipid shortening simulations. First, although the helices are generally kinked in the F80P simulation, they do *not* show a shorter

hydrophobic surface length (HSL) than the helices in the wild-type simulation (data not shown). Since TM2 kinking does not inherently cause HSL shortening, the shortening observed above as the channel adjusted to thinned bilayers was most likely not caused by TM2 kinking. Instead, the shortening of the HSL probably resulted from other channel conformational changes in the simulation. Second, the distinct pore narrowing observed both in lipid shortening simulations and the EPR studies of Perozo, Martinac and co-workers (Perozo et al., 2002a) is not observed in simulations of F80P (data not shown).

Figure 5.14: A) Histogram showing the number of saved frames during the last 1 ns with a given number of kinked TM2 helices for the wild-type and F80P simulations. Helical kinking was measured with HELANAL. B) Picture of TM2 helices from frames taken every 100 ps over the last 1 ns of the F80P simulation. The Cα of residues 69-80 from the different frames were superimposed in the picture.

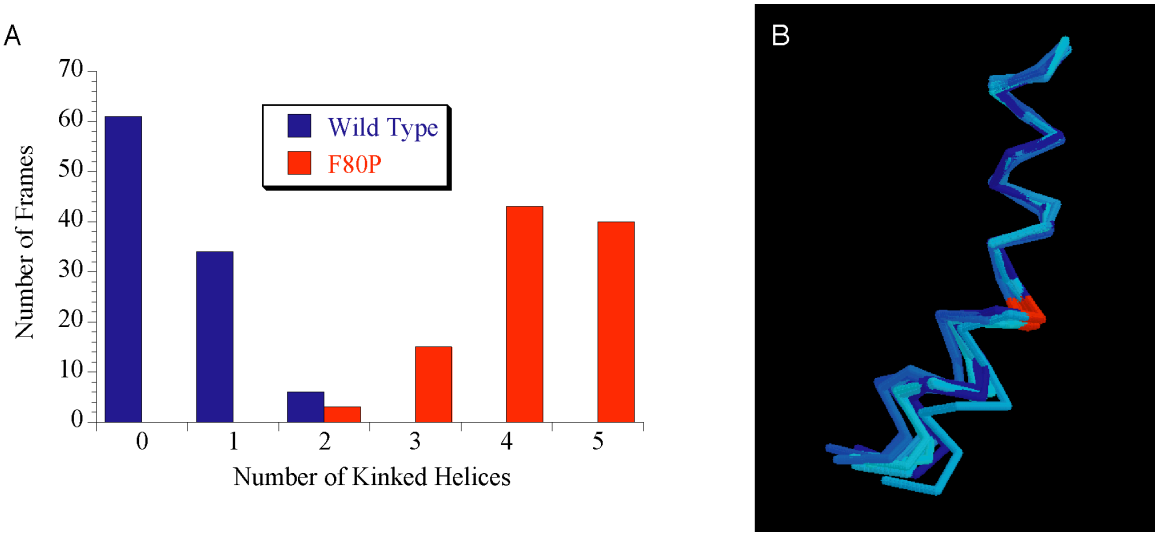

Together, these results imply that TM2 kinking is not likely to be a central feature of the MscL "intermediate" state proposed from experiments and computations with thinned lipid bilayers. In particular, inducing a kink in TM2 does not appear to drive the

structure to such as intermediat. However, the RMS fluctuation results (Fig. 5.15) imply that mutations inducing such a kink might lead to interesting channel phenotypes. Thus, a series of experiments was performed to characterize how such kink-inducing proline mutations in TM2 would alter channel function.

Figure 5.15: RMS fluctuation of Cα atoms per residue for TM1 (A) and TM2 (B) residues averaged over the last 1 ns of the wild-type (blue) and F80P (red) trajectories.

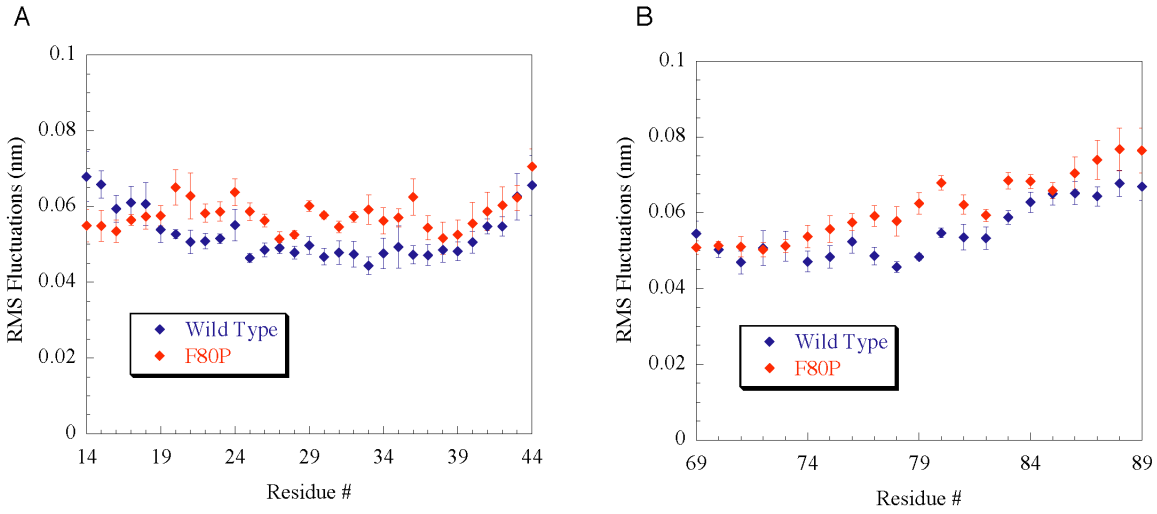

Experimental Characterization of Mutants with a TM2 Kink

To experimentally test the effect of transmembrane kinking, the *E. coli* (Ec) homologue of MscL was used since the very high gating tension of Tb-MscL makes its experimental characterization quite difficult. However, the generally high sequence homology between the TM domains of the two homologues (Maurer et al., 2000) makes comparisons between mutations in the TM2 region reasonable, such as the comparison of Tb-MscL computational results and Ec-MscL experimental results in the previous section. Thus, a series of Ec-MscL channels with a single proline mutation were made (D84P, F85P, L86P, I87P, V88P); Ec-MscL L86P is well-aligned with Tb-MscL F80P.

These residues encompass a full turn in the middle of TM2. All these mutations were made using the QuikChange Method (Stratagene) on a pB10b construct containing the Ec-MscL open reading frame. The mutants were functionally characterized using the Live/Dead BacLight method developed by Maurer and Dougherty and described in detail in (Maurer and Dougherty, 2001). In brief, bacterial cultures expressing mutant channels were subjected to a series of different osmotic downshock conditions, and the bacterial viability after downshock was measured using a fluorescent dye system. Since the MscL channel is thought to rescue bacteria from osmotic downshock, changes to the normal downshock response in bacteria expressing MscL mutants is attributed to changes in channel function. This method allows mutations to be characterized as having GOF, LOF, or wild-type-like phenotype.

Overall, all TM2 proline mutations led to a LOF channel (Table 5.1). These results further support the implication from the MD simulations that inducing TM2 kinking would not force the channel towards an intermediate state. One would expect that promoting the intermediate state of the channel would also make it easier for the channel to enter its open state, leading to a GOF phenotype. However, these results may at first seem contradictory to the RMS fluctuation results (Fig. 5.15) that showed a destabilization of the closed state resulting from TM2 kinking. However, a destabilization of the closed state would not necessarily imply that the channel would be pushed into the open state. Instead, it could be pushed into an unproductive non-native closed conformation. Looking at protein-lipid and intersubunit protein-protein interactions in the F80P simulation gives further insight into these possibilities.

Table 5.1: Experimentally characterized phenotypes of Ec-MscL TM2 mutants.

Mutant	Phenotype
D84P	LOF
F85P	LOF
L86P	LOF
L86A	wt-like
I87P	LOF
V88P	LOF

Intersubunit and Protein-Lipid Interactions of MscL TM2 Proline Mutants

Changes in the intersubunit interactions of TM2 residues in the F80P trajectory are consistent with the channel being pushed into a non-functional conformation by proline mutations. In the simulation, kinking at P80 brings the extracellular and intracellular ends of TM2 closer to TM1 (Fig. 5.16A). This closer proximity leads to a marked increase in intersubunit interactions of those TM2 residues (Fig. 16B). These increased interactions could effectively "glue" the ends of the two TM regions together, which would prevent the "sliding" motions of the TM helices proposed in the prevailing gating models of MscL (Perozo et al., 2002a; Sukharev et al., 2001a; Sukharev et al., 2001b). Thus, TM2 kinking induced by proline mutations may lock the channel into an occluded conformation, albeit one that is somewhat different than the native closed state.

A reduction in protein-lipid interactions could be another possible explanation for the LOF phenotype of TM2 proline mutations. The protein-lipid interaction profile of TM2 residues is very similar in the wild-type and F80P simulations with one clear exception—the mutation decreases the interaction of residue 80 with lipid (Fig. 5.17). Since analyses discussed above implied that altering MscL protein-lipid interactions often leads to altered channel function, the Ec-MscL L86P mutation could have caused a LOF

phenotype by this mechanism instead of by TM kinking. To control for this possibility, a L86A Tb-MscL mutation that would also dramatically decrease protein-lipid interactions was made and characterized by the Live/Dead BacLight method. Since L86A showed a wild-type-like phenotype (Table 5.1), it appears that the LOF phenotype observed for L86P was more likely due to TM kinking and not to reduced protein-lipid interactions.

Figure 5.16: A) Representative interaction between a kinked TM2 helix (yellow) with TM1 in the adjacent subunit (green). The P80 residue is shown in red. B) Intersubunit interactions energies per residue for TM2 in the wild-type and F80P simulations.

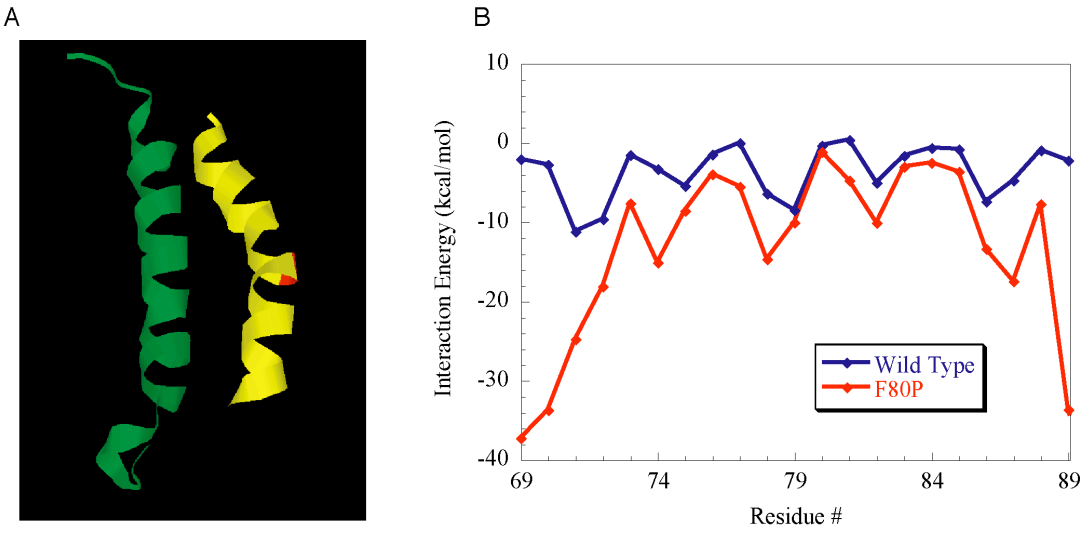

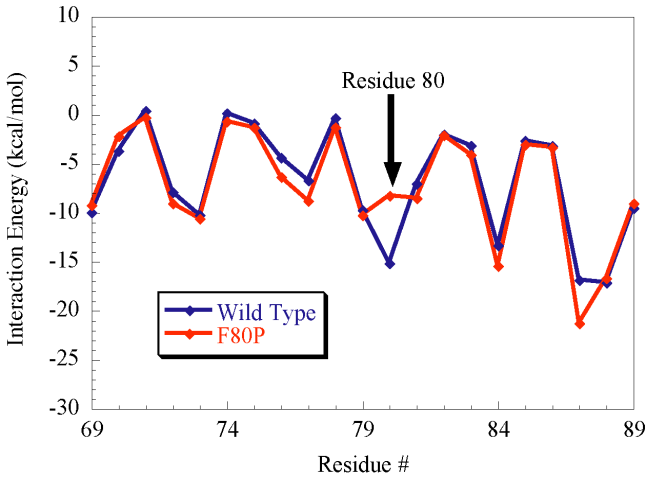

Figure 5.17: Protein-lipid interaction energies per residue for TM2 in the wild-type and F80P trajectory.

Summary

Considering multiple lipid environments in MD simulations of MscL has led to insights into protein-lipid interactions that help interpret previous experiments and propose future work. Although not currently standard practice, similar consideration of multiple types of membrane may also yield interesting results for other membrane protein simulations. Certainly, the methods employed here could undergo further optimization, such as considering the effect of employing PME electrostatics in shortening simulations or extending simulations further. However, the systems were stable under our current protocols and adjusted quite quickly to the changes in lipid molecules.

In simulations comparing Tb-MscL in POPE and POPC lipids, POPE clearly seems to promote a C-terminal structure closer to the crystal structure conformation than that seen in POPC. Such differences in conformation could be one manner by which lipid composition affects Tb-MscL physiology. As well, lipid interactions and hydrogen bonding profiles were different for POPE and POPC in the extracellular loop region, although these differences did not correlate with clear structural changes in the

simulations. Further experiments focusing on this region of the channel may clarify the importance of any such changes. Theoretical consideration of MscL in other types of lipid molecules using MD or other methods may lead to additional insights.

Trajectories in which lipid was gradually shortened showed that MscL does exhibit notable hydrophobic matching with lipid. Although these simulations did not lead to an open state of MscL—which would be shocking in the timescales considered—they did yield some hints of how the channel may adjust to membrane thinning. Such motions included constriction of the pore, which has also been observed experimentally (Perozo et al., 2002a), and kinking of TM helices. However, additional simulations and experimental mutagenesis showed that TM2 kinking is not likely an important feature of MscL intermediates. In fact, TM2 kinking led to a channel that was either non-functional or harder to gate than wild-type; increased interactions between TM1 and TM2 caused by kinking may have led to this LOF phenotype in TM2 proline mutants. Together, this data supports the use of rigid TM helices in the current gating models of MscL. It is also interesting to note that hydrophobic matching alone may only cause relatively small changes in channel structure, which would agree with data showing shorter lipids promote channel gating but are insufficient to induce channel gating by themselves (Perozo et al., 2002b).

Protein-lipid interactions in the TM2 region of MscL also showed intriguing correlations with experimental mutagenesis data (Maurer and Dougherty, 2003). In particular, residues that were seen in MD simulations to mediate protein-lipid interactions were mutagenically more sensitive than residues that mediated intersubunit interactions within the channel. This implies that protein-lipid interactions may be more important

than protein-protein interactions for proper MscL assembly and function. It will be interesting to consider if this is a general theme for mechanosensitive membrane proteins.

Overall, this work has begun to give some molecular insight into how lipid composition affects MscL structure and function. The importance of lipid interactions in MscL gating has been discussed in efforts to develop gating models of MscL, but it has been difficult to address such interactions directly in these models (Sukharev et al., 2001b). Hopefully, combinations of experiments and theoretical methods, such as those employed here, will be fruitful in developing an increasingly complete picture of the interplay between protein and membrane in mechanosensitive channel gating, and membrane protein function in general.

References

Ajouz, B., C. Berrier, M. Besnard, B. Martinac, and A. Ghazi. 2000. Contributions of the different extramembranous domains of the mechanosensitive ion channel MscL to its response to membrane tension. *J. Biol. Chem.* 275:1015-1022.

Ajouz, B., C. Berrier, A. Garrigues, M. Besnard, and A. Ghazi. 1998. Release of thioredoxin via the mechanosensitive channel MscL during osmotic downshock of *Escherichia coli* cells. *J. Biol. Chem.* 273:26670-26674.

Arbuzova, A., L. Wang, J. Wang, G. Hangyás-Mihályné, D. Murray, B. Honig, and S. McLaughlin. 2000. Membrane binding of peptides containing both basic and aromatic residues. Experimental studies with peptides corresponding to the scaffolding region of caveolin and the effector region of MARCKS. *Biochemistry* 39:10330-10339.

Bansal, M., S. Kumar, and R. Velavan. 2000. HELANAL: A program to characterize helix geometry in protiens. *J. Biolmol. Struct. Dyn.* 17:811-819.

Batiza, A. F., I. Rayment, and C. Kung. 1999. Channel gate! Tension, leak, and disclosure. *Structure* 7:R99-R103.

Berendsen, H. J. C., J. P. M. Postma, W. F. van Gunsteren, A. DiNola, and J. R. Haak. 1984. Molecular dynamics with coupling to an external bath. *J. Chem. Phys.* 81:3684-3690.

Berendsen, H. J. C., D. van der Spoel, and R. van Drunen. 1995. GROMACS: A message-passing parallel molecular dynamics implementation. *Comp. Phys. Comm.* 91:43-56.

Berger, O., O. Edholm, and F. Jähnig. 1997. Molecular dynamics simulations of a fluid bilayer of dipalmitoylphosphatidylcholine at full hydration, constant pressure, and constant temperature. *Biophys. J.* 72:2002-2013.

Berrier, C., A. Garrigues, G. Richarme, and A. Ghazi. 2000. Elongation factor Tu and DnaK are transferred from the cytoplasm to the periplasm of *Escherichia coli* during osmotic downshock presumably via the mechanosensitive channel MscL. *J. Bacteriology* 182:248-251.

Bilston, L. E., and K. Mylvaganam. 2002. Molecular simulations of the large conductance mechanosensitive (MscL) channel under mechanical loading. *FEBS Lett.* 512:185-190.

Blount, P., S. I. Sukharev, M. J. Schroeder, S. K. Nagle, and C. Kung. 1996. Single residue substitutions that change the gating properties of a mechanosensitive channel in *Escherichia coli*. *Proc. Natl. Acad. Sci. USA* 93:11652-11657.

Capener, C. E., and M. S. P. Sansom. 2002. Molecular dynamics simulations of a K channel model: Sensitivity to changes in ions, waters, and membrane environment. *J. Phys. Chem. B* 106:4545-4551.

Chang, G., R. H. Spencer, A. T. Lee, M. T. Barclay, and D. C. Rees. 1998. Structure of the MscL homolog from *Mycobacterium tuberculosis*: a gated mechanosensitive ion channel. *Science* 282:2220-6.

Cruickshank, C. C., R. F. Minchin, A. C. LeDain, and B. Martinac. 1997. Estimation of the pore size of the large-conductance mechanosensitive ion channel of *Escherichia coli*. *Biophys. J.* 73:1925-1931.

Daffé, M., and P. Draper. 1998. The envelope layers of mycobacteria with reference to their pathogenicity. *Advances in Microbial Physiology*, Vol 39. p 131-203.

Darden, T. D., D. York, and L. Pedersen. 1993. Particle mesh Ewald: An N log(N) method for Ewald sums in large systems. *J. Chem. Phys.* 98:10089-10092.

Elmore, D. E., and D. A. Dougherty. 2001. Molecular dynamics simulations of wild-type and mutant forms of the *Mycobacterium tuberculosis* MscL channel. *Biophys. J.* 81:1345-1359.

Faraldo-Gómez, J. D., G. R. Smith, and M. S. P. Sansom. 2002. Setting up and optimization of membrane protein simulations. *Eur. Biophys. J.* 31:217-227.

Feller, S. E., R. W. Pastor, A. Rojnuckarin, S. Bogusz, and B. R. Brooks. 1996. Effect of electrostatic force truncation on interfacial and transport properties of water. *J. Phys. Chem.* 100:17011-17020.

Forrest, L. R., and M. S. P. Sansom. 2000. Membrane simulations: Bigger and better? *Curr. Opin. Struct. Biol.* 10:174-181.

Gullingsrud, J., D. Kosztin, and K. Schulten. 2001. Structural determinants of MscL gating studied by molecular dynamics simulations. *Biophys. J.* 80:2074-2081.

Hamill, O. P., and B. Martinac. 2001. Molecular basis of mechanotransduction in living cells. *Physiol. Rev.* 81:685-740.

Häse, C. C., A. C. Le Dain, and B. Martinac. 1995. Purification and functional reconstitution of the recombinant large mechanosensitive ion channel (MscL) of *Escherichia coli*. *J. Biol. Chem.* 270:18329-18334.

Hess, B., H. Bekker, H. J. C. Berendsen, and J. G. E. M. Fraaije. 1997. LINCS: A linear constraint solver for molecular simulations. *J. Comp. Chem.* 18:1463-1472.

Khuller, G. K., R. Taneja, S. Kaur, and J. N. Verma. 1982. Lipid composition and cirulence of *Mycobacterium tuberculosis* H37rv. *Aust. J. Exp. Biol. Med. Sci.* 60:541-547.

Kloda, A., and B. Martinac. 2001. Mechanosensitive channel of *Thermoplasma*, the cell wall-less archaea: Cloning and molecular characterization. *Cell Biochem. and Biophys.* 34:321-347.

Kochendoerfer, G. G., J. M. Tack, and S. Cressman. 2002. Total chemical synthesis of a 27 kDa TASP protein derived from the MscL ion channel of *M. tuberculosis* by ketoxime-forming ligation. *Bioconjugate Chem.* 13:474-480.

Lanéelle, M. A., D. Promé, G. Lanéelle, and J. C. Promé. 1990. Ornithine lipid of *Mycobacterium tuberculosis*: Its distribution in some slow-growing and fast-growing mycobacteria. *J. Gen. Microbiol.* 136:773-778.

Lee, R. E., P. J. Brennan, and G. S. Besra. 1996. *Mycobacterium tuberculosis* cell envelope. *Curr. Topics Microbiol. Immunol.* 215:1-27.

Levina, N., S. Tötemeyer, N. R. Stokes, P. Louis, M. A. Jones, and I. R. Booth. 1999. Protection of *Escherichia coli* cells against extreme turgor by activation of MscS and MscL mechanosensitive channels: Identification of genes required for MscS activity. *EMBO J.* 18:1730-1737.

Lewis, B. A., and D. M. Engelman. 1983. Lipid bilayer thickness varies linearly with acyl chain length in fluid phosphatidylcholine vesicles. *J. Mol. Biol.* 166:211-217.

Lindahl, E., B. Hess, and D. van der Spoel. 2001. GROMACS 3.0: A package for molecular simulation and trajectory analysis. *J. Mol. Mod.* 7:306-317.

Maurer, J. A., and D. A. Dougherty. 2001. A high-throughput screen for MscL channel activity and mutational phenotyping. *Biochim. Biophys. Acta* 1514:165-169.

Maurer, J. A., and D. A. Dougherty. 2003. Generation and evaluation of a large mutational library from the *E. coli* mechanosensitive channel of large conductance, MscL. Implications for channel gating and evolutionary design. *J. Biol. Chem.* 278:21076-21082.

Maurer, J. A., D. E. Elmore, H. A. Lester, and D. A. Dougherty. 2000. Comparing and contrasting *Escherichia coli* and *Mycobacterium tuberculosis* mechanosensitive channels (MscL): New gain of function mutations in the loop region. *J. Biol. Chem.* 275:22238-22244.

Mihailescu, D., and J. C. Smith. 2000. Atomic detail peptide-membrane interactions: Molecular dynamics simulation of gramicidin S in a DMPC bilayer. *Biophys. J.* 79:1718-1730.

Miyamoto, S., and P. A. Kollman. 1992. SETTLE: An analytical version of the SHAKE and RATTLE algorithms for rigid water models. *J. Comp. Chem.* 13:952-962.

Moe, P. C., P. Blount, and C. Kung. 1998. Functional and structural conservation in the mechanosensitive channel MscL implicates elements crucial for mechanosensation. *Mol. Microbiol.* 28:583-592.

Moe, P. C., G. Levin, and P. Blount. 2000. Correlating a protein structure with function of a bacterial mechanosensitive channel. *J. Biol. Chem.* 275:31121-31127.

Murray, D., L. Hermida-Matsumoto, C. A. Buser, J. Tsang, C. T. Sigal, N. Ben-Tal, B. Honig, M. D. Resh, and S. McLaughlin. 1998. Electrostatics and the membrane association of Src: Theory and experiment. *Biochemistry* 37:2145-2159.

Murray, D., and B. Honig. 2002. Electrostatic control of the membrane targeting of C2 domains. *Mol. Cell* 9:145-154.

Nakamaru, Y., Y. Takahashi, T. Unemoto, and T. Nakamura. 1999. Mechanosensitive channel functions to alleviate the cell lysis of marine bacterium, *Vibrio alginolyticus*, by osmotic downshock. *FEBS Lett.* 444:170-172.

Perozo, E., D. M. Cortes, P. Sompornpisut, A. Kloda, and B. Martinac. 2002a. Open channel structure of MscL and the gating mechanism of mechanosensitive channels. *Nature* 418:942-948.

Perozo, E., A. Kloda, D. M. Cortes, and B. Martinac. 2001. Site-directed spin-labeling analysis of reconstituted MscL in the closed state. *J. Gen. Physiol.* 118:193-205.

Perozo, E., A. Kloda, D. M. Cortes, and B. Martinac. 2002b. Physical principles underlying the transduction of bilayer deformation forces during mechanosensitive channel gating. *Nature Struct. Biol.* 9:696-703.

Petrache, H. I., S. W. Dodd, and M. F. Brown. 2000a. Area per lipid and acyl length distributions in fluid phosphatidylcholines determined by H-2 NMR spectroscopy. *Biophys. J.* 79:3172-3192.

Petrache, H. I., A. Grossfield, K. R. MacKenzie, D. M. Engelman, and T. B. Woolf. 2000b. Modulation of glycophorin A transmembrane helix interactions by lipid bilayers: Molecular dynamics calculations. *J. Mol. Biol.* 302:727-746.

Petrache, H. I., D. M. Zuckerman, J. N. Sachs, J. A. Killian, R. E. I. Koeppe, and T. B. Woolf. 2002. Hydrophobic matching mechanism investigated by molecular dynamics simulations. *Langmuir* 18:1340-1351.

Raetz, C. R. 1978. Enzymology, genetics, and regulation of membrane phospholipid synthesis in *Escherichia coli*. *Microbiol. Rev.* 42:614-659.

Rand, R. P., and V. A. Parsegian. 1989. Hydration forces between phospholipid bilayers. *Biochim. Biophys. Acta* 988:351-376.

Roux, B. 2002. Theoretical and computational models of ion channels. *Curr. Opin. Struct. Biol.* 12:182-189.

Shrivastava, I. H., and M. S. P. Sansom. 2000. Simulations of ion permeation through a potassium channel: Molecular dynamics of KcsA in a phospholipid bilayer. *Biophys. J.* 78:557-570.

Shrivastava, I. H., D. P. Tieleman, P. C. Biggin, and M. S. P. Sansom. 2002. K^+ versus Na^+ ions in a K channel selectivity filter: A simulation study. *Biophys. J.* 83:633-645.

Smart, O. S., J. Breed, G. R. Smith, and M. S. P. Sansom. 1997. A novel method for structure-based predictions of ion channel conductance properties. *Biophys. J.* 72:1109-1126.

Spencer, R. H., G. Chang, and D. C. Rees. 1999. "Feeling the pressure": Structural insights into a gated mechanosensitive channel. *Curr. Opin. Struct. Biol.* 9:448-454.

Sukharev, S., M. Betanzos, C.-S. Chiang, and H. R. Guy. 2001a. The gating mechanism of the large mechanosensitive channel MscL. *Nature* 409:720-724.

Sukharev, S., S. R. Durell, and H. R. Guy. 2001b. Structural models of the MscL gating mechanism. *Biophys. J.* 81:917-936.

Sukharev, S. I., B. Martinac, V. Y. Arshavsky, and C. Kung. 1993. Two types of mechanosensitive channels in the *Escherichia coli* cell-envelope—Solubilization and functional reconstitution. *Biophys. J.* 65:177-183.

Sukharev, S. I., W. J. Sigurdson, C. Kung, and F. Sachs. 1999. Energetic and spatial parameters for gating of the bacterial large conductance mechanosensitive channel, MscL. *J. Gen. Physiol.* 113:525-539.

Tieleman, D. P., and H. J. C. Berendsen. 1998. A molecular dynamics study of the pores formed by *Escherichia coli* OmpF porin in a fully hydrated palmitoyloleoylphosphatidylcholine bilayer. *Biophys. J.* 74:2786-2801.

Tieleman, D. P., L. R. Forrest, M. S. P. Sansom, and H. J. C. Berendsen. 1998. Lipid properties and the orientation of aromatic residues in OmpF, influenza M2, and alamethicin systems: Molecular dynamics simulations. *Biochemistry* 37:17554-17561.

Tieleman, D. P., I. H. Shrivastava, M. R. Ulmschneider, and M. S. P. Sansom. 2001. Proline-induced hinges in transmembrane helices: Possible roles in ion channel gating. *Prot. Struct. Funct. Genet.* 44:63-72.

van Dalen, A., S. Hegger, J. A. Killian, and B. de Kruijff. 2002. Influence of lipids on membrane assembly and stability of the potassium channel KcsA. *FEBS Lett.* 525:33-38.

Vasquez-Laslop, N., H. Lee, R. Hu, and A. A. Neyfakh. 2001. Molecular sieve mechanism of selective release of cytoplasmic proteins by osmotically shocked *Escherichia coli*. *Journal of Bacteriology* 183:2399-2404.

Wilkinson, S. G. 1972. Composition and structure of ornithine-containing lipid from *Pseudomonas rubescens*. *Biochim. Biophys. Acta* 270:1-17.

Wood, J. M. 1999. Osmosensing by bacteria: Signals and membrane-based sensors. *Microbiol. and Mol. Biol. Rev.* 63:230-262.

Woolf, T. B. 1998. Molecular dynamics simulations of individual □-helices of bacteriorhodopsin in dimyristoylphosphatidylcholine. II. Interaction energy analysis. *Biophys. J.* 74:115-131.

Zhu, F., E. Tajkhorshid, and K. Schulten. 2001. Molecular dynamics study of aquaporin-1 water channel in a lipid bilayer. *FEBS Lett.* 504:212-218.

Chapter 6: Identification of the Mechanosensitive Channel of Small Conductance (MscS) Voltage Sensor

Background

The past few chapters have focused on the mechanosensitive channel of large conductance (MscL), one of three bacterial mechanosensitve channels that have been characterized electrophysiologically. The other two channels, the mechanosensitive channel of small conductance (MscS) (Martinac et al., 1987) and the mechanosensitive channel of miniture conductance (MscM) (Berrier et al., 1989) were originally noted in electrophysiological traces of *E. coli* spheroplasts. Although the gene for MscM still has not been identified, the *E. coli* gene related to MscS activity was cloned by the Booth group in 1999 (Levina et al., 1999). This yggB gene product, which has orthologues in several different bacterial species, shares relatively little sequence homology with MscL. Sequence analyses and PhoA fusion studies predicted that MscS had a more complicated topology than MscL with three transmembrane domains and a sizable C-terminal intracellular region that appears to be necessary for proper channel function (Miller et al., 2003a).

Electrophysiological measurements on MscS also showed important differences between it and MscL. First, measurements of MscS activity before its cloning implied that, in addition to being gated by membrane tension, its activity was notably modulated by changes in transmembrane potential (Martinac et al., 1987). However, this result has not been replicated in the literature after the cloning of MscL. Secondly, in contrast to the non-selective pore of MscL, MscS appears to show a slight selectivity for anions over cations (Sukharev, 2002).

Recently, a 3.9 Å resolution crystal structure of *E. coli* MscS was solved by the Rees group (Bass et al., 2002). This structure confirmed many of the earlier postulations

about the channel topology (Levina et al., 1999; Miller et al., 2003a), and showed the full channel to be a homoheptamer (Fig. 6.1). In addition to having this unique channel symmetry, the MscS structure was also interesting since it appeared to capture the channel as an open conformation instead of the closed conformation observed in the previous structures of MscL (Chang et al., 1998) and other ion channels (Doyle et al., 1998; Dutzler et al., 2002; Jiang et al., 2003a). Although there has been some debate about whether this structure is actually the open state of MscS (Anishkin and Sukharev, In press), results discussed below clearly support the assertion that it minimally represents a conductive state of the channel.

Figure 6.1: The MscS crystal structure. A) A side view of the channel showing secondary structure. Each of the seven homomeric subunits is shown in a different color. B) A top view of the channel in CPK looking from the extracellular side. As in (A), each subunit is shown in a different color. C) A single subunit of MscS with the TM1, TM2, and TM3 regions shown in red, blue, and green, respectively.

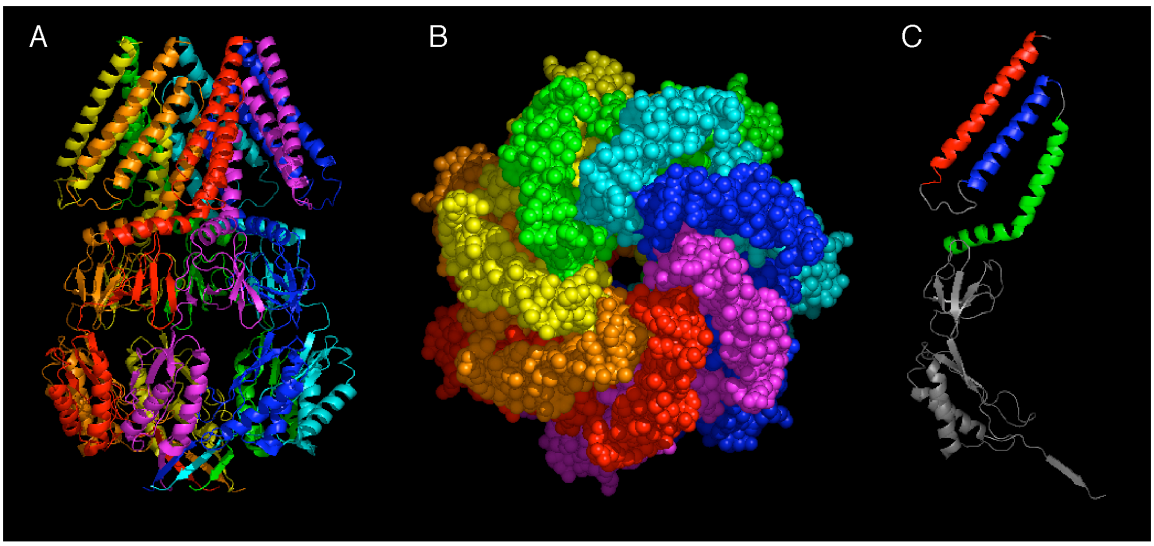

This intriguing channel structure provides the opportunity to consider interesting properties of MscS, such as its voltage sensitivity, on the molecular level. In particular, we can use molecular dynamics (MD) simulations to predict which particular amino acid residues imbue the channel with its voltage sensitivity. The crystal structure has two arginine residues, R46 and R74, in the middle of the transmembrane regions (Fig. 6.2A) that are hypothesized to contribute to the voltage sensitivity (Bass et al., 2002), but other transmembrane charged residues could also be important in this phenomenon. In light of the recent crystal structure of another channel sensitive to transmembrane potential, KvAP, these results on MscS should help refine our ideas about structural aspects of voltage sensitivity (Jiang et al., 2003a).

Setup of Molecular Dynamics Simulations

Residues Tyr 27-179 from the *E. coli* MscS crystal structure (Bass et al., 2002) were used as a starting structure for all simulations, which included all TM domains and the middle-β domain in the simulations (Fig. 6.2A). The C-terminal region after residue 179 was omitted to maintain a reasonable simulation size, although some recent results imply that region may play a role in MscS assembly and/or function (Miller et al., 2003a). All ionizable residues (Asp, Glu, Lys, and Arg; no His are present in the structure) were charged unless specifically noted otherwise, while the N- and C-termini were left uncharged as they do not represent physiological termini of the channel.

Figure 6.2: A) Crystal structure of MscS with the region included in the simulation shown in white and the region omitted in gray. Two arginines, Arg 46 and Arg 74, hypothesized to be important for voltage sensitivity are shown in blue and violet CPK, respectively. B) The embedded MscS system used for MD simulations. The protein is shown as white ribbons, with explicit lipid and water shown as green and blue wireframe, respectively. The phosphorous atoms of lipid headgroups are shown in yellow CPK.

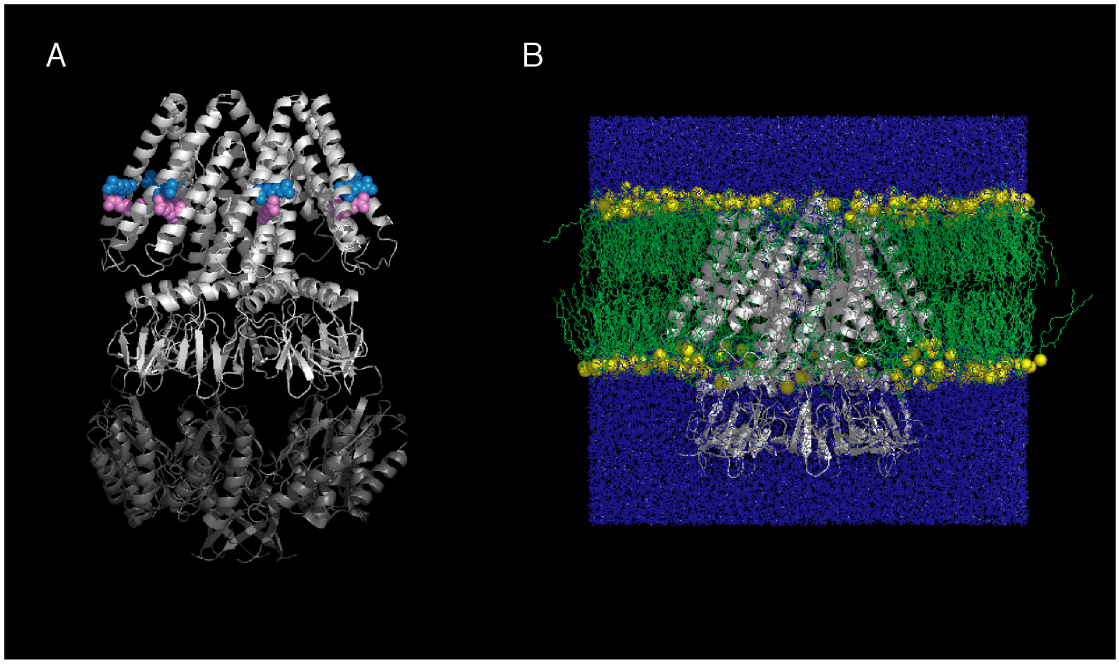

This structure was embedded into an equilibrated membrane of 512 POPE (palmitoyloleoylphosphatidylethanolamine) lipids. Throughout, the membrane was oriented in the *xy* plane, with the *z*-axis as the membrane normal. The membrane used in simulations was created by first converting a 128 POPC (palmitoyloleoyl-phosphatidylcholine) membrane created by Tieleman and co-workers (Tieleman et al., 1999) to POPE, in an analogous manner to POPE to POPC conversions described in Chapter 5. After conversion to POPE, the membrane was equilibrated for 3 ns. This equilibrated 128 POPE membrane was then copied in the *xy* plane to yield a membrane patch of 512 lipids. This enlarged membrane system was equilibrated by MD for an

additional 2 ns. The parameters described below were also used for these membrane equilibration steps.

The MscS channel was embedded into the 512 POPE membrane utilizing methods developed by Faraldo-Gómez et al. (Faraldo-Gomez et al., 2002). Briefly, lipids were removed from each leaflet of the bilayer based on the exclusion volume of the channel structure calculated using MSMS (Sanner et al., 1996); 53 total lipids were removed during this step. Then, the remaining lipids were subjected to forces based on the shape of the channel protein over three short MD simulations, forming a cavity in the membrane in the shape of MscS. These simulations were: a) a 20 ps simulation heating from 5 K to 310 K, with an outward force of 10 kJ/mol Å; b) a 20 ps simulation at 310 K with an outward force of 10 kJ/mol Å; c) a 10 ps simulation at 310 K with an outward force of 100 kJ/mol Å. The channel was then inserted into this cavity, additional waters were added to fully solvate the channel structure, and the system was subjected to 50 steps of steepest descents minimization. Afterwards, 52 Cl^- and 10 Na^+ ions were added based on the electrostatic potential of the system to neutralize the overall system charge, and four lipids which still had significant overlap with the channel were removed. This system was again minimized for 50 steps. The final system included 1071 protein residues, 455 POPE, and 28423 waters for a total of 118,665 atoms, and was about 11.6 nm x 12.2 nm x 10.9 nm. The embedded system is shown in Fig. 6.2B.

The minimized MscS system was heated to 310 K over 20 ps, with restraints on all Cα atoms of the protein structure. These restraints were maintained for an additional 180 ps of MD, after which they were gradually reduced stepwise over an additional 330 ps. This system was then used to begin three different MD simulations.

The first simulation continued the trajectory for an additional 4470 ps, for a total 5 ns of simulation. A second simulation was performed identically to the first except that a potential of 0.1 V/nm (about a 350 mV transmembrane potential) was applied normal to the membrane (in the *z*-direction) during the simulation using a method described by Tieleman, Sansom, and co-workers (Tieleman et al., 2001). This simulation was extended for 6970 ps, for a total trajectory of 7.5 ns. A third simulation was performed with two putative MscS voltage sensing residues, Arg 46 and 74, neutralized and the 0.1 V/nm potential applied throughout. Because of the change in side chain charge states, 14 waters were replaced with Cl^- ions, based on electrostatic potential, to neutralize the overall system. This simulation was extended for 4470 ps, for a total 5 ns of simulation.

All minimizations and MD simulations were performed using the GROMACS 3 suite of programs (Berendsen et al., 1995; Lindahl et al., 2001). The protocols for MD used in this study were analogous to those used in our previous simulations of the Tb-MscL channel (Elmore and Dougherty, 2001; Elmore and Dougherty, 2003). Lipid parameters were from (Berger et al., 1997), with additional parameters for the oleoyl double bond taken from the GROMOS force field. GROMACS atomic parameters were used for protein and water. All MD runs used a time step of 2 fs along with the LINCS routine to constrain bond lengths (Hess et al., 1997) and SETTLE to constrain rigid water geometries (Miyamoto and Kollman, 1992). Long-range electrostatics were computed using PME (Darden et al., 1993), with a Fourier grid spacing of 0.10 nm and cubic interpolation. A 1.0 nm cutoff was employed for Lennard-Jones and real-space Coulombic interactions. Structures from the trajectories were stored every 0.5 ps for analysis. The NPT ensemble was employed with anisotropic pressure coupling in each

direction to 1 bar with a time constant (τ_p) of 1.0 ps (Berendsen et al., 1984). Temperatures were coupled separately for protein, lipid, and solvent to a temperature bath with a coupling constant (τ) of 0.1 ps (Berendsen et al., 1984).

Analyses of trajectories were performed primarily using tools provided in the GROMACS suite, and pore radii were calculated with HOLE (Smart et al., 1997). Structural pictures were created with Pymol (DeLano, W. L., http://www.pymol.org) and Rasmol (Sayle and Milner-White, 1995).

The Channel Structure is Sensitive to Transmembrane Potential in Simulations

In general, the MscS channel is well behaved in MD simulations. As in simulations of MscL and other ion channels, the channel structure initially shows some drift from the crystal structure—as would be expected for a structure at only 3.9 Å resolution—but generally seems to equilibrate within the constraints of the simulation (Fig. 6.3). However, in the absence of any transmembrane voltage, the channel adjusts fairly rapidly to form an occlusion across the pore region through which water cannot pass (Fig. 6.4). The occlusion does not require a large conformational shift in the channel structure, but instead occurs as a few of the TM3 helices adjust in an asymmetric manner to use the L105 and L109 residues, which form the narrowest constriction in the crystal structure, to form the occlusion (Fig. 6.5). Once it appears, the occlusion remains across the pore throughout the rest of the 5 ns simulation. Since this occlusion occurs so quickly in the simulation, and these simulations are constrained to relatively short nanosecond timescales, we are hesitant to refer to this as the "closed" state of the channel. In addition, this occluded conformation does not agree fully with cross-linking data obtained

on MscS channel thought to be in the closed state (Miller et al., 2003b). Regardless, the TM motions that led to the occlusion provide an intriguing starting point for thinking about channel closure as a potentially asymmetric process, and the rapid collapse of the channel into an occluded state shows the instability of the crystal structure conformation in the absence of some applied stimulus, such as a transmembrane potential.

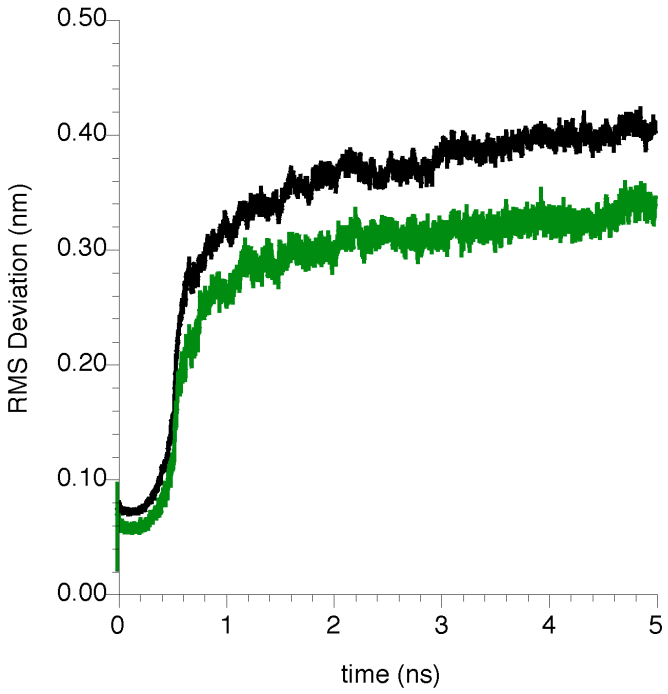

Figure 6.3: RMS deviation from crystal structure in the MscS simulation with no applied voltage. These values were calculated for all Cα in the protein (black) or just Cα in the pore-lining TM3 domain (green) for each frame of the simulation by first fitting all protein Cα to the crystal structure.

Since MscS is thought to be a voltage-sensitive channel, we performed a simulation in which a 0.1 V/nm voltage was applied across the simulation box. This corresponds to a 300-400 mV transmembrane potential, which although higher than that typically observed in living cells is in the range used in previous simulations (Robertson and Tieleman, 2002; Tieleman et al., 2001) and would be feasible for electrophysiological studies. In particular, simulations performed by Tieleman and co-

workers have shown that the membrane models used here are stable under this magnitude of applied voltage.

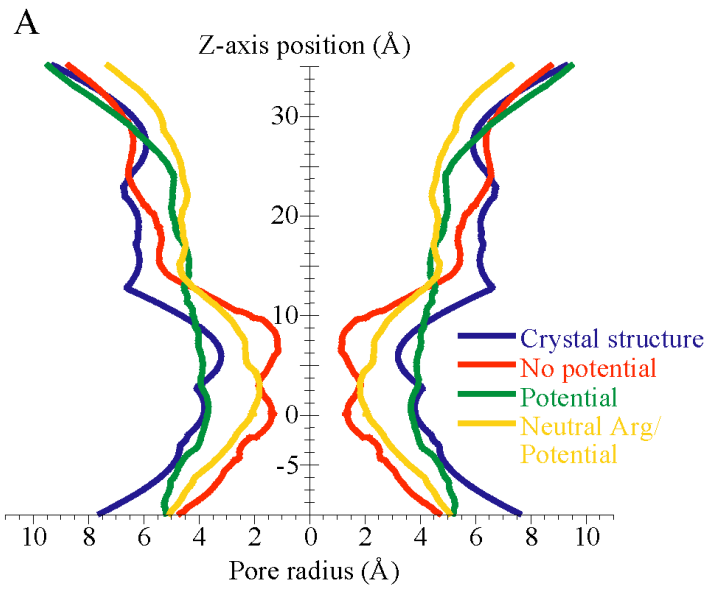

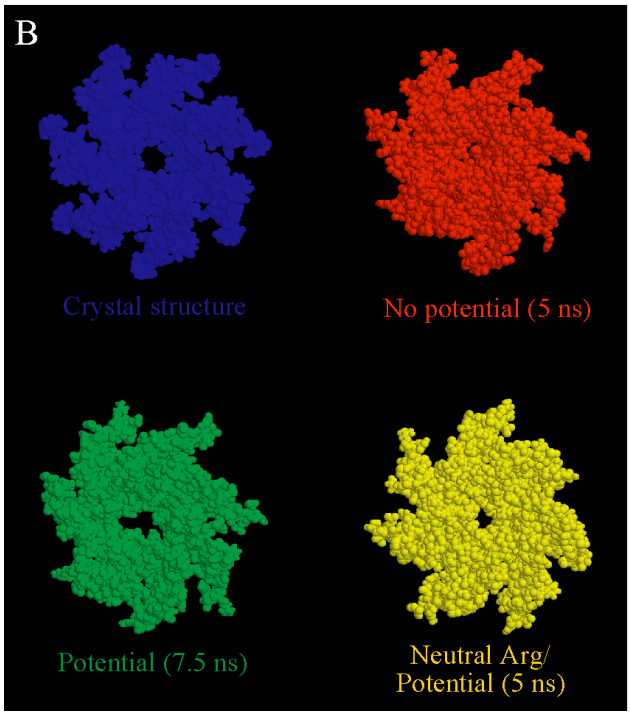

Figure 6.4: A) Plot showing the radius along the MscS pore calculated using HOLE. Radii for simulations were averaged over frames taken every 50 ps over the final 250 ps of each trajectory. The Z-axis position refers to position along the membrane normal, with 0 set at the position of L109. B) CPK pictures of the MscS crystal structure and the final frame of different trajectories. Each picture is oriented looking from the extracellular side of the channel and includes only TM residues for clarity.

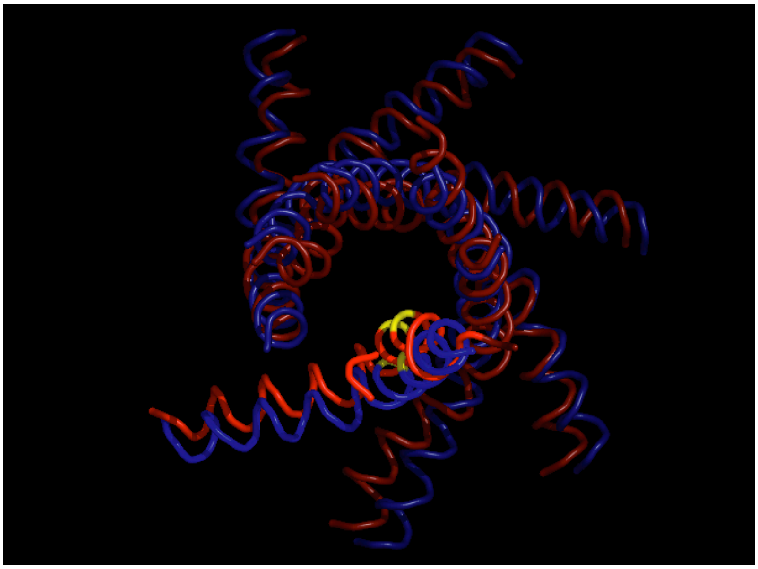

Figure 6.5: Superimposed TM3 regions from the crystal structure (blue) and the 5 ns frame of the simulation with no applied voltage (red). The subunit in brighter colors was one that moved such that the L105 and L109 (shown in yellow) residues occluded the channel. The TM3 of one subunit is omitted for clarity.

Interestingly, the channel does *not* relax into the occluded state in this simulation with an applied voltage (Fig. 6.4). In fact, the channel never becomes more occluded than the crystal structure throughout a 7.5 ns trajectory. It appears that the non-occluded conformation seen in the crystal structure is stabilized by applied voltage, while that conformation is unstable if such a voltage is not applied. Thus, the channel structure is clearly sensitive to transmembrane potentials.

Remarkably, the occluded channel from the simulation can also be "reopened" by an applied voltage. When the 5 ns occluded final frame from the simulation with no voltage applied was subjected to a potential of 0.33 V/nm across the box, the occlusion was removed from the channel. Interestingly, this "reopening" did not occur within a few ns when the channel was only subjected to the 0.1 V/nm voltage used to maintain the non-occluded state.

Does the Crystal Structure Represent an "Open" State?

As mentioned earlier, there has been some debate about whether or not the MscS crystal structure represents an open state of the ion channel. Initially, Bass et al. felt that the relatively wide diameter of the MscS pore in the structure (≈ 11 Å at its narrowest point) implied the structure was in the open state (2002). However, recent MD simulations by Anishkin and Sukharev (in press) have implied that the most constricted region of the crystal structure pore is so hydrophobic that it would expel water and induce a "vapor-lock" that effectively blocks the channel to ion passage.

Our MD simulations show that this pore "dewetting" behavior is likely an artifact of a simulation that was not allowed to equilibrate fully (Anishkin and Sukharev, In press). In order to increase computational efficiency, Anishkin and Sukharev included only fragments of the MscS TM regions in their simulations. Thus, in order to maintain a reasonable conformation, they placed restraints on the backbones of the TM regions. In their trajectory, water is rapidly expelled from the most constricted region of the pore and generally does not reenter during the remainder of a 6 ns simulation.

We also observe a similar "dewetting" phenomenon in the initial *nonequilibrated* portion of our MD simulations in which the channel is subjected to restraints. During this early portion of the trajectory, the majority of water molecules leave the constricted region of the pore, and in some frames, such as at 250 ps (Fig. 6.6A), there is a clear region devoid of water. However, in the voltage applied simulation where the channel does not become occluded, water rapidly reenters the pore after the restraints are fully released from the system, and there is a clear column of water through the channel that remains throughout the full 7.5 ns simulation (Fig. 6.6B and C). In fact, many ions pass

through this region of the pore over the course of the trajectory. Thus, in our *equilibrated* system there is no evidence that the channel pore is blocked to the passage of ions by a region devoid of water.

Figure 6.6: Pictures of the 250 ps (A), 2 ns (B), and 7.5 ns (C) frames from the simulation with 0.1 V/nm potential applied (no potential was applied yet at 250 ps).

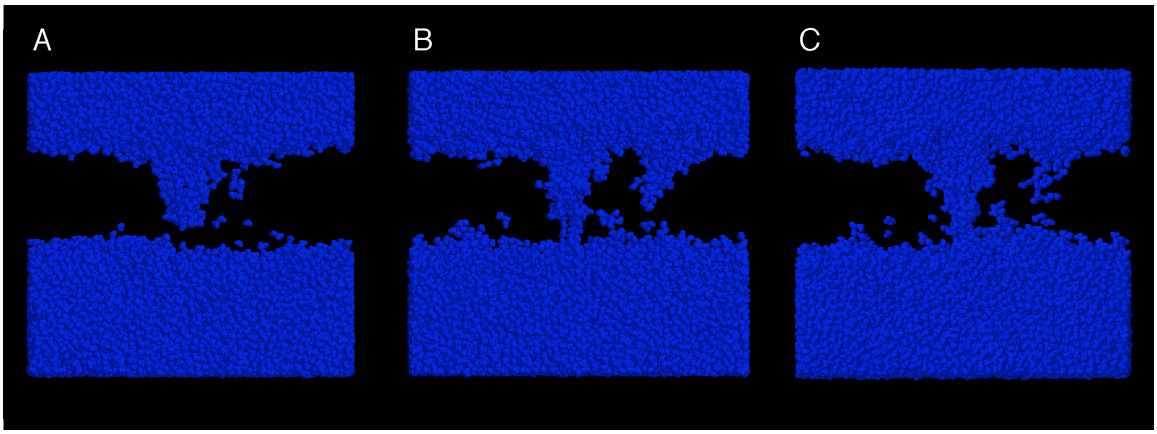

This might lead one to wonder whether the pore region conformation of the channel changes significantly in our simulation to allow the reentry of water. The most notable change upon the release of restraints is a break of symmetry in the pore region (Fig. 6.7 A). In breaking this symmetry, the TM3 helices are able to present a somewhat less hydrophobic face to the pore, promoting the reentry of water into the pore. In addition, some of the polar side chains of Q112 residues move up towards the L105/L109 constriction as the simulation progresses, further stabilizing water in the region (Fig. 6.7B). However, these conformational changes are relatively minor. The experimental structure was only solved to 3.9 Å resolution, and the RMS deviation of all TM3 atoms from the crystal structure is just about 3 Å at the point in the trajectory where water

reenters the pore, and it hits a maximum of about 4 Å throughout the 7.5 ns trajectory. As well, the perfect heptameric symmetry imposed during the solving of the crystal structure would almost certainly not exist at any moment in time in a physiological system. In general, it seems very reasonable from an energetic standpoint that the channel protein would experience these relatively conservative changes to eliminate an effective vacuum within the pore.

Interestingly, an ongoing collaboration between the Roux group and ourselves using Brownian Dynamics simulations and electrostatic calculations (Im et al., 2000) to predict MscS conductance based on the crystal structure implies that the crystal structure represents a conductive state of the channel (unpublished data). These predictions are still preliminary, and it is unclear from them whether the structure actually represents a *conductive* intermediate state or the fully open state of the channel. However, these models clearly do not imply that the MscS crystal structure represents a non-conductive state of the channel. Thus, throughout the rest of this chapter the conformation of MscS in simulations with an applied voltage will be referred to as the "conductive" state.

Figure 6.7: Top (A) and side (B) views of TM3 regions from the 250 ps (left) and 2 ns (right) frames from an MscS trajectory. The 2 ns frame is taken from a trajectory with 0.1 V/nm voltage applied to the system. L105 and L109 are shown in yellow CPK, and Q112 is shown in blue CPK.

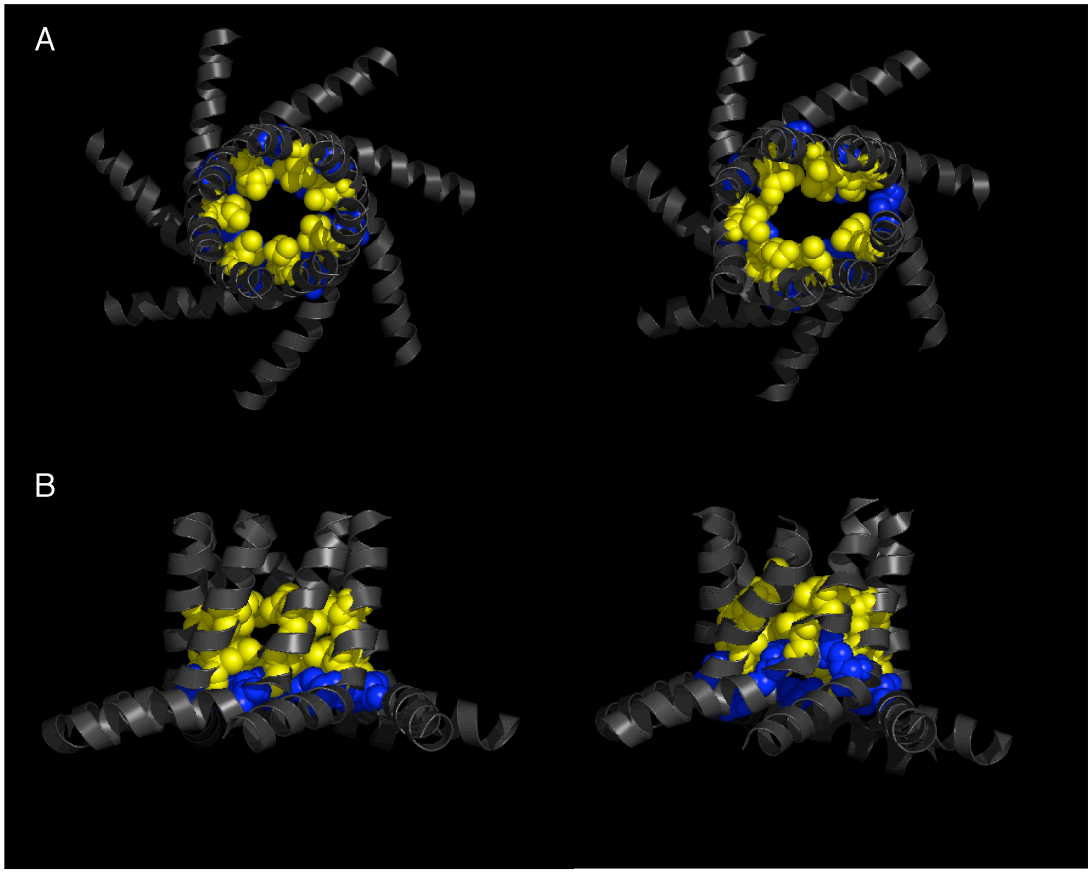

What Chemical Moieties Give the Channel Its Voltage Sensitivity?

The conventional model of voltage sensitivity implies that a voltage-sensitive channel has charged residues that move through the transmembrane region—and thus the transmembrane potential field—as the channel progresses from its open to closed conformations (Hille, 2001). We observed this type of behavior in the MD simulation in which MscS moves from its conductive conformation to the occluded conformation. In

particular, we initially noted that the two arginines originally considered to be voltage sensor residues, R46 and R74, dropped significantly towards the intracellular side of the membrane in the occluded trajectory (Fig. 6.8). Conversely, these residues maintained their relative transmembrane position throughout the simulation with an applied voltage.

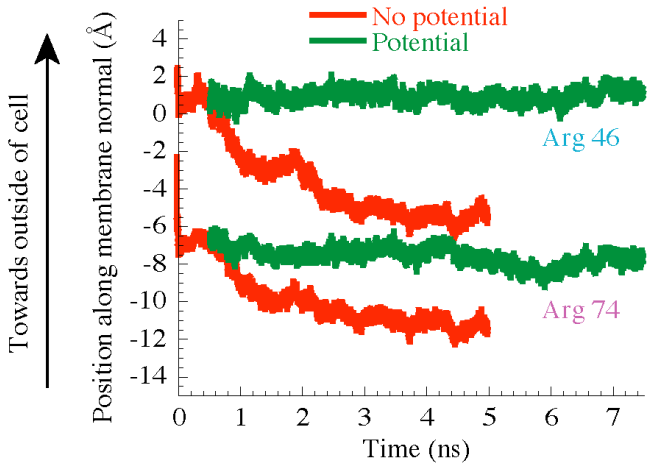

Figure 6.8: Position of R46 and R74 residues in simulations with and without applied potential. Positions were taken as the position of the □-carbon of the arginine residue, which is the charge center of the side chain. The zero position on the membrane normal is set at the center of the membrane.

These results implied that those residues might be important in providing MscS with its voltage sensitivity. To test this assertion, we performed an additional simulation of MscS in which R46 and R74 were changed to their neutral form. In this simulation, the channel became quite occluded even in the presence of the 0.1 V/nm potential field that maintains the wild-type channel in its conductive state (Fig. 6.4). Interestingly, the channel did not become fully occluded to the extent seen in the simulation without an applied voltage over this 5 ns simulation. Thus, it appeared that while R46 and R74 provide the channel with most of its voltage sensitivity, other residues that are still charged in this simulation also may play a role in sensing transmembrane potentials. As expected, a simulation of MscS with R46 and R74 neutralized that did not have an applied potential rapidly progressed towards the fully occluded state.

Another simulation with an R46A mutation and an applied 0.1 V/nm potential also was performed to further confirm this result (S. A. Spronk, unpublished results). This simulation is more directly comparable to conventional experimental mutagenesis of the channel converting an arginine residue to an alanine. R46 was chosen as the initial target over R74 since it showed a larger movement in the non-voltage applied simulation (Fig. 6.8), implying that it is likely more important for voltage sensitivity. The results of the R46A simulation were qualitatively identical to those of the neutralized R46/R74 simulation (data not shown).

Table 6.1: Positions and relative movement along the membrane normal (*z*-axis) of charged TM residues in MscS trajectories with (conductive state) and without (occluded state) 0.1 V/nm applied potential. Positions are averaged over the final 1 ns of each trajectory and expressed such that zero is the membrane center and increasingly positive positions are towards the periplasmic side of the membrane. Relative changes are expressed such that positive values represent movement towards the cytoplasmic side in the simulation without applied potential.

Residue	Position in Trajectory with Applied Potential	Position in Trajectory without Applied Potential	Relative Change in Position Towards Cytoplasmic Side
R46	1.2 Å	-5.5 Å	6.7 Å
R54	-11.4 Å	-14.5 Å	3.1 Å
D67	-12.6 Å	-15.5 Å	2.9 Å
R74	-7.8 Å	-11.3 Å	3.5 Å
R88	11.1 Å	7.5 Å	3.6 Å

However, both the neutralized R46/R74 and R46A simulations do not show complete channel occlusion, implying that other charged residues in the transmembrane region may contribute to the voltage sensitivity of MscS. In fact, other charged residues show movement equivalent to that of R74 as the channel progresses from the conductive

to occluded states (Table 6.1). This includes two other positively charged arginines (R54 and R88) and one negatively charged aspartate (D67) that move towards the intracellular region. Thus, R54 and R88 would help promote voltage sensitivity, while D67 would actually oppose it. Together with R46 and R74, the motion of these residues implies that the transition between the conductive and occluded states would involve a motion of : 7 * (6.7 + 3.1 – 2.9 + 3.5 + 3.6) = 98 charge•Å. Assuming a membrane thickness of 35 Å, this corresponds to 2.8 charges moving across the membrane during the transition.

Agreement with Experimental Electrophysiology

Preliminary electrophysiological results on wild-type and R46A MscS expressed in *E. coli* spheroplasts generally agree with the predictions from MD simulations described above (L. W. Lee, unpublished data). Wild-type MscS does show voltage modulation, with an e-fold change in its open probability for every 6.44 mV of transmembrane potential at a constant applied tension. This is a somewhat greater voltage sensitivity than the previously observed e-fold increase in open probability for every 15 mV of transmembrane potential (Martinac et al., 1987). These experimentally measured voltage sensitivities can be compared to the 2.8 charge equivalents moving across the membrane as the channel transitions between the conductive and occluded states found in MD simulations. The e-fold increase for 15 mV would imply the motion of 1.6 charges across the membrane, while the e-fold increase for 6.44 mV implies a motion of 3.7 charges across the membrane. Although the movement of 2.8 charges across the membrane in our simulations is between these two numbers, it does imply that previous studies may have underestimated the voltage sensitivity of the channel.

As well, the R46A channel shows essentially no sensitivity to transmembrane potential in electrophysiological measurements, again supporting its predicted importance in providing a significant portion of the channel's voltage sensitivity. Unfortunately, attempts to experimentally characterize an R74A mutant have been hampered by the apparently poor expression of that channel in *E. coli* spheroplasts, but future attempts to characterize the sterically subtler but still uncharged R74Q mutant will hopefully provide interesting results.

Discussion

Molecular dynamics simulations have proven to be a very useful tool to structurally consider the voltage modulation of MscS, predicting specific amino acid residues that give the channel its voltage sensitivity. In particular, it appears that R46 is a central residue for giving the channel its ability to respond to transmembrane potentials. However, the MD simulations also imply that other charged residues in the MscS TM regions may be important in voltage sensing mechanisms, and additional simulations and experimental characterizations of MscS mutants can further investigate these possibilities.

The voltage sensing in MscS has both interesting similarities and differences to the voltage sensing "paddle" proposed for KvAP (Jiang et al., 2003a; Jiang et al., 2003b). Like the voltage paddle, many of the MscS residues that appear to respond to transmembrane potential, particularly R46, face the lipid membrane. However, the voltage sensing regions move much less dramatically in MscS, although this may be partially due to its lower sensitivity to voltage. Also, if other charged residues, such as

R88, do play a significant role in MscS voltage sensitivity, then the voltage sensing residues are also less concentrated in a single substructure in MscS.

Future investigations on MscS should probe in more detail how force is transduced between the MscS TM regions in order to couple the motion of the TM1 and TM2 regions that contain the voltage sensing residues—and also would directly sense tension applied through the membrane—and the pore-lining TM3 region. In particular, MD simulations could be used to calculate interaction energies between residues in the TM regions, and the importance of residues with significant interactions could then be probed by experimental mutagenesis. These mutants could be characterized by electrophysiology, but it might be more efficient to characterize a larger set of mutations by adapting the high-throughput assay used to characterize MscL mutants (Maurer and Dougherty, 2001) to MscS. The high-throughput assay should be appropriate for MscS since Miller et al. (2003) were able to characterize MscS mutants using standard growth-based assays. This approach combining interaction energies from MD simulations and experimental mutagenic analyses is similar to that described in Chapter 5 and in (Elmore and Dougherty, 2003) for determining that lipid-interacting residues are more important than intersubunit interactions for MscL function. In addition, since MscS is a mechanosensitive channel like MscL, it would also be interesting to determine whether its residues that interact strongly with lipid are also critical for proper channel function.

It would also be valuable to focus on the potential role of the extensive intracellular C-terminal domains of MscS. Even minor cleavages in the C-terminal region lead to a channel that cannot effectively rescue bacteria from osmotic downshock (Miller et al., 2003a). Although it is unclear whether this dramatic loss of channel

function results from improper channel assembly or a properly assembled but non-functional channel, it is clear that even the most distal portion of the intracellular domain plays some critical role in MscS structure or function. Other work has shown that the intracellular domains of the channel appear to rearrange their conformation upon channel gating, since binding of a C-terminal hexa-histidine tag to metal ions prevents closed channels from opening (Koprowski and Kubalski, 2003). Thus, future simulations should aim to include this full region from the crystal structure.

References

Anishkin, A., and S. Sukharev. In press. Water dynamics and dewetting transitions in the small mechanosensitive channel MscS. *Biophys. J.*

Bass, R. B., P. Strop, M. Barclay, and D. C. Rees. 2002. Crystal structure of *Escherichia coli* MscS, a voltage-modulated and mechanosensitive channel. *Science* 298:1582-7.

Berendsen, H. J. C., J. P. M. Postma, W. F. van Gunsteren, A. DiNola, and J. R. Haak. 1984. Molecular dynamics with coupling to an external bath. *J. Chem. Phys.* 81:3684-3690.

Berendsen, H. J. C., D. van der Spoel, and R. van Drunen. 1995. GROMACS: A message-passing parallel molecular dynamics implementation. *Comp. Phys. Comm.* 91:43-56.

Berger, O., O. Edholm, and F. Jähnig. 1997. Molecular dynamics simulations of a fluid bilayer of dipalmitoylphosphatidylcholine at full hydration, constant pressure, and constant temperature. *Biophys. J.* 72:2002-2013.

Berrier, C., A. Coulombe, C. Houssin, and A. Ghazi. 1989. A patch-clamp study of ion channels of inner and outer membranes and of contact zones of *E. coli*, fused into giant liposomes. Pressure-activated channels are located in the inner membrane. *FEBS Lett.* 259:27-32.

Chang, G., R. H. Spencer, A. T. Lee, M. T. Barclay, and D. C. Rees. 1998. Structure of the MscL homolog from *Mycobacterium tuberculosis*: a gated mechanosensitive ion channel. *Science* 282:2220-6.

Darden, T. D., D. York, and L. Pedersen. 1993. Particle mesh Ewald: An N log(N) method for Ewald sums in large systems. *J. Chem. Phys.* 98:10089-10092.

Doyle, D. A., J. Morais Cabral, R. A. Pfuetzner, A. Kuo, J. M. Gulbis, S. L. Cohen, B. T. Chait, and R. MacKinnon. 1998. The structure of the potassium channel: molecular basis of K^+ conduction and selectivity. *Science* 280:69-77.

Dutzler, R., E. B. Campbell, M. Cadene, B. T. Chait, and R. MacKinnon. 2002. X-ray structure of a ClC chloride channel at 3.0 A reveals the molecular basis of anion selectivity. *Nature* 415:287-94.

Elmore, D. E., and D. A. Dougherty. 2001. Molecular dynamics simulations of wild-type and mutant forms of the *Mycobacterium tuberculosis* MscL channel. *Biophys. J.* 81:1345-1359.

Elmore, D. E., and D. A. Dougherty. 2003. Investigating lipid composition effects on the mechanosensitive channel of large conductance (MscL) using molecular dynamics simulations. *Biophys. J.* 85:1512-1524.

Faraldo-Gomez, J. D., G. R. Smith, and M. S. Sansom. 2002. Setting up and optimization of membrane protein simulations. *Eur Biophys J* 31:217-27.

Hess, B., H. Bekker, H. J. C. Berendsen, and J. G. E. M. Fraaije. 1997. LINCS: A linear constraint solver for molecular simulations. *J. Comp. Chem.* 18:1463-1472.

Hille, B. 2001. *Ion Channels of Excitable Membranes.* Sunderland, CT: Sinauer Associates.

Im, W., S. Seefeld, and B. Roux. 2000. A Grand Canonical Monte Carlo-Brownian dynamics algorithm for simulating ion channels. *Biophys. J.* 79:788-801.

Jiang, Y., A. Lee, J. Chen, V. Ruta, M. Cadene, B. T. Chait, and R. MacKinnon. 2003a. X-ray structure of a voltage-dependent K^+ channel. *Nature* 423:33-41.

Jiang, Y., V. Ruta, J. Chen, A. Lee, and R. MacKinnon. 2003b. The principle of gating charge movement in a voltage-dependent K^+ channel. *Nature* 423:42-48.

Koprowski, P., and A. Kubalski. 2003. C termini of the *Escherichia coli* mechanosensitive ion channel (MscS) move apart upon the channel opening. *J. Biol. Chem.* 278:11237-11245.

Levina, N., S. Tötemeyer, N. R. Stokes, P. Louis, M. A. Jones, and I. R. Booth. 1999. Protection of *Escherichia coli* cells against extreme turgor by activation of MscS and MscL mechanosensitive channels: Identification of genes required for MscS activity. *EMBO J.* 18:1730-1737.

Lindahl, E., B. Hess, and D. van der Spoel. 2001. GROMACS 3.0: A package for molecular simulation and trajectory analysis. *J. Mol. Mod.* 7:306-317.

Martinac, B., M. Buechner, A. Delcour, J. Adler, and C. Kung. 1987. Pressure-sensitive ion channel in *Escherichia coli*. *Proc. Natl. Acad. Sci. USA* 84:2297-2301.

Maurer, J. A., and D. A. Dougherty. 2001. A high-throughput screen for MscL channel activity and mutational phenotyping. *Biochim. Biophys. Acta* 1514:165-9.

Miller, S., W. Bartlett, S. Chandrasekaran, S. Simpson, M. Edwards, and I. R. Booth. 2003a. Domain organization of the MscS mechanosensitive channel of *Escherichia coli*. *EMBO J.* 22:36-46.

Miller, S., M. D. Edwards, C. Ozdemir, and I. R. Booth. 2003b. The closed structure of the MscS mechanosensitive channel. Cross-linking of single cysteine mutants. *J Biol Chem* 278:32246-50.

Miyamoto, S., and P. A. Kollman. 1992. SETTLE: An analytical version of the SHAKE and RATTLE algorithms for rigid water models. *J. Comp. Chem.* 13:952-962.

Robertson, K. M., and D. P. Tieleman. 2002. The molecular basis of voltage gating of OmpF porin. *Biochem. Cell Biol.* 80:517-523.

Sanner, M. F., J.-C. Spehner, and A. J. Olson. 1996. Reduced surface: An efficeint way to computer molecular surfaces. *Biopolymers* 38:305-320.

Sayle, R., and E. J. Milner-White. 1995. RasMol: Biomolecular graphics for all. *TIBS* 20:374-376.

Smart, O. S., J. Breed, G. R. Smith, and M. S. P. Sansom. 1997. A novel method for structure-based predictions of ion channel conductance properties. *Biophys. J.* 72:1109-1126.

Sukharev, S. 2002. Purification of the small mechanosensitive channel of *Escherichia coli* (MscS): the subunit structure, conduction, and gating characteristics in liposomes. *Biophys. J.* 83:290-8.

Tieleman, D. P., H. J. C. Berendsen, and M. S. P. Sansom. 2001. Voltage-dependent insertion of a channel forming peptide: Molecular dynamics simulations of alamethicin at phospholipid-water and octane/water interfaces. *Biophys. J.* 80:331-346.

Tieleman, D. P., M. S. P. Sansom, and H. J. C. Berendsen. 1999. Alamethicin helices in a bilayer and in solution: Molecular dynamics simulations. *Biophys. J.* 76:40-49.

Chapter 7: Computational Determination of Nicotine Conformations in the Gas Phase and in Aqueous Solution

Background

Nicotine (Fig. 7.1) is a major drug of abuse that acts as a potent agonist of the nicotinic acetylcholine receptor (nAChR). Related nicotinic species have been proposed as treatments for conditions ranging from cognitive and attention deficits to Parkinson's disease to smoking cessation (Bannon et al., 1998; Eglen et al., 1999; Holladay et al., 1997). A thorough understanding of the geometric and electronic structure of nicotine would aid efforts to elucidate receptor structure-function relationships and design new pharmaceuticals. Several early experimental and theoretical studies investigated the relative stabilities of different nicotine conformers (Barlow et al., 1986; Berthelot et al., 1991; Chynoweth et al., 1973; Cox et al., 1986; Hacksell and Mellin, 1989; Kier, 1968; Koo and Kim, 1965; Pitner et al., 1978; Pullman et al., 1971; Radna et al., 1973; Seeman, 1984; Whidby et al., 1979; Whidby and Seeman, 1976). Much of this work focused on three conformational aspects of nicotine: the position of the N8-methyl substituent relative to the pyridine ring (*cis* or *trans*); the relative orientation of the two rings; and the conformation of the pyrrolidine ring. Crystal structures of both the monoprotonated and diprotonated forms of nicotine as iodide salts show the two rings nearly perpendicular to one another and a *trans* N8 group (Barlow et al., 1986; Koo and Kim, 1965). However, these crystal structures do not give direct insight into relative conformer populations present in solution. Moreover, these crystals were grown from ethanol, in which nicotine might adopt a different conformation than in water. NMR studies have probed nicotine solution phase conformations (Chynoweth et al., 1973; Cox et al., 1986; Pitner et al., 1978; Seeman, 1984; Whidby et al., 1979; Whidby and Seeman, 1976). Early NOE work proposed a *cis* N8-methyl group (Chynoweth et al., 1973), but Whidby and Seeman

refuted this conclusion estimating an approximately 10:1 *trans*/*cis* equilibrium ratio for nicotine (Whidby and Seeman, 1976). This latter study was conducted at very low pH to suppress N8-inversion and therefore involved direct characterization of the diprotonated form, making conclusions about the physiologically relevant monoprotonated species necessarily indirect. Further NMR structural studies proposed that the pyridine and pyrrolidine rings are approximately perpendicular to one another and that the pyrrolidine ring adopts an envelope conformation with N8 out of plane (Pitner et al., 1978). However, these NMR studies were performed in a $CDCl_3/CFCl_3$ solvent mixture, which could lead to different conformational stabilities than aqueous solvent.

Figure 7.1: Nicotine protonation states and numbering of nicotine used in this chapter.

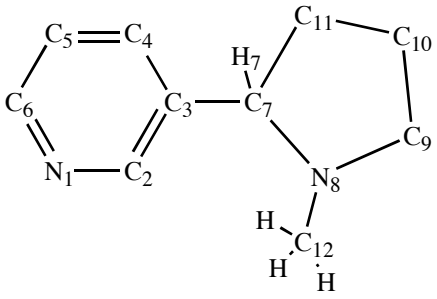

neutral (**0**)

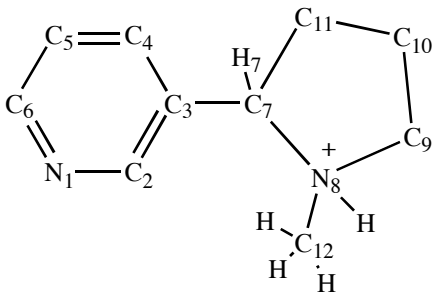

singly protonated (**+**)

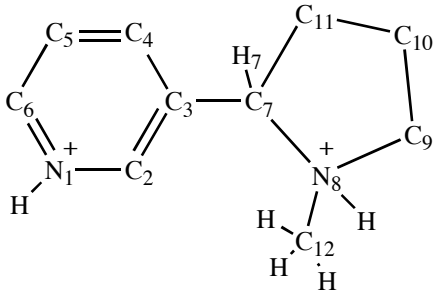

doubly protonated (**++**)

Previous computational studies of nicotine conformation employed PCILO (Pullman et al., 1971), molecular mechanics (Hacksell and Mellin, 1989), INDO (Radna et al., 1973; Seeman, 1984), AM1 (Berthelot et al., 1991), and extended Hückel (Kier, 1968) methods. These studies generally produced low energy conformers similar to those found experimentally, with the N8-methyl group *trans* and the two rings approximately perpendicular to one another. All of these calculations involved levels of theory well below the current state of the art and were conducted in the gas phase, ignoring possible effects arising from interactions with water. Recently, more modern computational techniques have been used to study the conformations of other nAChR ligands: ACh (Edvardsen and Dahl, 1991; Margheritis and Corongiu, 1988; Segall et al., 1998), epibatidene (Campillo et al., 1998), and anatoxin-a (Thompson et al., 1992), and it seemed appropriate to perform a contemporary study on nicotine. This was done by using a combination of quantum mechanical gas-phase methods and two very different solvation models. One model used explicit TIP4P (Jorgensen et al., 1983) water with the OPLS force field (Jorgensen et al., 1996) developed and applied by Jorgensen along with Monte Carlo (MC) statistical perturbation theory (SPT) methods (Jorgensen, 1989). SPT/OPLS methods have been used to calculate solvent effects for a variety of chemical systems, including heterocycles similar to nicotine, such as histamine, imidazone, and nicotinic and isonicotinic acids (Nagy and Durant, 1996; Nagy et al., 1994; Nagy et al., 1993; Nagy and Takács-Novák, 1997). The second solvation model applied is a recently developed quantum mechanical continuum method, SM5.42R (Li et al., 1998; Zhu et al., 1998), which has been parameterized for a number of HF and DFT methods. It has

produced good results for a wide range of solutes, including N-containing species which are sometimes problematic for solvation methods.

Energetic Profile for Relative Pyridine/Pyrrolidine Ring Rotations

Rotation around the C3-C7 bond was investigated using molecular mechanics (MMFF94) and semiempirical (AM1) methods implemented in SPARTAN 5.0. This was done for all nicotine protonation states (Fig. 7.1), which will be referred to as **0** (unprotonated), **+** (singly protonated), **++** (doubly protonated). The rotational profiles were performed by freezing the H7-C7-C1-C2 dihedral angle at approximately 5° intervals and optimizing the remainder of the structure. All profiles were generally like the **+** MMFF94 profiles shown in Fig. 7.2 with two minima. These rotamers, labeled **A** and **B**, have dihedral angles close to 0° and 180°, respectively, which place the pyridine and pyrrolidine rings roughly perpendicular to one another as seen in previous work (Hacksell and Mellin, 1989; Kier, 1968; Pitner et al., 1978; Pullman et al., 1971). Rotational barriers between **A** and **B** are consistently higher for the *cis* species (6-8 kcal/mol versus about 3 kcal/mol for *trans*), which is consistent with increased steric interactions between the N8-methyl group and the pyridine ring in that species. Nonetheless, these barriers are low enough to generally allow rapid rotation between the **A** and **B** species.

Figure 7.2: MMFF94 rotational profile for singly protonated (+) nicotine species**.**

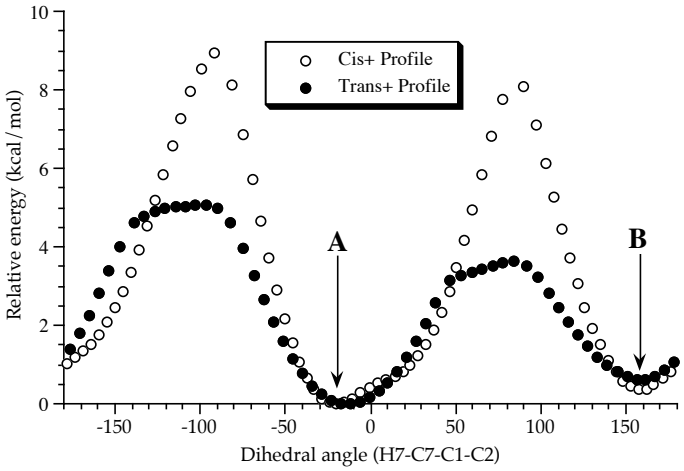

Gas-Phase Structures and Energetics

Gas-phase optimized structures were therefore calculated for the **A** and **B** rotamers of each protonation state at the HF/6-31G** level; HF/6-31G** frequency calcualtions were used to verify these were true minima. All *ab initio* calculations were performed with the Gaussian 94 suite (Frisch et al., 1995). Although the major contributors in aqueous solution may not all be gas-phase minima (Colominas et al., 1999), this seems unlikely in the present system that has relatively few degrees of conformational freedom. Pictures of the optimized **+** species can be seen in Fig. 7.3, and selected geometrical quantities for all structures are given in Table 7.1. The rings remain relatively perpindicular in these optimizations. The intramolecular N3-N8 distances are longer for **A** rotamers; this trend is more pronounced in *trans* than *cis* species. These differences might be related to differences in solvation discussed below. As well, the N-N distance increases between **+** and **++** species, as observed in crystal structures (Barlow

et al., 1986; Koo and Kim, 1965), apparently as two positively charged centers repel each other.

Table 7.1: Selected geometric attributes of nicotine species optimized at HF/6-31G**.[a]

Species	N1-N8	H7-C7-C3-C2	C7-N8-C9-C10	N8-C9-C10-C11	C9-C10-C11-C7
***cis*+ A**	4.582	-19.0	37.3	-18.5	-6.7
***cis*+ B**	4.529	159.8	37.4	-18.8	-6.2
***trans*+A**	4.655	-5.9	-25.7	1.3	23.3
***trans*+ B**	4.385	178.0	-27.7	4.0	21.0
***cis* A**	4.633	-18.9	36.8	-16.9	-6.9
***cis* B**	4.537	160.6	37.2	-17.4	-6.4
***trans* A**	4.793	16.5	-42.3	25.7	-1.4
***trans* B**	4.247	-164.7	-42.3	25.6	-1.2
***cis*++ A**	4.749	-5.6	26.4	-41.0	40.5
***cis*++ B**	4.708	140.7	-4.4	-22.3	40.5
***trans*++ A**	4.737	1.7	-30.7	7.6	17.8
***trans*++ B**	4.546	162.6	-24.0	-1.5	26.0

[a]Distances are in Å and angles are in degrees; pyrrolidine dihedral angles are given to the right of the bold line.

Pyrrolidine ring conformation was ambiguous in previous work. NMR studies on nicotine and closely related compounds have implied that the ring has an envelope conformation with the N8 atom out of plane in nonaqueous solution where the **0** species would have been present (Pitner et al., 1978; Seeman, 1984; Whidby et al., 1979). Conversely, the **+** and **++** crystal structures show species with more twisted conformations (Barlow et al., 1986; Koo and Kim, 1965). To address this, several ring conformations were explored with AM1 and HF/6-31G** calculations, leading to the most stable conformers shown in Fig. 7.3 and Table 7.2. The *trans***0** pyrrolidine has an envelope conformation analogous to NMR results. However, the *trans***+** and *trans***++** species alter their envelope conformation to place the C7 atom out of plane, which is

different than in crystal structures (Barlow et al., 1986; Koo and Kim, 1965). All *cis***0** and *cis***+** structures have similar envelope conformations, with the N8-atom out of plane, although the rest of the ring is less planar than in *trans***0** conformers. Doubly protonated *cis***++ A** and **B** structures show different conformations than other protonation states, with C10 and C11 out of plane, respectively.

Figure 7.3: HF/6-31G** optimized structures of singly protonated nicotine species. Key: Black: carbon, Grey: nitrogen, White: hydrogen.

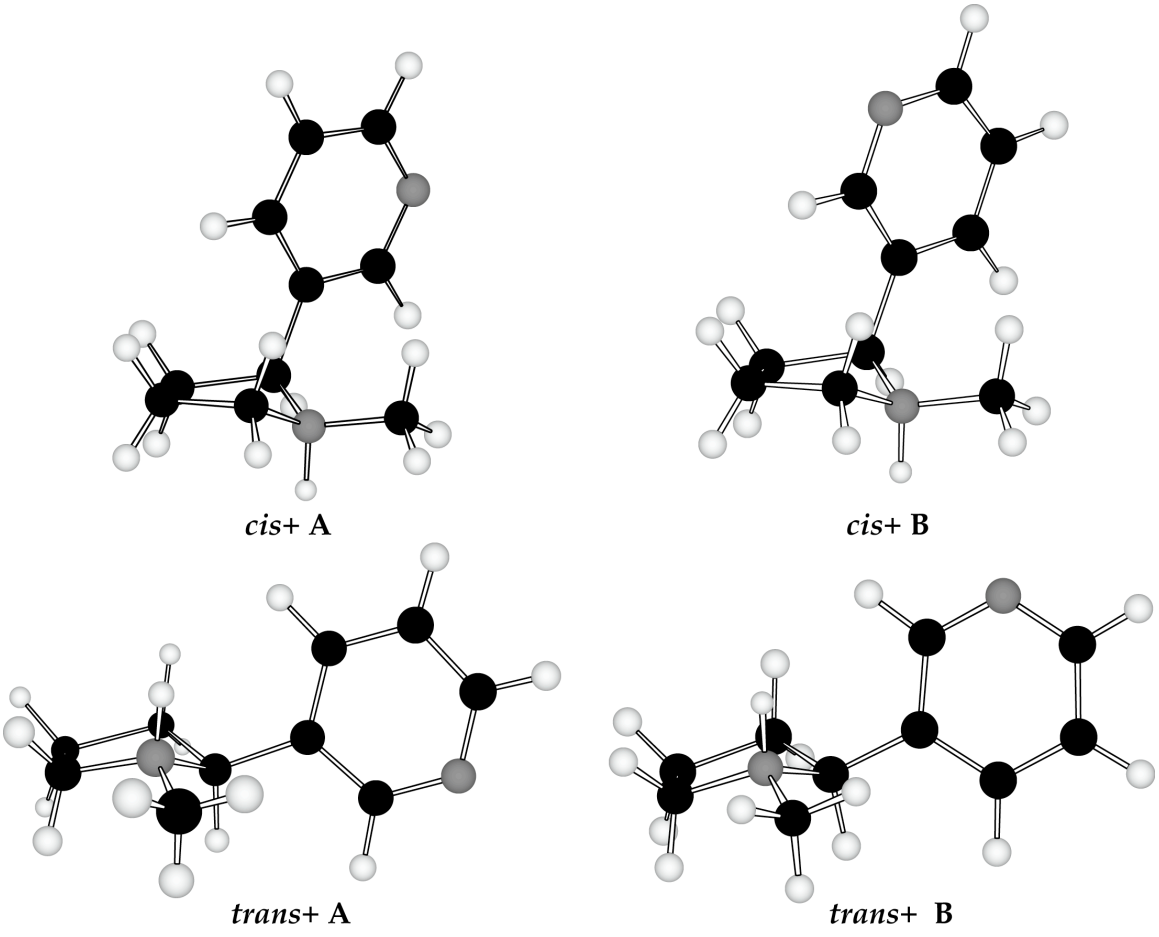

Energetic comparisons of the conformers were done using MP2/6-31G** and B3LYP/6-31G** single point calculations on the optimized HF/6-31G** structures.

These energies were combined with thermal energy (TE) and entropy (S) estimates from the HF/6-31G** frequency calculations to obtain ΔG values by the following relationship: $\Delta G = \Delta E + \Delta TE - 298(\Delta S)$. Relevant quantities from these calculations are given in Table 7.2. For all protonation states at all computational levels, *trans* species are prediced to be more stable than *cis*, consistent with steric considerations. Little difference is seen between **A** and **B** rotamers of most species. However, the **A/B** difference is larger for the **0** and **++** *trans* stereoisomers. The ΔG values predict a larger energy gap between *cis* and *trans* steroisomers than ΔE values because the *trans* species are more entropically favorable than the more compact and restricted *cis*; this effect is largest for the **+** species.

Table 7.2: Relative gas-phase ΔG values and thermal energy and entropy corrections for all nicotine species considered[a]

Species/ Conformer	HF/6-31G** ΔG	MP2/6-31G** //HF/6-31G** ΔG	B3LYP/6-31G** //HF/6-31G** ΔG	ΔTE + 298x(ΔS) relative to *trans*A
***cis*+ A**	4.32	2.87	4.09	1.19
***cis*+ B**	4.38	2.94	4.15	1.24
***trans*+A**	0.00	0.00	0.06	0.00
***trans*+ B**	0.00	0.01	0.00	-0.03
***cis* A**	5.21	4.30	4.83	0.67
***cis* B**	5.44	4.53	5.08	0.73
***trans* A**	0.00	0.00	0.00	0.00
***trans* B**	0.48	0.52	0.44	-0.04
***cis*++ A**	3.41	2.51	2.69	0.23
***cis*++ B**	3.60	2.75	3.18	0.18
***trans*++ A**	0.00	0.00	0.00	0.00
***trans*++ B**	1.03	1.07	1.03	0.07

[a] All values are given in kcal/mol.

Inclusion of Solvation in Energetic Calculations

Explicit solvation calculations on the **+** conformers were performed using BOSS version 3.8 (Jorgensen, 1997). For these, the optimized HF/6-31G** geometries were used for solute structures. Calculations used an approximately 25 Å cubic cell of 500 TIP4P (Jorgensen et al., 1983) water molecules and the isothermic-isobaric ensemble (NPT) at 25 °C and 1 atm. Standard OPLS all-atom Lennard-Jones parameters (Jorgensen et al., 1996) and CHELPG charges (Breneman and Wiberg, 1990) fit to the HF/6-31G** wavefunction were used for the solutes, as previously recommended (Carlson et al., 1993). Solvent-solvent and solute-solvent interactions were cut off at 12 and 10 Å, respectively, with potential functions quadradically feathered to zero over the final 0.5 Å. Perturbations were performed with ten steps of double-wide sampling to give 20 simulation windows; for each window 2×10^6 and 4×10^6 conformations were sampled for equilibrium and averaging phases, respectively. Volume and solute moves were attempted every 1000 and 50 configurations, respectively, and ranges for moves were set to allow approximately 40% of the moves to be accepted. A thermodynamic cycle of $\Delta\Delta G_{sol}$ values from the perturbations performed are given in Fig. 7.4. These $\Delta\Delta G_{sol}$ values from the SPT/OPLS method can then be combined with the calculated gas-phase values (Table 8.2) to determine relative ΔG values for each of the **+** species in water (Table 8.3).

The HF/6-31G*, HF/cc-pVDZ, and BPW91/6-31G* parameterizations of the SM5.42R method were also used to determine ΔG_{sol} for **+** species. Again, HF/6-31G** structures were used as rigid solutes. The $\Delta\Delta G_{sol}$ values for these calculations are given in Table 7.4; overall relative ΔG values for conformers using these solvation energies

along with TE and S estimates from HF/6-31G** gas-phase frequency calculations are in Table 7.5. As can be seen, SM5.42R $\Delta\Delta G_{sol}$ values are not identical in magnitude to those predicted using the SPT/OPLS method; most striking is the *trans*+**B**/*cis*+**A** difference. Nonetheless, both methods predict the same qualitative order of ΔG_{sol} values for these conformers.

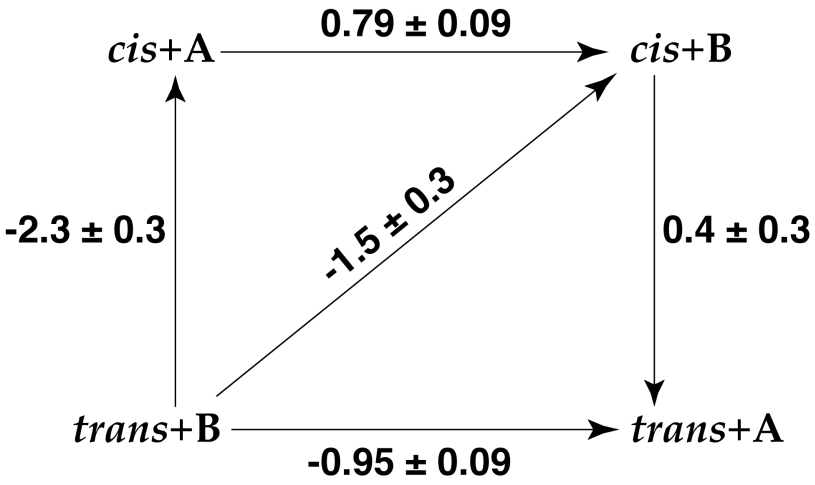

Figure 7.4: Thermodynamic cycle of $\Delta\Delta G_{sol}$ values for singly protonated nicotine species calculated with SPT/OPLS. All values are in kcal/mol.

Table 7.3: Relative ΔG of singly protonated species including computed solvation effects from SPT/OPLS; Predicted relative equilibrium percentages at 25 °C in parentheses[a]

Species/ Conformer	HF/6-31G**	MP2/6-31G**// HF/6-31G**	B3LYP/6-31G**// HF/6-31G**
***cis*+ A**	3.1 ± 0.3 (0.4)	1.6 ± 0.3 (5.3)	2.8 ± 0.3 (0.8)
***cis*+ B**	4.0 ± 0.3 (0.1)	2.5 ± 0.3 (1.1)	3.7 ± 0.3 (0.2)
***trans*+A**	0.0 (82.8)	0.0 (78.1)	0.0 (80.0)
***trans*+ B**	0.95 ± 0.09 (16.7)	0.96 ± 0.09 (15.5)	0.89 ± 0.09 (18.9)

[a] ΔG values are given in kcal/mol.

The overall ΔG values for the species lead directly to predicted equilibrium ratios of each species in solution using a Boltzmann distribution, given for 25 °C in Tables 7.3 and 7.5. Despite quantitative differences, all methods clearly predict that no more than 6% of the species should be in a *cis* conformation, implying the experimental 1:10 *cis*/*trans* ratio may be an upper limit of *cis* present (Whidby and Seeman, 1976). As well, in the receptor binding site, which is not purely aqueous, one would expect the relative proportion of *cis* to be lower than in bulk water since *cis* is stabilized relative to *trans* by aqueous solvation. These percentages do emphasize one difference between the solvation methods, as SPT/OPLS predicts mainly *trans***+A** would be present while SM5.42R predicts that the amounts of *trans***+A** and **B** would be more nearly equal.

Table 7.4: Relative $\Delta\Delta G_{sol}$ values of singly protonated species calculated with SM5.42R at various levels of theory[a]

Species/Conformer	HF/6-31G*// HF/6-31G**	HF/cc-pVDZ// HF/6-31G**	BPW91/6-31G*// HF/6-31G**
***cis*+ A**	0.000	0.000	0.000
***cis*+ B**	0.089	0.640	0.043
***trans*+A**	0.658	1.223	0.632
***trans*+ B**	0.889	1.382	0.817

[a] ΔG values are given in kcal/mol.

Table 7.5: Relative ΔG of singly protonated species including computed solvation effects from SM5.42R; Predicted relative equilibrium percentages at 25 °C in parentheses[a]

Species/Conformer	HF/6-31G*// HF/6-31G**	HF/cc-pVDZ// HF/6-31G**	BPW91/6-31G*// HF/6-31G**
***cis*+ A**	3.68 (0.1)	3.28 (0.2)	3.44 (0.2)
***cis*+ B**	3.81 (0.1)	4.01 (0.1)	3.58 (0.1)
***trans*+A**	0.00 (59.0)	0.00 (58.7)	0.00 (54.6)
***trans*+ B**	0.22 (40.8)	0.21 (41.0)	0.11 (45.1)

[a] ΔG values are given in kcal/mol.

Both solvation methods show two trends in ΔG_{sol} for these species: 1) *cis* species solvate better than *trans* and 2) **A** rotamers solvate better than **B**. The *cis*/*trans* difference can be rationalized by considering solvent accessible surface area (SASA) values calculated by BOSS (Jorgensen, 1997). *Cis* species have lower SASA (381 $Å^2$) than *trans* (398 $Å^2$) and therefore reduce the less favorable interactions that occur at the interface of the hydrophobic portions of the solute and water. Also, *cis* more fully exposes the N^+-H substructure likely to be best solvated. The radial distribution function of water oxygen atoms around the N^+-H proton shows that the first solvation shell has a similar population in *cis* and *trans* species, while a solvation difference arises with a more closely held second shell in *cis*. This difference in second solvation shells could explain why the OPLS/SPT method predicts a larger *cis*/*trans* $\Delta\Delta G_{sol}$ than SM5.42R. **A** rotamers possibly are better solvated than **B** because they have a larger separation between the two oppositely charged regions. Since this change in N-N distance is slightly larger between the *trans*+ than the *cis***+** rotamers, it is reasonable that the relative stabilization of the **A** rotamer is slightly larger in the *trans***+** species for almost all models.

Calculation of ΔG_{sol} of the other nicotine protonation states (**0** and **++**) was performed using the SM5.42R HF/6-31G* parameterized model on HF/6-31G** geometries. This model was applied to these systems in lieu of SPT/OPLS simulations because it produced similar qualitative trends for the singly protonated species at a fraction of the computational expense. The same *cis*/*trans* solvation trend seen for **+** species was seen for other protonation states, and *trans* species are still predicted to be most stable in aqueous solution. But, the **B** rotamers for both **0** and **++** species showed

better solvation than the **A** ones. Thus, in species where the N atoms carry a similar charge, solvation appears to improve with decreased N-N distance.

Relevance to Other Work on Nicotinic Receptors and Agonists

These predictions of nicotine conformation can be considered in light of previous studies estimating the geometrical relationship between "pharmacophore" groups important for nicotine binding, such as optimal N-N distances. Earlier work proposed a N-N distance of 4.8 Å (Sheridan et al., 1986), which is quite close to the calculated *trans***+A** N-N distance (4.655 Å). Later work including the high-affinity nAChR ligand epibatidine proposed a longer optimal N-N distance of 5.5 Å (Glennon et al., 1994). Although this estimate is significantly longer than the *trans***+A** N-N distance, the *trans***+A** conformer does have the maximum N-N distance of the structures considered in this work (Table 7.1), which might provide evidence that it represents the active conformation. Additional research on conformationally restricted nicotine analogs, such as those described in recent reviews, may give increased insight into the physiological difference between the rotamers considered (Glennon and Dukat, 1996; Holladay et al., 1997).

Understanding the conformation of nicotine can also be useful for considering some interesting observations made by Dougherty and co-workers about the activation of nAChR by nicotine. Experimental and computational work reported by Zhong et al. clearly showed that the natural agonist acetylcholine interacts strongly with a trytophan residue at the binding site of the nAChR through a cation-π interaction (Zhong et al., 1998). This assertion has been supported by the crystal structure of the acetylcholine

binding protein with a bound positively charged HEPES molecule (Brejc et al., 2001). However, subsequent work has shown that although nicotine activates the receptor it does *not* appear to interact at the binding site through an analogous cation-π interaction (Beene et al., 2002). The computational predictions about nicotine conformation described in this chapter have helped to provide a starting point for current computational and experimental work performed by Petersson and Cashin attempting to explain these unusual observations about the interactions between nicotine and the nAChR (Cashin, Petersson, et al, unpublished work).

References

Bannon, A. W., M. W. Decker, M. W. Holladay, P. Curzon, D. Donnelly-Roberts, P. S. Puttfarcken, R. S. Bitner, A. Diaz, A. H. Dickenson, R. D. Porsolt, M. Williams, and S. P. Arneric. 1998. Broad-spectrum, non-opioid analgesic activity by selective modulation of neuronal nicotinic acetylcholine receptors. *Science* 279:77-81.

Barlow, R. B., J. A. K. Howard, and O. Johnson. 1986. Structures of nicotine monomethyl iodide and nicotine monohydrogen iodide. *Acta. Cryst.* C42:853-856.

Beene, D. L., G. S. Brandt, W. Zhong, N. M. Zacharias, H. A. Lester, and D. A. Dougherty. 2002. Cation-pi interactions in ligand recognition by serotonergic (5-HT3A) and nicotinic acetylcholine receptors: the anomalous binding properties of nicotine. *Biochemistry* 41:10262-9.

Berthelot, M., M. Decouzon, J.-F. Gal, C. Laurence, J.-Y. Le Questel, P.-C. Maria, and J. Tortajada. 1991. Gas-phase basicity and site of protonation of polyfunctional molecules of biological interest: FT-ICR experiments and AM1 calculations on nicotines, nicotinic acid derivatives, and related compounds. *J. Org. Chem.* 56:4490-4494.

Brejc, K., W. J. van Dijk, R. V. Klaassen, M. Schuurmans, J. van Der Oost, A. B. Smit, and T. K. Sixma. 2001. Crystal structure of an ACh-binding protein reveals the ligand-binding domain of nicotinic receptors. *Nature* 411:269-76.

Breneman, C. M., and K. B. Wiberg. 1990. Determining atom-centered monopoles from molecular electrostatic potentials—the need for high sampling density in formamide conformational-analysis. *J. Comput. Chem.* 11:361-373.

Campillo, N., J. A. Páez, I. Alkorta, and P. Goya. 1998. A theoretical study of epibatidine. *J. Chem. Soc., Perkin Trans.* 2:2665-2669.

Carlson, H. A., T. B. Nguyen, M. Orozco, and W. L. Jorgensen. 1993. Accuracy of free energies of hydration for organic molecules from 6-31G*-derived partial charges. *J. Comp. Chem.* 14:1240-1249.

Chynoweth, K. R., B. Ternai, L. S. Simeral, and G. E. Maciel. 1973. Nuclear magnetic resonance studies of the conformation and electron distributions in nicotine and in acetylcholine. *Mol. Pharm.* 9:144-151.

Colominas, C., F. J. Luque, and M. Orozco. 1999. Dimerization of formamide in gas phase and solution. An ab initio MC-MST study. *J. Phys. Chem. A* 103:6200-6208.

Cox, R. H., J. Kao, H. V. Secor, and J. I. Seeman. 1986. Assessment of isolated electronic effects on conformation. NMR analysis of nicotine and related compounds and ab initio studies of model compounds. *J. Mol. Struct.* 140:93-106.

Edvardsen, Ø., and S. G. Dahl. 1991. Molecular structure and dynamics of acetylcholine. *J. Neural Transm.* 83:157-170.

Eglen, R. M., J. C. Hunter, and A. Dray. 1999. Ions in the fire: Recent ion-channel research and approaches to pain therapy. *Trends Pharm. Sci.* 20:337-342.

Frisch, M. J., G. W. Trucks, H. B. Schlegel, P. M. W. Gill, B. G. Johnson, M. A. Robb, J. R. Cheeseman, T. Keith, G. A. Petersson, J. A. Montgomery, K. Raghavachari, M. A. Al-Laham, V. G. Zakrzewski, J. V. Ortiz, J. B. Foresman, J. Cioslowski, B. B. Stefanov, A. Nanayakkara, M. Challacombe, C. Y. Peng, P. Y. Ayala, W. Chen, W. M. Wong, J. L. Andres, E. S. Replogle, R. Gomperts, R. L. Martin, D. J. Fox, J. S. Binkley, D. J. Defrees, J. Baker, J. P. Stewart, M. Head-Gordon, C. Gonzalez, and J. A. Pople. 1995. Gaussian 94. Version 94, D.3. Pittsburgh, PA: Gaussian, Inc.

Glennon, R. A., and M. Dukat. 1996. Nicotine receptor ligands. *Med. Chem. Res.* 6:465-486.

Glennon, R. A., J. L. Herndon, and M. Dukat. 1994. Epibatidine-aided studies toward definition of a nicotine receptor pharmacophore. *Med. Chem. Res.* 4:461-473.

Hacksell, U., and C. Mellin. 1989. Stereoselectivity of nicotinic receptors. *Prog. Brain Res.* 79:95-100.

Holladay, M. W., M. J. Dart, and J. K. Lynch. 1997. Neuronal nicotinic acetylcholine receptors as targets for drug discovery. *J. Med. Chem.* 40:4169-4194.

Jorgensen, W. L. 1989. Free-energy calculations—a breakthrough for modeling organic-chemistry in solution. *Acc. Chem. Res.* 221:184-189.

Jorgensen, W. L. 1997. BOSS. Version 3.8. New Haven, CN: Dept. of Chem., Yale University.

Jorgensen, W. L., J. Chandrasekhar, J. D. Madura, R. Impey, and M. L. Klein. 1983. Comparison of simple potential functions for simulating liquid water. *J. Chem. Phys.* 79:926-935.

Jorgensen, W. L., D. S. Maxwell, and J. Tirado-Rives. 1996. Development and testing of the OPLS all-atom force field on conformational energetics and properties of organic liquids. *J. Am. Chem. Soc.* 118:11225-11236.

Kier, L. B. 1968. A molecular orbital calculation of the preferred conformation of nicotine. *Mol. Pharm.* 4:70-76.

Koo, C. H., and H. S. Kim. 1965. The crystal structure of nicotine dihydroiodide. *Daehan Hwahak Hwojee* 9:134-141.

Li, J., G. D. Hawkins, C. J. Cramer, and D. G. Truhlar. 1998. Universal reaction field model based on ab initio Hartree-Fock theory. *Chem. Phys. Lett.* 288:293-298.

Margheritis, C., and G. Corongiu. 1988. Acetylcholine in water: Ab-initio potential and Monte Carlo simulation. *J. Comp. Chem.* 9:1-10.

Nagy, P. I., and G. J. Durant. 1996. Monte Carlo simulations of the counter ion effect on the conformational equilibrium of the N, N'-diphenyl-guanidinium ion in aqueous solution. *J. Chem. Phys.* 104:1452-1643.

Nagy, P. I., G. J. Durant, W. P. Hoss, and D. A. Smith. 1994. Theoretical analyses of the tautomeric and conformational equilibria of histamine and (aR,bS)-a,b dimethylhistamine in the gas phase and aqueous solution. *J. Am. Chem. Soc.* 116:4898-4909.

Nagy, P. I., G. J. Durant, and D. A. Smith. 1993. Theoretical studies on hydration of pyrrole, imidazole, and protonated imidazole in the gas phase and aqueous solution. *J. Am. Chem. Soc.* 115:2912-2922.

Nagy, P. I., and K. Takács-Novák. 1997. Theoretical and experimental studies of the zwitterion <--> neutral form equilibrium of ampholytes in pure solvents and mixtures. *J. Am. Chem. Soc.* 119:4999-5006.

Pitner, T. P., W. B. Edwards, III, R. L. Bassfield, and J. F. Whidby. 1978. The solution conformation of nicotine. A ^{1}H and ^{2}H nuclear magnetic resonance investigation. *J. Am. Chem. Soc.* 100:246-251.

Pullman, B., P. Courrière, and J. L. Coubeils. 1971. Quantum mechanical study of the conformational and electronic properties of acetylcholine and its agonists muscarine and nicotine. *Mol. Pharm.* 7:397-405.

Radna, R. J., D. L. Beveridge, and A. L. Bender. 1973. Structural chemistry of cholinergic neural transmission systems. II. A quantum theoretical study of the molecular electronic structure of muscarine, nicotine, acetyl-a-methylcholine, acetyl-b-methylcholine, acetyl-a,b-dimethylcholine, and further studies on acetylcholine. *J. Am. Chem. Soc.* 95:3831-3842.

Seeman, J. I. 1984. Recent studies in nicotine chemistry. Conformational analysis, chemical reactivity studies, and theoretical modeling. *Heterocycles* 22:165-193.

Segall, M. D., M. C. Payne, and R. N. Boyes. 1998. An ab initio study of the conformational energy map of acetylcholine. *Mol. Phys.* 93:365-370.

Sheridan, R. P., R. Nilakantan, J. S. Dixon, and R. Venkataraghavan. 1986. The ensemble approach to distance geometry: Application to the nicotinic pharmacophore. *J. Med. Chem.* 29:899-906.

SPARTAN. Version 5.0. Irvine, CA: Wavefunction, Inc.

Thompson, P. E., D. T. Manallack, F. E. Blaney, and T. Gallagher. 1992. Conformational studies on (+)-anatoxin-a and derivatives. *J. Comp. Aided Mol. Design* 6:287-298.

Whidby, J. F., W. B. Edwards, III, and T. P. Pitner. 1979. Isomeric nicotines. Their solution conformation and proton, deuterium, carbon-13, and nitrogen-15 nuclear magnetic resonance. *J. Org. Chem.* 44:794-798.

Whidby, J. F., and J. I. Seeman. 1976. The configuration of nicotine. A nuclear magnetic resonance study. *J. Org. Chem.* 41:1585-1590.

Zhong, W., J. P. Gallivan, Y. Zhang, L. Li, H. A. Lester, and D. A. Dougherty. 1998. From ab initio quantum mechanics to molecular neurobiology: a cation-pi binding site in the nicotinic receptor. *Proc. Natl. Acad. Sci. USA* 95:12088-93.

Zhu, T., J. B. Li, G. D. Hawkins, C. J. Cramer, and D. G. Truhlar. 1998. *J. Chem. Phys.* 109:9117-9133.